

Seamless integration of the coastal ocean in global marine carbon cycle modeling

M. Mathis¹, K. Logemann¹, J. Maerz², F. Lacroix³, S. Hagemann¹, F. Chugini², L. Ramme^{2,4}, T. Ilyina², P. Korn², and C. Schrum⁵

¹Helmholtz-Zentrum Hereon, Institute of Coastal Systems, Max-Planck-Str. 1, D-21502 Geesthacht

²Max-Planck-Institute for Meteorology, Bundesstr. 53, D-20146 Hamburg

³Max-Planck-Institute for Biogeochemistry, Hans-Knöll-Str. 10, D-07745 Jena

⁴International Max Planck Research School on Earth System Modelling, Hamburg, Germany

⁵University of Hamburg, Institute of Oceanography, Bundesstr. 53, D-20146 Hamburg

Key Points:

- We introduce the first global ocean-biogeochemistry model with a dedicated representation of coastal carbon dynamics.
- We globally apply a grid refinement in the coastal ocean to better resolve regional circulation features, including ocean-shelf exchange.
- We explicitly incorporate key physical and biogeochemical processes controlling coastal carbon dynamics.

Corresponding author: Moritz Mathis, moritz.mathis@hereon.de

Abstract

We present the first global ocean-biogeochemistry model that uses a telescoping high resolution for an improved representation of coastal carbon dynamics: ICON-Coast. Based on the unstructured triangular grid topology of the model, we globally apply a grid refinement in the land-ocean transition zone to better resolve the complex circulation of shallow shelves and marginal seas as well as ocean-shelf exchange. Moreover, we incorporate tidal currents including bottom drag effects, and extend the parameterizations of the model's biogeochemistry component to account explicitly for key shelf-specific carbon transformation processes. These comprise sediment resuspension, temperature-dependent remineralization in the water column and sediment, riverine matter fluxes from land including terrestrial organic carbon, and variable sinking speed of aggregated particulate matter. The combination of regional grid refinement and enhanced process representation enables for the first time a seamless incorporation of the global coastal ocean in model-based Earth system research. In particular, ICON-Coast encompasses all coastal areas around the globe within a single, consistent ocean-biogeochemistry model, thus naturally accounting for two-way coupling of ocean-shelf feedback mechanisms at the global scale. The high quality of the model results as well as the efficiency in computational cost and storage requirements proves this strategy a pioneering approach for global high-resolution modeling. We conclude that ICON-Coast represents a new tool to deepen our mechanistic understanding of the role of the land-ocean transition zone in the global carbon cycle, and to narrow related uncertainties in global future projections.

Plain Language Summary

The coastal ocean is an area hardly taken into account by current climate change assessment activities. Yet, its capacity in carbon dioxide (CO₂) uptake and storage is crucial to be included in a science-based development of sustainable climate change mitigation and adaptation strategies. Earth system models are powerful tools to investigate the marine carbon cycle of the open ocean. The coastal ocean, however, is poorly represented in global models to date, because of missing key processes controlling coastal carbon dynamics and too coarse spatial resolutions to adequately simulate coastal circulation features. Here, we introduce the first global ocean-biogeochemistry model with a dedicated representation of the coastal ocean and associated marine carbon dynamics: ICON-Coast. In this model, we globally apply a higher resolution in the coastal ocean and extend the accounted physical and biogeochemical processes. This approach enables for the first time a consistent, seamless incorporation of the global coastal ocean in model-based Earth system research. In particular, ICON-Coast represents a new tool to deepen our understanding about the role of the land-ocean transition zone in the global climate system, and to narrow related uncertainties in possible and plausible climate futures.

1 Introduction

Our current understanding about the role of the coastal ocean in the marine carbon cycle is limited and fragmentary. Considerable knowledge gaps are related to the interaction between the diverse sources and sinks of carbon in the highly heterogeneous and dynamic land-ocean transition zone and their relation to the biogeochemical processes in the open ocean (Regnier et al., 2013; Ward et al., 2017; G. G. Laruelle et al., 2018). Under present-day climatic conditions, the global coastal ocean has been identified as a net sink for atmospheric CO₂ (G. Laruelle et al., 2014; Gruber, 2015). However, to what extent coastal areas around the globe are taking up or releasing carbon, as well as how much of the carbon exported from the coastal areas enters the deep ocean, remains unclear (Bauer et al., 2013; Roobaert et al., 2019). The coastal ocean, thus, is a largely missing component of current global carbon budgeting (Fennel et al., 2019; Hauck et al., 2020), yet its capacity in carbon storage and transformation is crucial to be included in a science-based development

68 of sustainable mitigation and adaptation strategies to global climate change (Nellemann et
69 al., 2009; Schmidt et al., 2017; Luisetti et al., 2020).

70 The general view is that in coastal areas of middle and high latitudes, net CO₂ draw-
71 down at the sea surface is induced by high biological productivity and an efficient export of
72 sequestered carbon to the adjacent deep open ocean, which outcompetes outgassing in low
73 latitudes driven by temperature effects and substantial terrestrial carbon inputs (Borges &
74 Frankignoulle, 2005; Cai, 2011). However, observation- and model-based estimates of the
75 carbon fluxes across the boundaries of the coastal ocean, determining the overall budget, are
76 poorly constrained. About 2 Gt C yr⁻¹ uncertainty is associated with the amount of carbon
77 deposited in coastal sediments, with estimates ranging from 0.2-2.2 Gt C yr⁻¹ (Krumins et
78 al., 2013). This is about the same amount taken up from the atmosphere by the entire
79 global ocean at present (Park et al., 2010; Landschützer et al., 2016). About 1 Gt C yr⁻¹
80 uncertainty is associated with the coastal CO₂ flux at the air-sea interface, ranging from
81 0.1-1.0 Gt C yr⁻¹ uptake (G. G. Laruelle et al., 2010; Bourgeois et al., 2016), although more
82 recent studies point rather towards the lower end of this spread (Roobaert et al., 2019;
83 Lacroix et al., 2021b). More accurate estimates of coastal carbon fluxes are thus also needed
84 to robustly quantify the anthropogenic perturbation of the global carbon cycle, which is a
85 key diagnostic of the evolution of climate change and the effectiveness of climate policies
86 (Canadell et al., 2010; Friedlingstein et al., 2020).

87 Observations of processes relevant to constrain uncertainties in coastal carbon dynamics
88 are methodologically challenging. Moreover, their spatial and temporal coverage is still
89 scarce and often biased towards certain regions, latitudes and seasons (Painting et al., 2020;
90 Ward et al., 2020). Recent studies applied machine learning algorithms to close data gaps by
91 extrapolating collinearities between target and proxy observables (Lee et al., 2019; Gregor
92 et al., 2019). The results, though, are often sensitive to the choice of the specific approach.

93 Global ocean-biogeochemistry models are powerful tools to gain understanding about
94 the functioning of the marine carbon cycle and to test hypotheses about its response to
95 future scenarios following various socio-economic climate policy directions. To investigate
96 the coastal ocean, however, global ocean-biogeochemistry models are faced with conceptual
97 limitations (Ward et al., 2020). First, global models are not designed to capture the var-
98 ious energetic processes characterizing biogeochemical shelf sea dynamics such as a strong
99 interaction between the water column and the sediment, strong internal mixing, or a strong
100 influence of matter fluxes from land (Fig. 1). Many of these processes are thus typically
101 underrepresented by global biogeochemistry models, if implemented at all (Allen et al.,
102 2010; Hauck et al., 2020). And second, a comparatively high grid resolution is required to
103 adequately resolve shelf-specific processes as well as ocean-shelf exchange. In the shallow
104 coastal ocean, the horizontal grid resolution necessary to resolve the characteristic length
105 scale of the ocean circulation ranges between 1/16° and 1/50° (Hallberg, 2013).

106 Setting up a global model with high grid resolution is not a problem in the first place
107 (e.g. Cheng et al., 2016; Z. Li et al., 2017; Hewitt et al., 2020). The study of global carbon
108 dynamics in the context of contemporary increasing atmospheric pCO₂, however, requires
109 simulation periods of at least multiple decades or even centuries, irrespective of still much
110 longer spinup simulations needed to drive the physical and biogeochemical state of the
111 ocean into equilibrium. Running a conventional global biogeochemistry model at the desired
112 resolutions of 1/16° or higher for several decades, though, is too resource intensive under
113 today's high-performance computing (HPC) capacities, thus excluding this application for
114 practical reasons. Global ocean-biogeochemistry models contributing to the 6th phase of
115 the Coupled Model Intercomparison Project (CMIP6), for example, were run with nominal
116 horizontal resolutions of 1/2° to 1° (Séférian et al., 2020). Model-based investigations of the
117 coastal ocean therefore have mainly pursued the application of regional model systems that
118 enable both, specific process adaptation and finescale grid resolution at lower computational
119 costs. Inconsistencies due to the prescribed forcing at the open lateral boundaries, however,
120 can lead to spurious artefacts influencing the model results in the interior of the regional

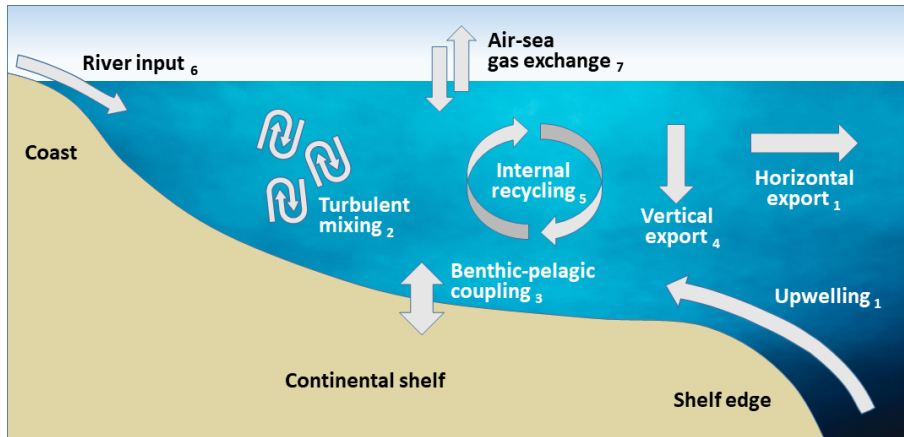


Figure 1: Schematic of key processes controlling coastal carbon dynamics. Attached indices are referred to in the results section 3

121 domain (Marsaleix et al., 2006; Z. Liu & Gan, 2016; Mathis et al., 2018). Moreover, global
 122 budgeting of the coastal ocean requires global coastal coverage, which can hardly be obtained
 123 by regional modeling efforts.

124 In this paper, we present the first global ocean-biogeochemistry model that overcomes
 125 these technical barriers of inadequate grid resolution and process representation in the
 126 coastal ocean. We build our development on the ocean component ICON-O of the new
 127 Earth system model of the Max-Planck-Institute for Meteorology in Hamburg and con-
 128 struct a modified version of this model with a dedicated focus on the land-ocean transition
 129 zone: ICON-Coast. For this task, we take advantage of the triangular grid structure of
 130 ICON-O and globally apply a regional grid refinement in the coastal ocean. Logemann et
 131 al. (2021) have demonstrated a significant improvement of coastal tidal amplitudes simu-
 132 lated with ICON-O when such a regional refinement is used. The advantages of installing
 133 variable-resolution grids in global Earth system models to accommodate complex biogeo-
 134 chemical interactions in the terrestrial-aquatic interface were recently emphasized by Ward
 135 et al. (2020). Besides, the use of unstructured grids was envisaged the most versatile, effi-
 136 cient and elegant way to improve our understanding of the role of shelf seas in global-scale
 137 processes already by Holt et al. (2009). In addition to the regional grid refinement, we
 138 incorporate several modifications and extensions of the standard modules of ICON-O, in
 139 particular for the biogeochemistry component HAMOCC, to improve the representation of
 140 shelf-specific processes related to coastal carbon dynamics (Fig. 1).

141 The aim of this development is to provide a tool for reducing uncertainties in our un-
 142 derstanding of the global carbon cycle and its governing processes via an improved modeling
 143 approach. A seamless connection of the open and coastal ocean merged into a global ocean-
 144 biogeochemistry model enables a consistent two-way coupling of cross-scale physical and
 145 biogeochemical feedback mechanisms in all coastal regions of the world. To lay the grounds
 146 for various scientific applications, we here introduce the general concept of ICON-Coast and
 147 exemplify the skills and potentials of the model by showing results of simulated physical and
 148 biogeochemical key processes related to coastal carbon dynamics.

149 2 Methods

150 2.1 Model description of ICON-O

151 The basis of our development is the global ocean-sea ice-biogeochemistry model ICON-
 152 O (Korn, 2017; Korn & Linardakis, 2018; Logemann et al., 2021). The physical core of

153 the model is based on finite volume numerics. The grid structure discretizes the spherical
 154 surface of the global ocean by triangular cells with a C-type staggering of variables. The
 155 vertical dimension is defined on z coordinates. The primitive equations of fluid motion are
 156 solved with applied hydrostatic and Boussinesq approximations. In the setup presented
 157 here, the vertical turbulent viscosity and diffusivity are parameterized by a TKE mixing
 158 scheme (Gaspar et al., 1990; Gutjahr et al., 2021). Biharmonic operators are used for the
 159 velocity closure. Sea ice advection and thermodynamics are included by a coupling with the
 160 sea ice model FESIM (Danilov et al., 2015).

161 The biogeochemistry component of ICON-O is the Hamburg Ocean Carbon Cycle model
 162 HAMOCC (Maier-Reimer et al., 2005; Ilyina et al., 2013) in its CMIP6 version (Mauritsen et
 163 al., 2019). This version was transferred from the Earth system model MPI-ESM to ICON-O
 164 as the ocean component of the upcoming Earth system model ICON-ESM (Jungclaus et al.,
 165 in prep.). Marine biology dynamics is represented by a NPZD-type approach (Six & Maier-
 166 Reimer, 1996). Sequestration of inorganic carbon and nutrients by phytoplankton growth is
 167 controlled by light availability, water temperature, and co-limitation of the macro nutrients
 168 phosphate and nitrate as well as iron, assuming Redfield stoichiometry (Six & Maier-Reimer,
 169 1996; Kloster et al., 2006). Biogeochemical transformation processes distinguish between
 170 oxic, sub- and anoxic conditions, accounting for bacterial decomposition, denitrification, and
 171 sulfate reduction. The nitrogen cycle includes a prognostic representation of N-fixation at
 172 the sea surface by cyanobacteria (Paulsen et al., 2017). A 3-dimensional sediment module
 173 accounts for deposition and dissolution of particulate matter at the sea floor as well as
 174 benthic-pelagic pore water exchange (Heinze et al., 1999). In the current setup, tracer
 175 advection is calculated by the physical component of the model.

176 2.2 Model extensions for ICON-Coast

177 Starting from the model setup described in the previous section, our improvements re-
 178 garding shelf-specific process representation comprise the incorporation of tidal currents in-
 179 cluding bottom drag effects, and the implementations of sediment resuspension, temperature-
 180 dependent remineralization in the water column and sediment, riverine matter fluxes from
 181 land including terrestrial organic carbon, and variable sinking speed of aggregated partic-
 182 ulate matter. Because of the diversity of these concepts, brief introductions with respect
 183 to their relevance for coastal carbon dynamics are given in the results section 3 to ease the
 184 interpretation of the presented results and the understanding of associated added values.

185 Tidal currents are used as implemented by Logemann et al. (2021). The tide module
 186 accounts for the full luni-solar tidal potential to provide broad frequency tidal dynamics,
 187 including nonlinear interactions between partial tides. Effects of loading and self-attraction
 188 are neglected in this first version of the module.

189 Sediment resuspension is implemented as described in Mathis et al. (2019). Critical bed
 190 shear stresses are calculated from the mean sediment density and grain size at every time step.
 191 The latter are determined by the local sediment composition and the constant density and
 192 grain size assigned to each particle class. The erosion depth is derived from bottom current
 193 velocities inducing overcritical bed shear stress. Here, this has been extended to account
 194 for mixing of eroded pore water with the tracer concentrations in the bottom layer of the
 195 water column, in addition to the erosion and advection of the solid sediment constituents
 196 (detritus, opal, calcium carbonate, and dust).

197 To incorporate a mechanistic representation of the vertical export dynamics of biogeni-
 198 cally bound carbon and nutrients from the euphotic zone to the interior of the ocean, we
 199 adopted a scheme for marine aggregates following Maerz et al. (2020). The formulation
 200 explicitly accounts for the influences of size, microstructure, heterogeneous composition,
 201 density, and porosity of marine aggregates on their settling velocities and exposure to bio-
 202 geochemical transformation processes. Ballasting (biogenic and lithogenic) minerals and

203 particulate organic carbon are tied together, yielding common but variable sinking speeds
 204 for all aggregate components.

205 Water temperature has a non-linear influence on the degradation processes of organic
 206 carbon (Yvon-Durocher et al., 2012; Laufkötter et al., 2017; Lønborg et al., 2018) and diatom
 207 silica frustules (Hurd, 1972; Dixit et al., 2001; van Cappellen et al., 2002). Together with
 208 the explicit representation of marine aggregates, we introduce a consistent temperature
 209 dependence for remineralization and dissolution processes of particulate matter. As the
 210 aggregated particle compounds in the water column sink with a common settling velocity,
 211 they are exposed to a common ambient temperature. Their different degradation length
 212 scales, however, interplay in determining e.g. the ballasting and thus the sinking speed
 213 (Maerz et al., 2020). In the coastal ocean, this intricate connection between POC and
 214 ballasting minerals is particularly relevant where deposited matter may become resuspended
 215 and transported to distant areas and depths. Also here, we follow Maerz et al. (2020) with
 216 a Q10 approach to modify the remineralization rate of detritus and the dissolution rate of
 217 opal, and extend this concept to dissolved organic carbon.

218 Temperature-dependent degradation rates were also reported for the upper sediment,
 219 derived from in-situ measurements, diagenetic modeling, and laboratory incubation exper-
 220 iments (Arndt et al., 2013; Franzo et al., 2019). Consistent with the Q10 approach in the
 221 water column, we extended the temperature-dependence of the degradation of particulate
 222 organic matter and opal to the sediment. Here, we use a Q10 value of 2.3 with a reference
 223 temperature of 10°C for detritus (Provoost et al., 2013) and a Q10 value of 2.3 with reference
 224 temperature of 20°C for opal (Kamatani, 1982; Ridgwell et al., 2002).

225 River mouths are treated as point sources at individual coastal grid cells, incorporating
 226 the work by Lacroix et al. (2020) who investigated the influence of riverine matter fluxes on
 227 the preindustrial oceanic CO₂ outgassing with the global Earth system model MPI-ESM.
 228 Rivers are discharging prescribed fluxes of fresh water, nutrients, organic and inorganic
 229 carbon, and alkalinity. The organic carbon fraction includes terrestrial dissolved organic
 230 matter (tDOM), a biogeochemical tracer usually not considered by global models to date
 231 (Lacroix et al., 2021b). tDOM is more refractory than oceanic organic matter and has a
 232 carbon-to-nutrient ratio that is about 20 times higher (Compton et al., 2000; Aarnos et al.,
 233 2018). The tDOM pool in our model is therefore treated with a C:P mole ratio of 2583:1
 234 (Meybeck, 1982; Compton et al., 2000) and a mineralization rate of 0.003 d⁻¹ (Fichot &
 235 Benner, 2014) at reference temperature of 10°C.

236 All process extensions compared to the standard configuration of HAMOCC (Mauritsen
 237 et al., 2019) were individually evaluated during their original developments for the Earth
 238 system model MPI-ESM and can be found in the primary references given above, including
 239 descriptions of the mathematical formalisms. Our model experiments with ICON-Coast
 240 presented here, thus also represent the first simulations where these processes have been
 241 consistently integrated in a common ocean-biogeochemistry component.

242 **2.3 Regional grid refinement**

243 The other central concept of ICON-Coast, besides the incorporation of shelf-specific
 244 processes, is the application of a regionally refined numerical grid. This is done to resolve
 245 shelf sea dynamics more properly, while reducing resource demands compared to simulations
 246 with a globally uniform high resolution.

247 Increasing horizontal resolution is assigned locally according to three geometric criteria
 248 (Logemann et al., 2021): decreasing distance to the coast, decreasing water depth, and
 249 increasing slope of the bottom topography. By combining these criteria we obtain higher
 250 resolution in the near-coastal zones as well as the shallow shelves, broadly including the shelf
 251 breaks as the transition to the open ocean. Areas of different resolutions are connected by
 252 cell bisection and subsequent local spring optimization to assure smooth grid spacing and

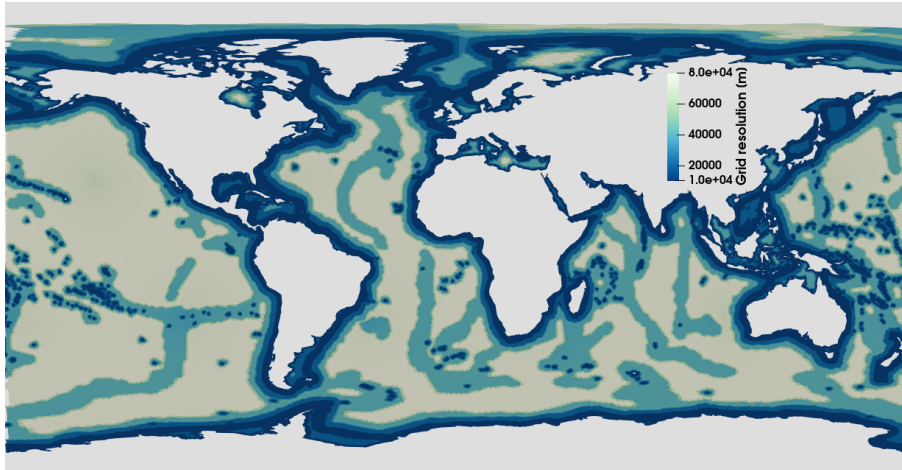


Figure 2: Grid configuration used for the high-res simulations with a horizontal resolution ranging from 80 km in the open ocean to 10 km at the coast lines and continental margins. For the low-res simulations, a qualitatively similar configuration has been used with a horizontal resolution that is coarser by a factor of 2, ranging from 160-20 km

253 avoid critically distorted cell geometries. An example of a grid configuration used in this
 254 study is shown in Fig. 2.

255 The grid refinement accounts for a more detailed discretization of topographic features
 256 in the coastal ocean, enabling a better representation of the general circulation in shelf and
 257 marginal seas. In particular, many ocean-shelf exchange mechanisms such as cross-slope
 258 bottom transport, instabilities of frontal boundary currents, or eddy-shelf interaction are
 259 strongly influenced by ageostrophic processes which can be significantly better resolved by
 260 mesoscale grid resolutions (Karakas et al., 2006; Oguz et al., 2015; Brink, 2016; Graham
 261 et al., 2018b; Thévenin et al., 2019; Combes et al., 2021; Kämpf, 2021). Moreover, an
 262 increased grid resolution permits the local development of high horizontal temperature and
 263 salinity gradients which enhances the baroclinic components of the general circulation. As
 264 all biogeochemical tracers in the model are subject to advection, the better representation
 265 of the circulation is vital for improving the simulated biogeochemical state of the coastal
 266 ocean.

267 Due to the applied slope criterion, a moderate refinement is also assigned to mid-ocean
 268 ridges, seamounts, and submarine banks (Fig. 2). This accounts for a better representation
 269 of the abyssal circulation in the open ocean, associated with tidal mixing (Simmons et al.,
 270 2004; Dale & Inall, 2015) as well as transport of heat and biogeochemical tracers parallel to
 271 the ridge's flanks (Lavelle et al., 2012). Moreover, the capture of bathymetric gaps, such as
 272 fracture zones, determines how much deep water can pass between ocean basins and where
 273 this exchange occurs (Gille et al., 2004).

274 The spatial positioning of variables within the numerical grid follows an Arakawa C-grid
 275 staggering, with scalar variables at the cell centre and normal components of the velocity
 276 vector at cell boundaries. This staggering type is numerically advantageous. For triangular
 277 cells, however, it is associated with spurious discontinuities in the divergence field of the
 278 horizontal flow (Stuhne & Peltier, 2009; Danilov, 2010). To overcome this problem, the dis-
 279 cretization of the primitiv equations of fluid motion is based on a novel technique developed
 280 by Korn (2017), which provides an efficient way to control divergence noise without violating
 281 conservation conditions. The numerical stability of strongly irregular grids as used in our
 282 simulations was demonstrated by Logemann et al. (2021), who conducted comprehensive
 283 test simualtions with the core model ICON-O.

284

2.4 Experiment design

285

286

287

288

289

290

291

292

293

294

295

296

297

298

299

300

301

302

303

In this paper, we show results from two ICON-Coast simulations with different horizontal grid configurations. The first one spans a resolution of 160-20 km (low-res) and has been run in coupled physics-biogeochemistry mode. The resolution of the second configuration is higher by a factor of 2, spanning 80-10 km (high-res; Fig. 2), and has been run in physics-only mode to assure reasonable simulation progress and computational cost. The advantage of including the high-res simulation, albeit in a light version, is that we can better demonstrate the benefit of a regional grid refinement for the representation of relevant hydrodynamic features in the coastal ocean that provide the background conditions for the biogeochemical processes. In particular at the upper end of the resolution range (10 km), we reach or come close to the first baroclinic radius of deformation in many shelf seas and ocean-shelf transition zones, thus incorporating mesoscale activity more extensively than in the low-res simulation (Hallberg, 2013; Hewitt et al., 2017). Representing the mesoscale explicitly was shown to tangibly improve the simulated mean ocean state as well as the temporal variability (Hewitt et al., 2020). For both grid configurations, the vertical dimension is resolved by 40 layers with a surface layer thickness of 16 m, a layer thickness of 10 m in the remaining upper 100 m of the water column, and increasing thicknesses below. The high surface layer thickness is necessary in this model setup to allow for critical tidal amplitudes and sea ice formation, as a wetting-drying algorithm is not yet included. Internal model time steps are 400 s for the low-res and 100 s for the high-res setups.

304

305

306

307

308

309

310

311

312

313

314

315

316

317

The simulations were driven with ERA-Interim reanalysis data (Dee et al., 2011) of 6-hourly atmospheric forcing fields for the period 1990-2010. River runoff data are taken from a hindcast reconstruction by the global hydrological discharge model HD (Hagemann & Dümenil-Gates, 2001) for the period 1979-2009 and applied as monthly climatological means. The hindcast was generated by applying the HD model (vs. 1.10) to a simulation of the land surface scheme JSBACH (Ekici et al., 2014) forced by bias corrected ERA-Interim data (Hagemann et al., 2020). Lateral discharge fluxes were calculated globally at 0.5° resolution and comprise about 2000 catchments areas. Riverine inputs of DIP, DIN, DSi, DFe, DIC, Alk, tDOM (terrestrial dissolved organic matter) and POM are derived from Lacroix et al. (2020, 2021b) for about 850 rivers under 1980-2010 conditions (Table 1). In these studies, historical river loads for the period 1905-2010 were reconstructed based on a hierarchy of weathering and terrestrial organic matter export models as well as the global data set NEWS2 (Seitzinger et al., 2010). Non-weathering sources of nutrients, C and Alk from fertilizer, sewage, and allochthonous inputs were also considered.

318

319

320

321

322

323

324

325

326

327

328

329

330

331

332

333

334

Both simulations, low-res and high-res, were initialized by temperature and salinity fields taken from the 0.25° resolution World Ocean Atlas 2013 data set (Locarnini et al., 2013; Zweng et al., 2013) and an ocean at rest. Because of high computational resource demands, we so far have only performed comparatively short simulations of maximum 20 consecutive years. The biogeochemical initial state of the low-res run was therefore taken from previous test and calibration runs in order to reduce effects of long-term drift as much as possible. As the process extensions for HAMOCC were done consecutively, we originally started from the biogeochemical state of the year 1979, simulated by the CMIP6 version of MPI-ESM-LR (Mauritsen et al., 2019), and continued until the year 2010 with several repetitions of intermittent periods to adjust new biogeochemical parameters. To apply this strategy, we could not yet account for contemporary increasing atmospheric pCO₂ but used a constant preindustrial level of 278 ppm. The simulated CO₂ fluxes at the sea surface are thus expected to be biased towards weaker uptake and stronger outgassing compared to observational products of the recent past. The results shown here finally stem from a repetition of the period 2000-2010, where no model parameters have been adjusted further. While being aware of associated limitations, with this approach we aim for a first-order understanding of the added value of the global coastal setup and resulting dynamics therein.

Table 1: River inputs for the period 1981-2010 used in the presented ICON-Coast simulations as derived by Lacroix et al. (2020, 2021b), and contemporary observation- and model-based estimates from literature.

Compounds	ICON-Coast	Contemporary estimates	References
DIP [Tg P yr ⁻¹]	1.2	0.8-1.4	Meybeck (1982); Compton et al. (2000); Seitzinger et al. (2010)
DIN [Tg N yr ⁻¹]	17.6	12-19	Meybeck (1982); Seitzinger et al. (2010)
DSi [Tg Si yr ⁻¹]	328	170-490	Beusen et al. (2009); Dürr et al. (2011); Tréguer & De La Rocha (2013); Tréguer et al. (2021)
DIC/Alk [Tg C of HCO ₃ ⁻ yr ⁻¹]	370	260-550	Berner et al. (1983); Amiotte Suchet & Probst (1995); Hartmann et al. (2009); M. Li et al. (2017)
DOM [Tg C yr ⁻¹]	216	130-240	Meybeck & Vörösmarty (1999); Seitzinger et al. (2010); M. Li et al. (2019)
POM [Tg C yr ⁻¹]	115	100-230	Meybeck & Vörösmarty (1999); Seitzinger et al. (2010); Galy et al. (2015)

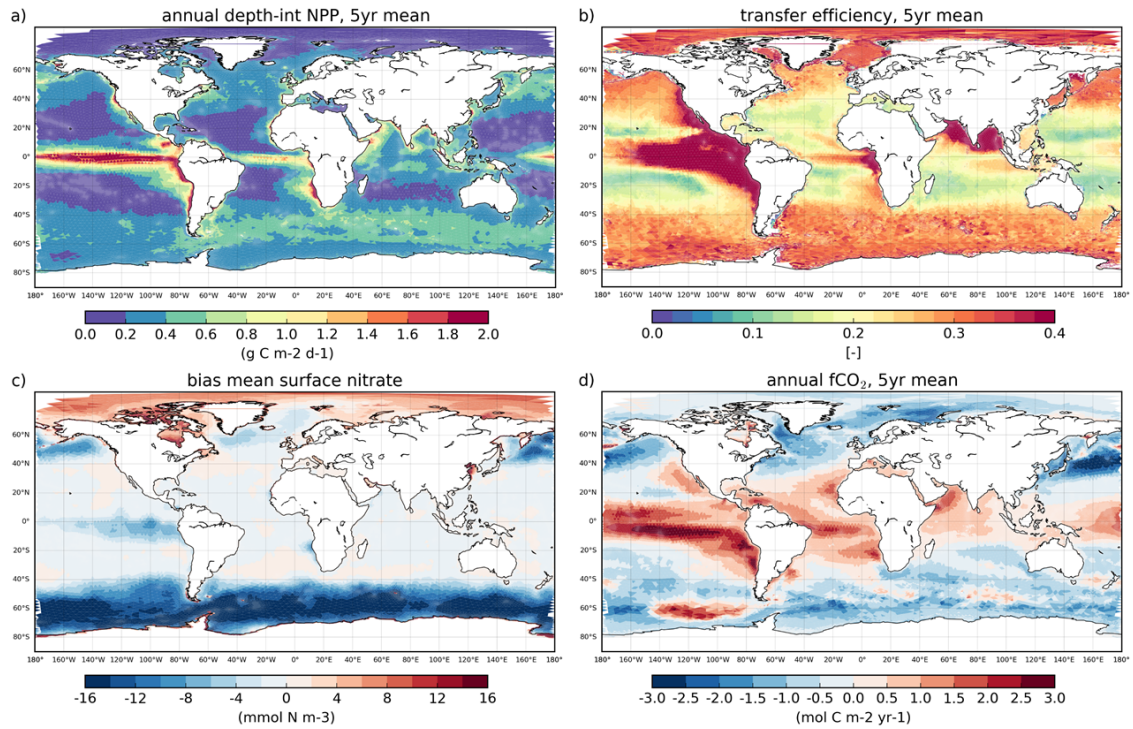


Figure 3: Global distributions of annual depth-integrated net primary production (a), transfer efficiency of organic carbon to the deep ocean (1000 m, b), bias in surface nitrate concentration (c), and ocean-atmosphere CO_2 flux (d), simulated with low-res configuration. Positive values in (d) refer to oceanic outgassing.

3 Results

3.1 Global biogeochemical patterns

Simulated global patterns of net primary production, transfer efficiency, nutrient concentrations (biases), and ocean-atmosphere CO_2 flux are shown in Fig. 3. The general distributions reflect the persistent large-scale features and global patterns known from observational products and global ocean-biogeochemistry models.

High biological productivity in the open ocean is linked to favorable light conditions and continuous or seasonal nutrient supply to the euphotic zone via upwelling or deep mixing. Thus, enhanced primary production is found in the equatorial Pacific, the eastern upwelling areas, and the subpolar gyres, whereas the oligotrophic subtropical gyres are substantially less productive throughout the year (Fig. 3a; Boyd et al., 2014; Kulk et al., 2020). In the Arctic Ocean, phytoplankton growth is weak due to the sea ice cover and limited light availability. In the greater Arctic (north of the polar circle), ICON-Coast simulates a mean productivity of $32 \text{ g C m}^{-2} \text{ yr}^{-1}$, which is underestimated compared to $36\text{--}39 \text{ g C m}^{-2} \text{ yr}^{-1}$ estimated from model experiments and remote sensing products by Terhaar et al. (2021) and K. R. Arrigo & van Dijken (2015), respectively. The lower productivity can be attributed to terrestrial nutrient supply from coastal erosion, which sustains around 20% of Arctic net primary production (Terhaar et al., 2021), but is not yet taken into account in the simulations presented here. The simulated global net primary production amounts to $49\text{--}52 \text{ Gt C yr}^{-1}$ (min-max during the simulation period) with a positive drift of about $0.09 \text{ Gt C yr}^{-1}$ (derived from linear regression). Contemporary observation-based estimates range between $39\text{--}58 \text{ Gt C yr}^{-1}$ (Buitenhuis et al., 2013; Richardson & Bendtsen, 2019; Kulk et al., 2020) and model results show a wide spread of $20\text{--}80 \text{ Gt C yr}^{-1}$ (Laufkötter et al., 2015; Séférian et al., 2020).

359 The simulated global export of organic matter out of the euphotic zone is 8.0 Gt C yr^{-1}
360 and is comparable to the particle flux of 9.1 Gt C yr^{-1} derived from data assimilation by
361 DeVries & Weber (2017). The amount of carbon reaching the deep ocean is influenced
362 by the variable sinking speed of aggregated organic and mineral particles. Another criti-
363 cal parameter is the temperature dependence of the compound's degradation rates, as it
364 determines the sensitivity of aggregates to extensive biogeochemical transformation. The
365 strong temperature gradients in the upper ocean across latitudes and seasons thus promote
366 spatially and temporally heterogeneous recycling rates and export fluxes, with maximum
367 ranges being observed in the shallow coastal areas (Guidi et al., 2015; Xie et al., 2019). The
368 combination of the aggregate sinking scheme and temperature-dependent degradation pro-
369 cesses applied in ICON-Coast has been shown to induce a global shift in the vertical carbon
370 transfer to the deep ocean towards the poles (Maerz et al., 2020), which is also simulated by
371 ICON-Coast (Fig. 3b). In particular the temperature influence promotes shallower reminer-
372 alization at low latitudes and deeper remineralization at high latitudes (Laufkötter et al.,
373 2017), enabling the reproduction of latitudinal characteristics of the POC transfer efficiency
374 investigated by Weber et al. (2016) and DeVries & Weber (2017). In addition, the transfer
375 efficiency is regionally modulated by low oxygen concentrations, leading in our model to
376 maximum values exceeding 50% in the oxygen minimum zone of the Equatorial Tropical
377 Pacific. The simulated values, however, are generally overestimated, with a minimum of
378 about 10% transfer efficiency in the subtropical gyres and about 30% in high latitudes,
379 compared to 5% and 25% estimated from inverse modeling of phosphate fluxes by Weber et
380 al. (2016), respectively.

381 Surface nutrient concentrations show low biases in most ocean basins compared to World
382 Ocean Atlas 2018 Boyer et al. (2018). A mismatch, though, can be seen in the Southern
383 Ocean with deviations of about $-14 \text{ mmol N m}^{-3}$, $-0.8 \text{ mmol P m}^{-3}$, and $+20 \text{ mmol Si m}^{-3}$
384 in annual mean nitrate, phosphate and silicate concentrations, respectively (Fig. 3c and
385 Fig. A1). Besides, nitrate concentrations are slightly too high in the Arctic. Both the pat-
386 terns and magnitudes of these biases are also prominent features of the previous HAMOCC
387 implementation in MPI-ESM and have been linked to coarse grid resolution, overestimated
388 vertical velocities, and too low iron limitation (Ilyina et al., 2013).

389 Regarding surface CO_2 fluxes, low latitudes are dominated by strong outgassing in
390 particular in upwelling areas, with maximum net fluxes in the equatorial Pacific (Park et
391 al., 2010; Landschützer et al., 2016). Middle and high latitudes, by contrast, function as
392 net sinks for atmospheric CO_2 , governed by surface cooling and high seasonal biological
393 export production. The spatial distribution and zonal averages of simulated $f\text{CO}_2$ (Fig. 3d
394 and Fig. 4) qualitatively capture these latitudinal characteristics, e.g. as derived from field
395 measurements of the recent past (Takahashi et al., 2009; Landschützer et al., 2016; Bushinsky
396 et al., 2019). Deviations lie well within the model spreads of CMIP5/6 (Séférian et al.,
397 2020) and the Global Carbon Project (Hauck et al., 2020), with our model showing biases
398 of overestimated outgassing in low latitudes and underestimated outgassing in the Southern
399 Ocean. The global integral amounts to $0.1\text{-}0.2 \text{ Gt C yr}^{-1}$ outgassing with a negative drift of
400 about $-0.03 \text{ Gt C yr}^{-2}$. Note that the observed contemporary global uptake in the order of
401 2 Gt C yr^{-1} is not met because we have run ICON-Coast with constant preindustrial $p\text{CO}_2$
402 in the atmosphere (section 2.4), thus approaching equilibrium conditions with net surface
403 CO_2 fluxes driven by river inputs.

404 In general, the main biogeochemical features of the global open ocean are reasonably
405 well represented, in particular compared to earlier model studies. It is thus worth turning
406 the emphasis to the core of ICON-Coast, the coastal and shelf sea regions, to assess the
407 added value of the presented approach.

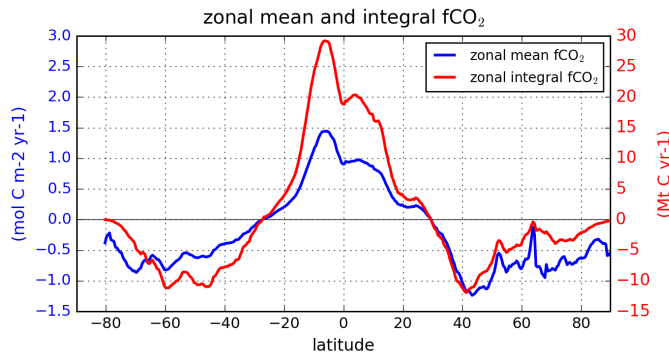


Figure 4: Zonally averaged (blue) and integrated (red) ocean-atmosphere CO_2 flux, simulated with low-res configuration. Positive values refer to oceanic outgassing.

3.2 Shelf sea dynamics

The primary motivation behind the development of ICON-Coast is to improve the traditional global modeling approach by enabling a better representation of coastal and shelf sea carbon dynamics (Fig. 1). The added value of ICON-Coast, thus, has to be assessed mainly by comparison to conventional ocean-biogeochemical models in capturing the general ranges and orders of magnitude of key biogeochemical parameters in the coastal ocean. We therefore directly compare our results to the global Earth system model MPI-ESM, which used the standard version of HAMOCC (Mauritsen et al., 2019), and verify remaining biases against available observations and regional modeling studies. In particular, we focus on three temperate coastal regions that share the large influence of tidal currents but differ through their embedding in the large-scale ocean circulation (Fig. 5): the Northwest European Shelf (NWES), the Patagonian Shelf (PS), and the East China Shelf (ECS). The NWES is connected to the eastern boundary current system of the North Atlantic subpolar gyre (SPG). The physical and biogeochemical characteristics of water masses flushing the shelf are strongly influenced by the strength of the SPG and the wintertime mixed layer depth in the Northeast Atlantic (Hátún et al., 2017; Koul et al., 2019). The PS is connected to the Antarctic Circumpolar Circulation (ACC) passing through the Drake Passage, and the northward flowing Malvinas Current (MC) branching off the ACC. Shelf water mass characteristics are modulated by the inflow of Subantarctic water and shelf break upwelling induced by the variability of the MC (Combes & Matano, 2018). The ECS is connected to the western boundary current of the North Pacific subtropical gyre. The water masses of this shelf sea mainly originate from the Kuroshio Current and are strongly influenced by the strength of the Yellow Sea Warm Current branching from the Kuroshio Current during boreal winter (Yuan et al., 2008; Lie & Cho, 2016). All three shelf regions are known to be net sinks for atmospheric CO_2 under present-day climatic and environmental conditions, driven by high biological carbon sequestration and an efficient export of respiratory CO_2 to the adjacent deep ocean (e.g. Becker et al., 2021; Kahl et al., 2017; Jiao et al., 2018). Moreover, they are subject to a strong seasonality of both the atmospheric forcing and the response of the physical and biogeochemical conditions in the ocean, and were extensively investigated by observational and regional modeling studies. These shelf areas thus serve as pivotal regions to test and evaluate our new model implementations.

In general, we show results of biogeochemical parameters from the low-res simulation but physical parameters from the high-res simulation (see section 2.4). This is done to best emphasize the potentials of ICON-Coast in regional high-resolution modeling at the global scale, as well as to demonstrate the ability of the model to simulate key processes of marine coastal carbon dynamics. Differences between high-res and low-res physics are discussed in section 4. The following examples given for the three focus regions are monthly, seasonal,

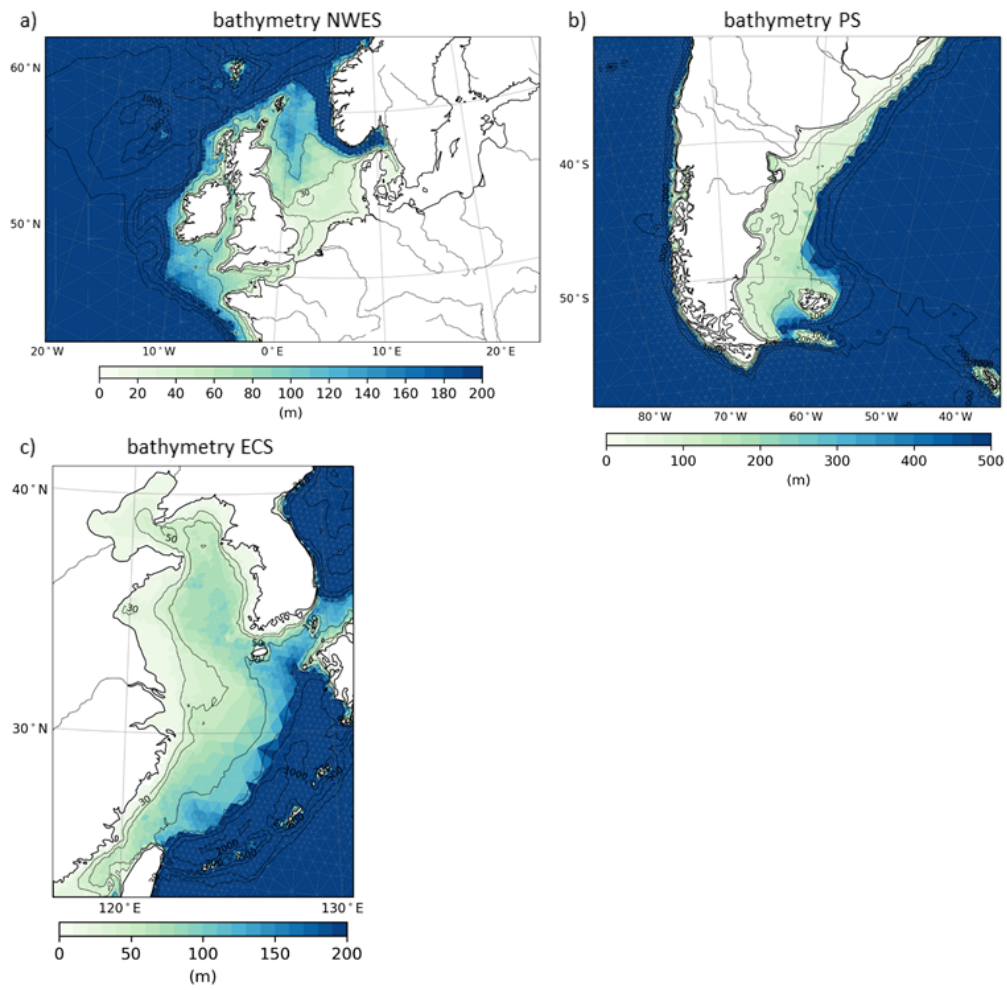


Figure 5: Model bathymetry of the Northwest European Shelf (a), Patagonian Shelf (b) and East China Shelf (c). Isobaths correspond to water depths of 30, 50, 100, 200, 500, 1000, 2000, and 3000 m.

Table 2: Volume transports ($10^6 \text{ m}^3 \text{ s}^{-1}$) through selected transects in the North Sea simulated by ICON-Coast (high-res configuration) as well as estimates from observational products and regional model systems for the period 1998-2009 presented in Pättsch et al. (2017). Identifiers in brackets refer to the section names and descriptions given in that study.

North Sea section	ICON-Coast	Observations	Model spread
Fair-Isle inflow (S1)	0.3	0.3	0.4-0.6
Inflow at 59°N (S2)	0.7	0.6	0.2-1.1
Outflow at 59°N (S3)	1.2	0.9	0.4-1.3
Skagerrak recirculation (S10)	0.8	1.0 ± 0.5	0.4-1.7
Jutland Current (S8)	0.20	-	0.19-0.33
English Channel (S6)	0.18	0.13 ± 0.04	0.01-0.15

445 or annual means over the last 5 years of our simulations, that is 2006-2010. These results
 446 are opposed to the ensemble mean over 10 realizations of the same period simulated by the
 447 Earth system model MPI-ESM (Mauritsen et al., 2019) in low-resolution version (LR) as it
 448 contributed to CMIP6.

449 3.2.1 General circulation

450 The general circulation of shelf seas governs the advective export of sequestered carbon
 451 from the coastal to the open ocean as well as the import of nutrient-rich water masses from
 452 deeper levels via shelf break upwelling and vertical mixing (Fig. 1 index 1; Painter et al.,
 453 2016; Legge et al., 2020; Luisetti et al., 2020). The circulation in the proximal coastal zone
 454 determines the distribution of river discharge and nutrient loadings in the inner shelf areas,
 455 as the position of river plumes is typically more sensitive to the wind direction than to the
 456 river outflow variability (Pimenta et al., 2005; Kastner et al., 2018; Kerimoglu et al., 2020).
 457 The strength and structure of the general circulation therefore sensitively influences the
 458 residence times of imported water masses on the shelves, and hence the local physical and
 459 biogeochemical water mass characteristics (Pättsch et al., 2017; X. Liu et al., 2019; Lacroix
 460 et al., 2021a). A proper representation of the general circulation is thus key for investigating
 461 coastal carbon dynamics and constraining budget uncertainties.

462 On the NWES, the simulated mean circulation shows all characteristic features of the
 463 well-studied North Sea circulation (Fig. 6a). The pathways of the Fair-Isle Current, East-
 464 Shetland Flow, the inflow along the western side of the Norwegian Trench which recirculates
 465 in the Skagerrak and leaves the North Sea via the Norwegian Coastal Current, the Dooley
 466 Current, and the weak cyclonic circulation in the southern North Sea (Holt & Proctor,
 467 2008; Sündermann & Pohlmann, 2011) can be well identified. Transport rates of prominent
 468 sections are evaluated in Table 2. The irregularities in the south-western area are probably
 469 related to influences of interannual variability on the shown 5-yr mean. The net transport
 470 through the North Sea simulated by ICON-Coast varies between 1.6-1.8Sv and lies within
 471 the range of 0.9-2.3Sv found in the literature (Mathis et al., 2013; Quante et al., 2016;
 472 Pättsch et al., 2017).

473 The circulation on the PS is more homogeneous than on the NWES (Fig. 6b). Part
 474 of the Cape Horn Current turns onto the shelf between the South American mainland and
 475 the Falkland Islands and generally flows northward to meet the La Plata river plume and
 476 the Brazil Malvinas Confluence (Combes & Matano, 2018). The inflow of the Cape Horn

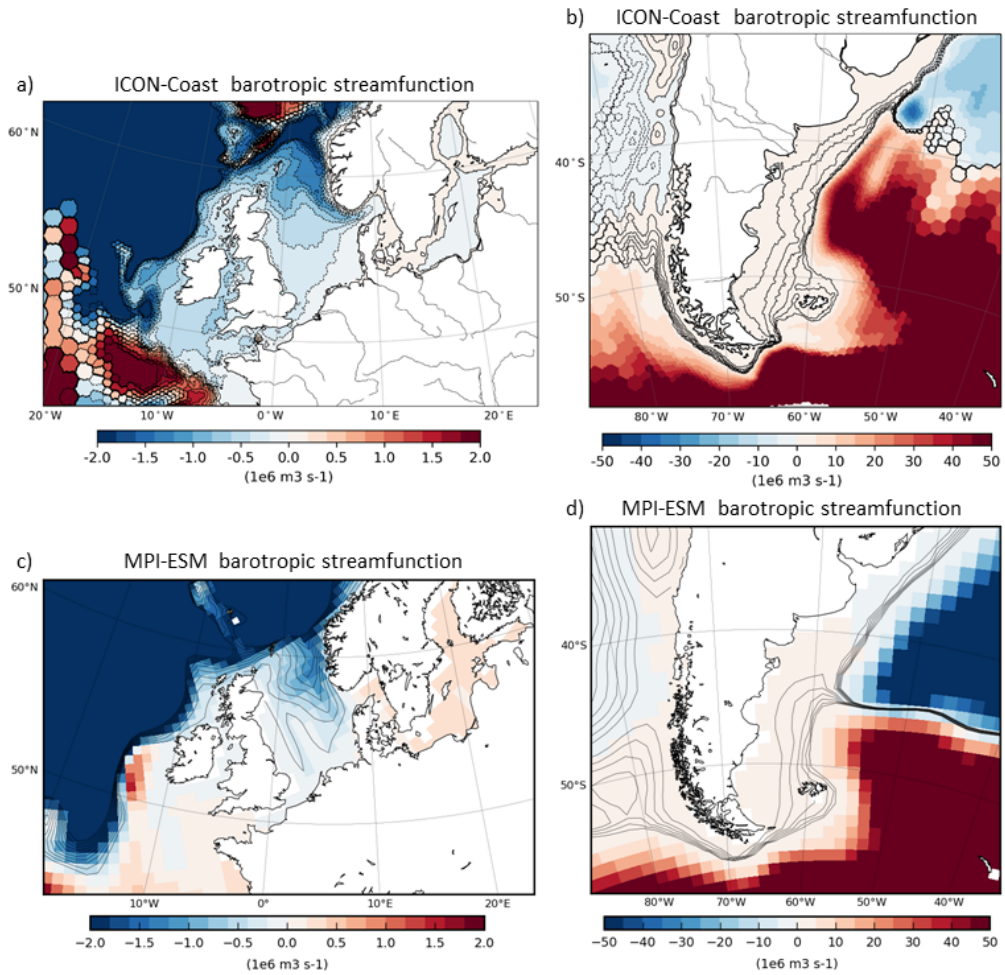


Figure 6: Annual mean barotropic streamfunction on the Northwest European Shelf (a,c) and Patagonian Shelf (b,d), simulated with ICON-Coast high-res configuration (a,b) and MPI-ESM (c,d). Increments of shown streamlines are 0.2 Sv for (a,c) and 0.5 Sv for (b,d). Hexagonal structures in (a,b) emerge from the calculation and mapping of net volume fluxes through the triangular grid cells.

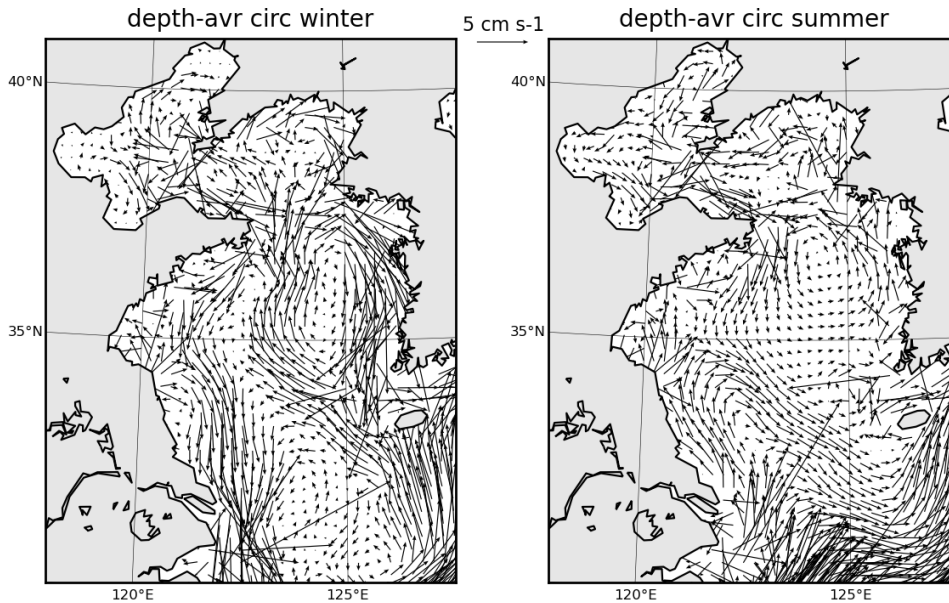


Figure 7: Depth-averaged current velocities on the East China Shelf for winter (left) and summer (right), simulated with high-res configuration.

477 Current to the shelf is about 2.5 Sv simulated by ICON-Coast and has been quantified by
 478 a high-resolution regional model study to about 1.7 Sv (Guihou et al., 2020). This is a
 479 reasonable agreement, assuming similar variability and uncertainty ranges as for the well-
 480 studied NWES.

481 On the ECS, distinct seasonal circulation patterns are driven by the characteristic
 482 monsoon wind regimes. In winter, the Yellow Sea Warm Current branches from the Kuroshio
 483 Current and flows northward into the Bohai Sea (R. Wu et al., 2016). This ECS inflow is
 484 balanced by the southward flowing Korean and Chinese coastal currents. In summer, the
 485 whole pattern changes into a cyclonic recirculation through the entire Yellow Sea and Bohai
 486 Sea (Zhu et al., 2015). ICON-Coast is able to capture the main features of this marked
 487 seasonality with great detail (Fig. 7). We can even identify the anticyclonic circulation in
 488 the northern part of the Bohai Sea in winter and its cyclonic turn in summer (Yang et al.,
 489 2019). The throughflow of the Taiwan and Tsushima Straits act as the origination and
 490 destination of the mean ECS circulation, respectively (Z. Liu, Gan, et al., 2021). The mean
 491 transport rate in the Taiwan Strait is simulated 1.3 Sv, with observations ranging between
 492 1.3-2.0 Sv and a regional modeling spread of 0.4-2.3 Sv (J. Hu et al., 2010; H. W. Chen et
 493 al., 2016; Z. Liu, Gan, et al., 2021). The main outflow through the Tsushima Strait into the
 494 Sea of Japan seems underestimated, with a simulated tranport of 1.8 Sv and observations of
 495 about 2.6 Sv (Z. Liu, Gan, et al., 2021). The region of coastal water diluted by the Yangtze
 496 river (salinity less than 28 psu) mainly spreads eastward and northward into the East China
 497 and Yellow Seas with a maxium extension to about 123°E and 35°N in summer, in good
 498 agreement with 124°E and 35°N during Jul/Aug 1998-2010 derived from remote sensing by
 499 Bai et al. (2014).

500 In MPI-ESM, by contrast, the coarser grid resolution leads to a systematic underestima-
 501 tion of shelf sea circulations (Fig. 6c, d). While the general flow pattern is partly captured in
 502 outer shelf areas, the structure and strength of individual currents, in particular in the inner
 503 areas, is not adequately represented. Moreover, in the south-western Atlantic, the position
 504 of the Brazil Malvinas Confluence is simulated too far to the south by about 10°(Fig. 6d),

505 disturbing water mass properties in the northern part of the PS with biases of up to +5°C
 506 and +0.7 psu in surface temperature and salinity (+1°C and +0.4 psu in ICON-Coast). We
 507 abstain from a correlate of Fig. 7, as in MPI-ESM the entire region would be covered by
 508 only a dozen velocity vectors (see e.g. Fig. 9).

509 **3.2.2 Tidal waves**

510 The most energetic flows in the coastal ocean are generated by tidal waves, with max-
 511 imum current speeds exceeding 60 cm/s twice a day (Poulain & Centurioni, 2015). The
 512 interaction with the topography in shallow areas induces energy dissipation via bottom fric-
 513 tion and leads to high bed shear stresses and turbulent mixing in the water column (Fig. 1
 514 index 2; Wilson & Heath, 2019). These effects are known to play an important role in the
 515 coastal nutrient and carbon dynamics (Cadier et al., 2017; Zhao et al., 2019).

516 In our model, tidal waves are calculated from the full luni-solar tidal potential. As
 517 shown by Logemann et al. (2021), who have run variable-resolution grids with ICON-O,
 518 the simulated amphidromic patterns as well as tidal amplitudes for both the open ocean
 519 and coastal areas generally agree with tidal charts derived from gauge measurements and
 520 satellite altimetry data (e.g. Egbert & Erofeeva, 2002). Here, we exemplify simulated M2
 521 amplitudes for the three shelf seas under consideration (Fig. 8) and elaborate more on the
 522 effects of tide-induced currents related to carbon dynamics in the following sections. A
 523 comparison with MPI-ESM cannot be provided here as this model was not run with tides.

524 ICON-Coast is able to reproduce complex tidal systems in the coastal ocean, as those of
 525 the NWES and ECS (Fig. 8). The positions of the amphidromic points of the M2 constituent
 526 are well captured. On the NWES, tidal amplitudes reach around 1.5 m in the German Bight
 527 area, between 1.5-2 m along the British North Sea coast and maximum heights exceeding
 528 3 m in the English Channel and Celtic Sea (e.g. Reynaud & Dalrymple, 2012). On the ECS,
 529 pronounced sea surface elevations of up to 2 m in the Taiwan Strait and along the Korean
 530 coast are realistically simulated (e.g. H. Wu et al., 2018), as well as the low amplitudes in the
 531 Bohai Sea which do not exceed 0.5 m. The amphidromic pattern of the PS is well captured
 532 likewise. Amplitudes, however, are simulated too high by a factor of about 1.5 compared to
 533 satellite altimetry data (Birol et al., 2017) and regional tidal modeling (Ke & Yankovsky,
 534 2010; Carless et al., 2016), with simulated maximum values of 6 m in the southern PS.

535 **3.2.3 Seasonal stratification**

536 On temperate shelves, tidal mixing is able to break the summer stratification and
 537 in many shallow areas the water column stays vertically mixed throughout the year (van
 538 Leeuwen et al., 2015). In deeper areas, the characteristic seasonal stratification prevents
 539 respiratory CO₂ below the pycnocline to exchange with the atmosphere (Thomas et al.,
 540 2004; Bianchi et al., 2005; Rippeth et al., 2014). Sharp changes in ocean-atmosphere $\Delta p\text{CO}_2$
 541 of up to 150 ppm across tidal fronts are often observed (Bianchi et al., 2005). The strength of
 542 the stratification as well as its spatial extension and timing in the year thus are key elements
 543 of the shelf carbon pump, promoting net horizontal carbon export to the deep open ocean.

544 Conventional global ocean models are typically run without tides (Taylor et al., 2012;
 545 Eyring et al., 2016). Tidal waves mainly transport energy but very little mass (Toffoli &
 546 Bitner-Gregersen, 2017), and in the open ocean the local net effects of tides are negligibly
 547 small for most applications. Hence, tides are usually omitted in global simulations to save
 548 resources. As a consequence, the simulated summer stratification on temperate shelves is
 549 too strong and its spatial extension too large, covering also the shallow areas otherwise
 550 subject to strong tidal mixing (Fig. 9d-f; Holt et al., 2017; Mathis et al., 2018).

551 The strength of the seasonal stratification as simulated by ICON-Coast (Fig. 9a-c) is in
 552 good agreement with regional high-resolution model studies (Graham et al., 2018b; Guihou
 553 et al., 2018) as well as observation-based estimates of the position of the tidal front (Bianchi

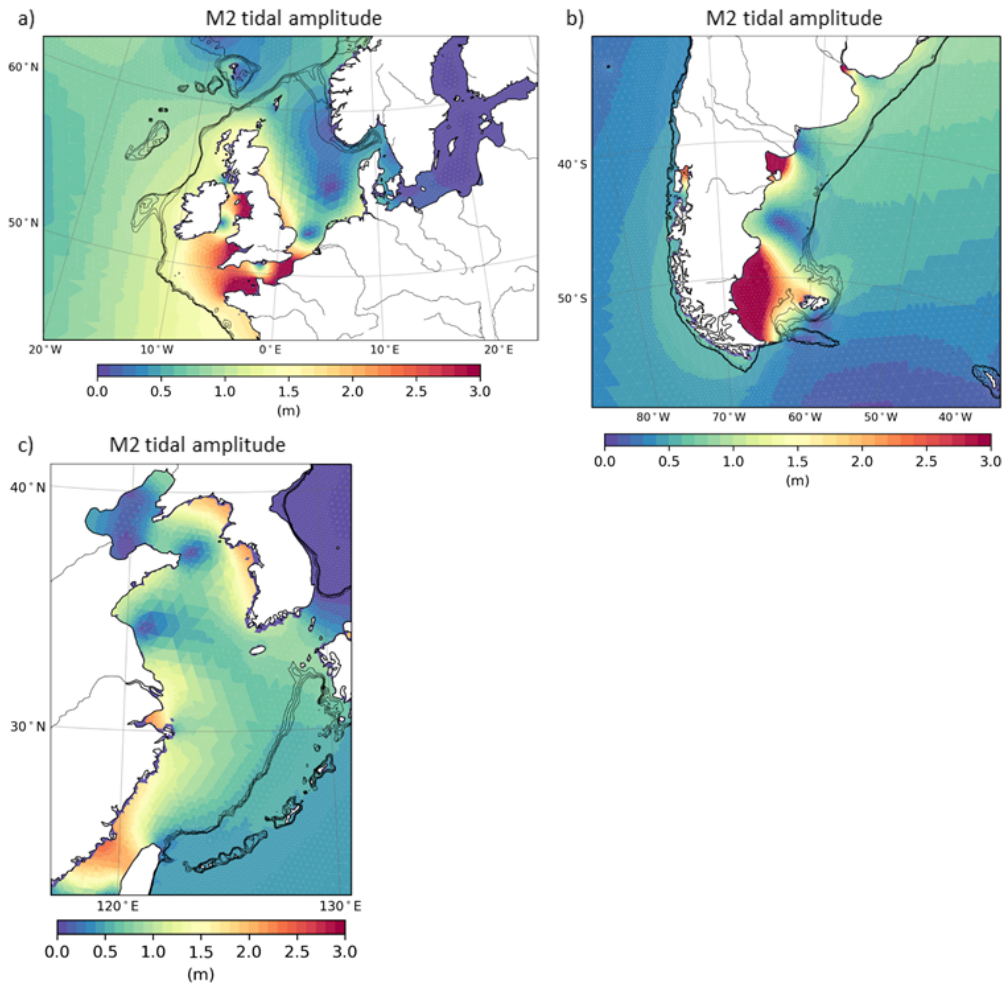


Figure 8: Tidal amplitudes of the semi-diurnal component M2 on the Northwest European Shelf (a), the Patagonian Shelf (b), and East China Shelf (c), simulated with high-res configuration. Isobaths illustrate the shelf break at water depths of 200-500 m.

et al., 2005; Yao et al., 2012; Kahl et al., 2017). For the North Sea, Pättsch et al. (2017) provide a comparison of the potential energy anomaly (PEA) between observations and state-of-the-art regional model systems for August of the period 1998-2009. The PEA quantifies the amount of energy required to vertically mix the entire water column, and hence is often used to evaluate vertical density distributions. The PEA of August calculated for ICON-Coast well reflects the main characteristics given in Pättsch et al. (2017), with values of $100\text{-}200\text{ J m}^{-3}$ in the stratified areas of the central and northern North Sea, maxima exceeding 500 J m^{-3} in the Norwegian Trench, $10\text{-}50\text{ J m}^{-3}$ in most parts of the weakly stratified southern North Sea, and minima below 1 J m^{-3} in the Southern Bight. On the PS, the stratification seems too weak on the southern shelf compared to Kahl et al. (2017) but fits better with the pattern derived by Bianchi et al. (2005). Both studies analyze observational data of 5-7 year periods prior to our analysis period 2006-2010. Nevertheless, the transition from stratified to vertically mixed conditions is mainly determined by the local tidal current speed, the water depth, and the thermal forcing depending on the time of the year. The positions of tidal fronts are therefore rather stable with low interannual variability (E. A. Acha et al., 2004; Holt & Proctor, 2008). The rather weak stratification on the southern PS thus can be attributed to the overestimated tidal currents (section 3.2.2). In the ECS, the summer stratification is exceptionally strong due to cold water transported by the Yellow Sea Warm Current to the central ECS in winter (Z. Liu, Gan, et al., 2021).

Nevertheless, local features like intermittent stratification in shallow coastal areas (van Leeuwen et al., 2015) or a distinct haline stratification in river plumes might not be captured adequately due to the relatively coarse vertical resolution with layer thicknesses of 10 m in the upper 100 m and 16 m in the surface layer (section 2.4). Simulated maximum vertical salinity gradients in the vicinity of large rivers, such as the Yangtze on the ECS and the La Plata north of the PS, reach about 0.25 psu m^{-1} , in contrast to observations and high-resolution regional modeling studies, reporting values of $0.25\text{-}1.0\text{ psu m}^{-1}$ in the first 10 m of the water column (e.g. M. Acha et al., 2008; Z. X. Zhou et al., 2019; Z. Liu, Zhang, et al., 2021).

3.2.4 *Sediment resuspension*

Another important effect of tidal currents is their contribution to the strong benthic-pelagic coupling of temperate shelves (Fig. 1 index 3). Elevated flow speeds near the bottom are known to induce critical bed shear stresses that lead to resuspension of deposited particulate matter (Wilson & Heath, 2019). Areas with strong tidal currents thus typically have very low carbon stocks in the sediment ($<1\%$ TOC dry weight in the upper 10 cm) and essentially net zero accumulation rates (Legge et al., 2020; Diesing et al., 2021). As a consequence, such areas do not function as significant long-term carbon storage. The resuspension of settled organic material and nutrient-rich pore water from sediments back to the water column, though, delivers nutrients for pelagic organisms (F. Liu et al., 2014). This mechanism contributes to the high biological productivity and CO_2 uptake in tidally mixed areas of temperate shelves in summer. The enhanced turbidity due to resuspended particulate matter, however, also reduces irradiance and thus can negatively affect phytoplankton growth (Loebl et al., 2009; Su et al., 2015; Zhao et al., 2019).

In ICON-Coast, we have implemented a sediment resuspension scheme following Mathis et al. (2019). Critical bed shear stresses and the fraction of deposited material that is eroded are inferred from the near-bottom flow speed and the mean density and grain size of the sediment composition. This dynamical approach enables the simulation of the seasonal cycle of sediment stability and wind-induced resuspension. For our developments, we have initialized the sediment from one of the historical simulations by MPI-ESM used here for direct comparison. This model, however, did not account for resuspension processes and therefore maintained a largely uniform distribution of highly overloaded carbon contents in coastal sediments, exceeding 20% TOC dry weight (Fig. 10d-f).

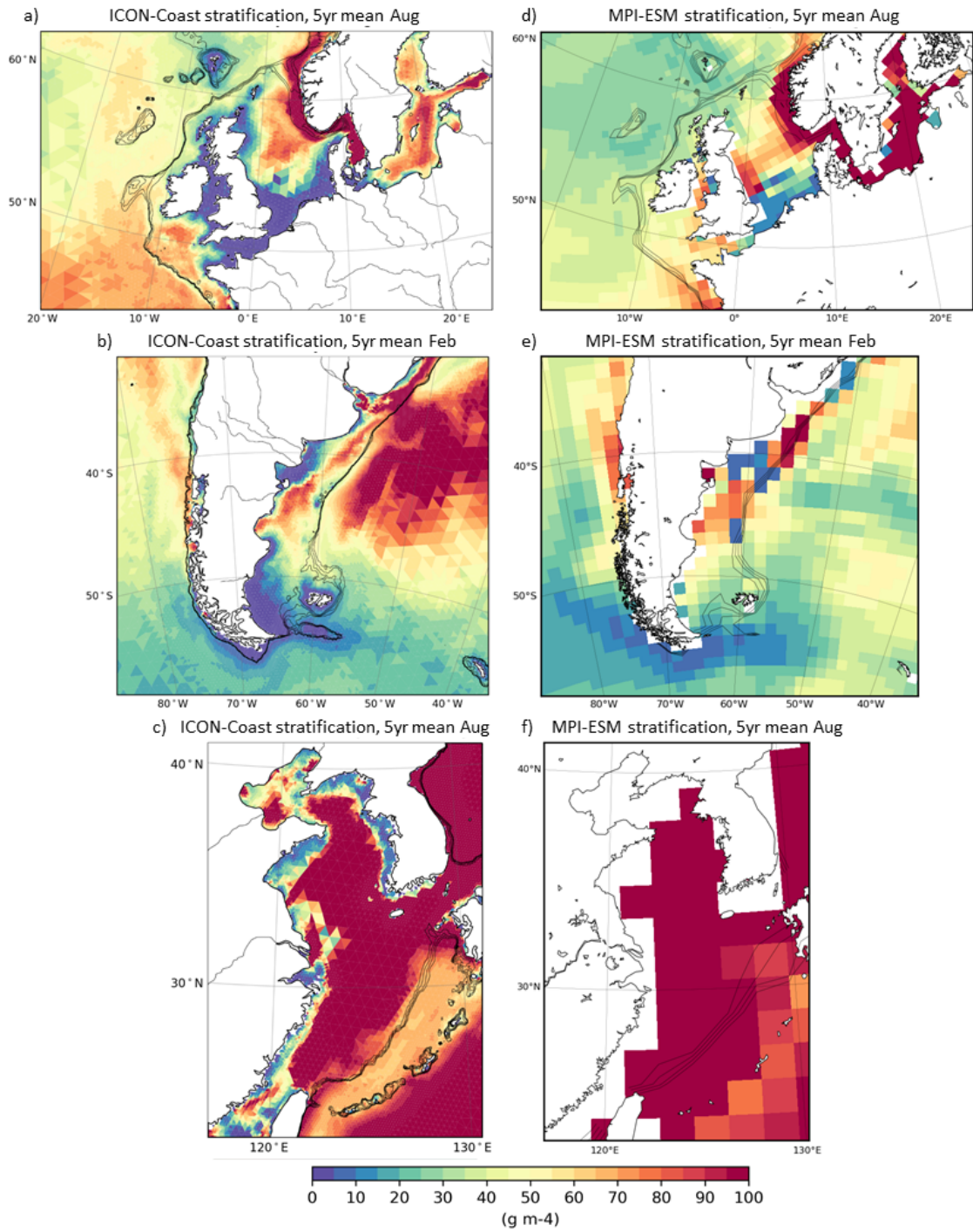


Figure 9: Strength of summer stratification (maximum vertical density gradient) on the Northwest European Shelf (a,d), Patagonian Shelf (b,e) and East China Shelf (c,f), simulated with ICON-Coast high-res configuration (a-c) and MPI-ESM (d-f). Isobaths illustrate the shelf break at water depths of 200-500 m.

605 During the first decades simulated by ICON-Coast, much of the deposited carbon gets
 606 eroded from the sediment and remineralized in the water column (Fig. 10a-c). As we started
 607 the model development by implementing the resuspension scheme, the sediment distribution
 608 shown from ICON-Coast results from an integration time of about 40 years in total (see
 609 section 2.4). The patterns of low carbon content ($< 1\%$ TOC dry weight) on the NWES are
 610 generally in line with measured distributions shown in Legge et al. (2020) and tide-induced
 611 high bed shear stresses reported by Wilson & Heath (2019). On the PS, the simulated
 612 carbon content reflects the observed sediment composition given in Violante et al. (2014).
 613 Over large PS areas, the sediment is dominated by sands and gravels, associated with low
 614 carbon concentrations (Diesing et al., 2017). Muddy sediments with high carbon concen-
 615 trations are found along the shelf break and in the coastal bays between 39-48°S. Similarly
 616 in ICON-Coast, the shelf break as well as the coastal bays on the PS are less affected by
 617 resuspension and hence keep elevated carbon fractions in the sediment. Maximum simu-
 618 lated concentrations in these accumulation areas reach up to 220 kg C m^{-3} in the uppermost
 619 sediment layers. L. M. Hu et al. (2011) and Yang et al. (2014) provide identifications of mud
 620 deposition centers on the ECS based on sediment core sampling. As indicated in Fig. 10c,
 621 ICON-Coast is able to capture the large deposition area in the center of the Yellow Sea as
 622 well as the higher carbon contents in the Bohai Sea.

623 In deeper shelf areas, bed shear stresses are generally weaker and critical values are
 624 rather caused by wind events (e.g. Wilson & Heath, 2019). Accordingly, net erosion rates are
 625 lower and the adjustment of the simulated sediment state takes more time. This is reflected
 626 by a longer drift in the carbon content for instance in the north-eastern part of the North Sea
 627 (Fig. 10a) and the outer shelf areas of the ECS (Fig. 10c). In these regions, relative organic
 628 carbon concentrations are still higher than in observations by a factor of about 5. Similarly,
 629 POC burial rates in the southern and western North Sea are less than $2 \text{ g C m}^{-2} \text{ yr}^{-1}$, and
 630 vary around $40\text{-}70 \text{ g C m}^{-2} \text{ yr}^{-1}$ in the Norwegian Trench, which is comparable to the rates
 631 derived from sediment cores, ranging from 0.02 to $66.18 \text{ g C m}^{-2} \text{ yr}^{-1}$ (Diesing et al., 2021).
 632 In the central and northeastern parts of the North Sea, where the sediment is still overloaded
 633 in our experiments, burial rates are simulated about $10\text{-}30 \text{ g C m}^{-2} \text{ yr}^{-1}$, in contrast to less
 634 than $5 \text{ g C m}^{-2} \text{ yr}^{-1}$ found by Diesing et al. (2021). The model drift in global carbon burial
 635 rates are shown in Fig. 11. At the end of the presented low-res simulation, burial rates of
 636 particulate organic and inorganic carbon on the shelves (0-500 m depth) amount to 0.62 and
 637 $0.15 \text{ Gt C yr}^{-1}$, respectively. The POC burial rate, however, seems overestimated compared
 638 to observation-based upscalings, which are not well constrained, though, ranging between
 639 0.04 and 0.3 Gt C yr^{-1} (Duarte et al., 2005; Burdige, 2007). The relative contribution of 75%
 640 simulated global POC burial occurring on the shelves is similar to about 80% estimated by
 641 Burdige (2007) and Bauer et al. (2013).

642 *3.2.5 Sinking of marine aggregates*

643 As another process extension of ICON-Coast, we have included an aggregate sinking
 644 scheme for particulate matter in the water column, following Maerz et al. (2020). Sinking
 645 organic and inorganic particles in the ocean tend to stick together by physical aggregation
 646 and form particulate assemblages known as marine aggregates. The variable buoyancy of
 647 marine aggregates, determined by their size and density, is associated with variable set-
 648 tling velocities that affect the vertical export of sequestered carbon out of the biologically
 649 productive euphotic zone (Fig. 1 index 4; Francois et al., 2002). This mechanism crucially
 650 contributes to the drawdown of atmospheric CO_2 , as any resulting imbalance in sea wa-
 651 ter pCO_2 near the ocean surface induces CO_2 gas exchange with the atmosphere (Volk &
 652 Hoffert, 1985; Kwon et al., 2009).

653 Global models usually parameterize the attenuation of vertical POC fluxes through an
 654 empirical fit to observations (Gloege et al., 2017). Power law parameterizations or expo-
 655 nential decay rates are most widely used. Such approaches, however, lack a mechanistic
 656 understanding and are aligned to present-day relations between primary production and

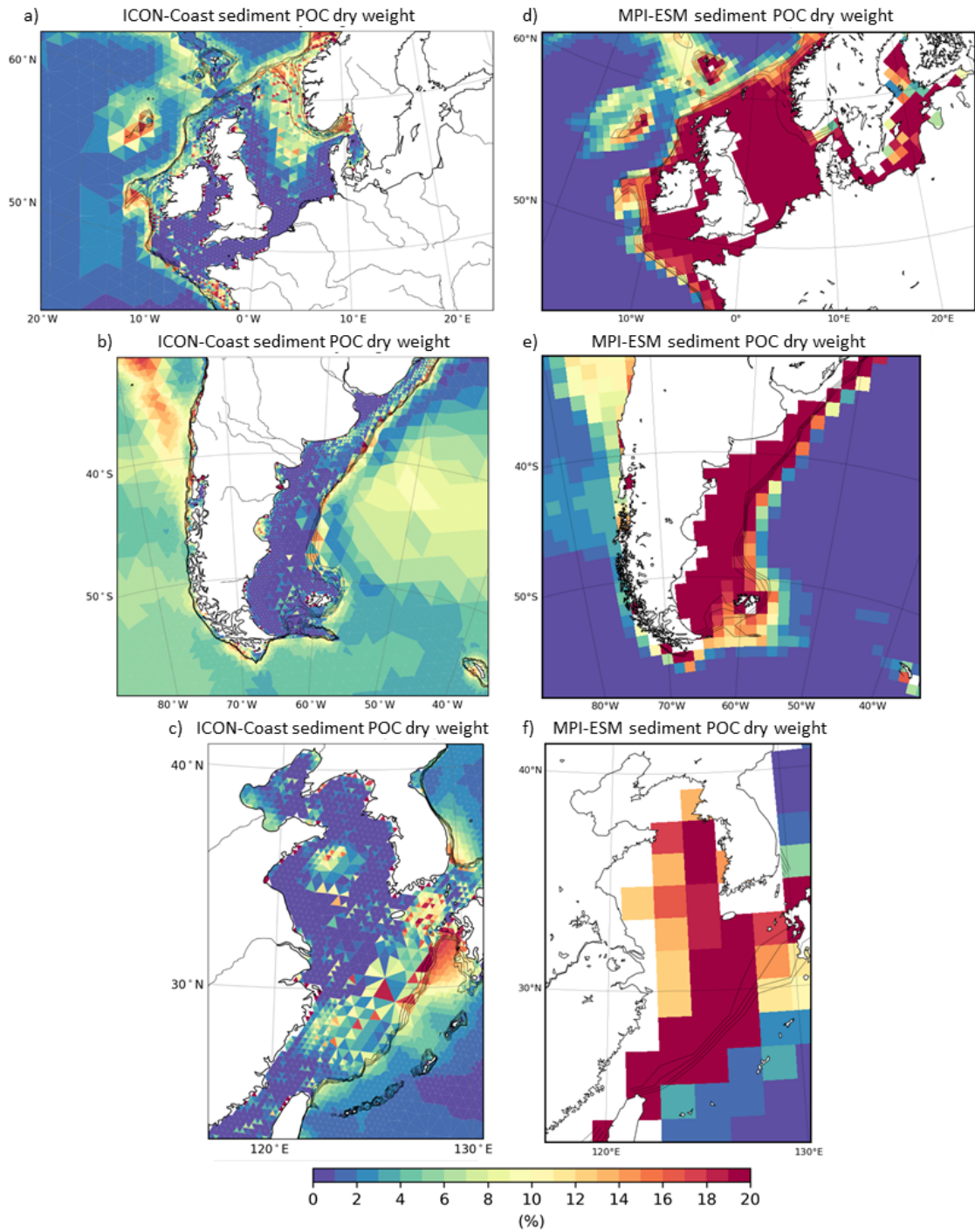


Figure 10: Dry weight of organic carbon in the upper 10 cm of the sediment on the Northwest European Shelf (a,d), Patagonian Shelf (b,e) and East China Shelf (c,f), simulated with ICON-Coast low-res configuration (a-c) and MPI-ESM (d-f). Isobaths illustrate the shelf break at water depths of 200-500 m.

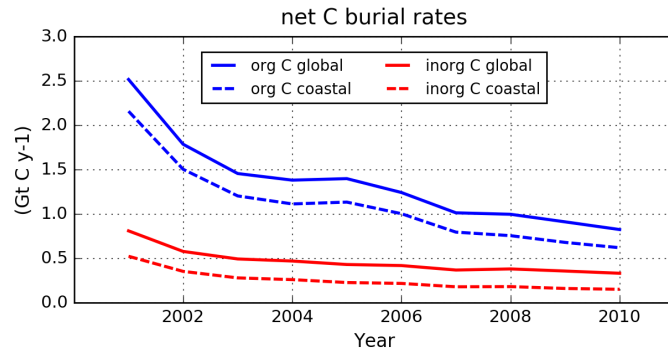


Figure 11: Time series of annual sediment burial rates of organic (blue) and inorganic (red) particulate matter, simulated by the low-res configuration. Solid lines: global average; dashed lines: coastal ocean (0-500 m depth).

657 remineralization processes. The sinking scheme of ICON-Coast explicitly represents the
 658 main structural and compositional characteristics of marine aggregates, and ties ballasting
 659 mineral and POC fluxes together. In this way, the model is able to capture main seasonal
 660 characteristics of marine aggregates in middle and high latitudes (Fig. 12; Fettweis et al.,
 661 2014; Maerz et al., 2016; Schartau et al., 2019). In winter, marine primary production is
 662 weak and thus little organic carbon is available to assemble large aggregates. The composi-
 663 tion, therefore, is dominated by high-density mineral components, leading to comparatively
 664 small aggregate sizes and high sinking speeds (Fig. 12a). During summer, high productivity
 665 delivers organic carbon to form biogenic aggregates of larger sizes but lower excess densi-
 666 ties, and thus reduced sinking speeds (Fig. 12b). In the open ocean and stratified shelf areas
 667 (Fig. 12 north of 54°N), the carbon content gets remineralized while the aggregates sink
 668 to deeper levels, and accordingly the aggregates decompose, become more compacted and
 669 achieve higher settling velocities. In tidally mixed areas (Fig. 12 south of 54°N), by contrast,
 670 sediment resuspension prevents mineral components such as plankton shells and terrestrial
 671 dust to become deposited (Babin & Stramski, 2004; Vantrepotte et al., 2012). The aggre-
 672 gates therefore accommodate larger fractions of mineral components, keeping sizes smaller
 673 and sinking speeds higher throughout the year. It is worth mentioning that all simulated
 674 seasonal aspects of aggregate composition, size and sinking speed emerge from the internal
 675 model formulation without prescribing any element of seasonality.

676 Another factor controlling the turnover rates of organic carbon in the coastal ocean
 677 is the age of organic material settled to the sediment. Fresh, dead material in sediments
 678 of shallow areas is generally more attractive as source of carbon and energy for benthic
 679 organisms than older, more refractory material typically found in deeper areas (Arndt et
 680 al., 2013; O’Meara et al., 2018). The heterotrophic recycling of carbon and nutrients is thus
 681 accelerated in sediments of shallow areas, potentially stimulating high biological productivity
 682 by the resupply of nutrients to otherwise depleted surface waters (Fig. 1 indexes 3 and
 683 5). As our model does not incorporate metabolic reworking of organic matter by benthic
 684 communities, we approximate this age effect by a modification of the remineralization rate
 685 constant of detritus deposited at water depths of up to 500 m, assigning linearly decreasing
 686 values with increasing depth from 0.06 to 0.013 d⁻¹ at a reference temperature of 10°C.
 687 These values are aligned to the range investigated by Lacroix et al. (2021a), though a more
 688 mechanistic parameterization including bioturbation in the upper sediment, as e.g. proposed
 689 by Stolpovsky et al. (2015) or Zhang & Wirtz (2017), would be a further improvement.

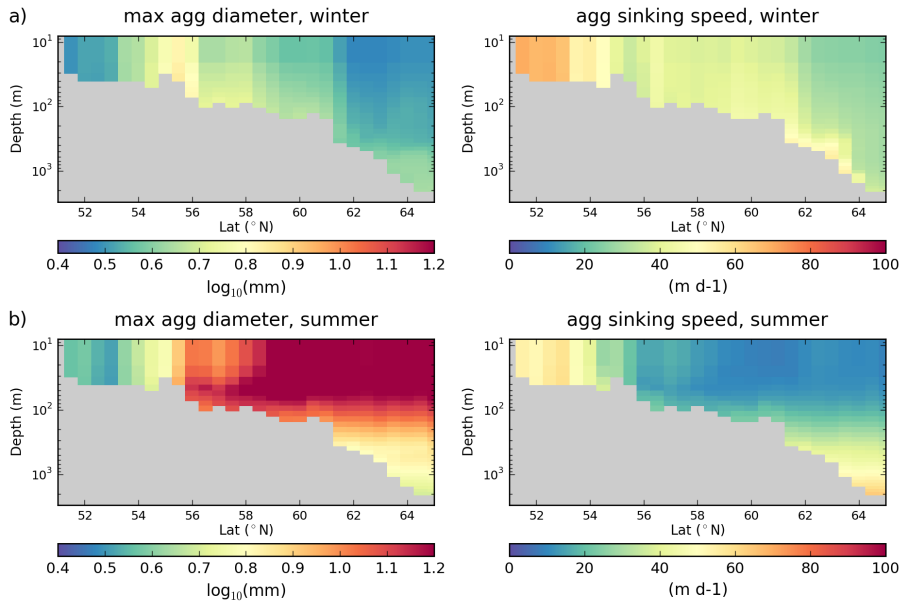


Figure 12: Maximum diameter (left) and mean sinking speed (right) of marine aggregates in winter (a) and summer (b) along a meridional transect through the North Sea at 2.5°E , simulated with low-res configuration.

690 3.2.6 River inputs

691 The importance of riverine carbon, alkalinity, and nutrient inputs for addressing re-
 692 gional carbon dynamics at the global scale was recently highlighted by Hauck et al. (2020)
 693 and Lacroix et al. (2020, 2021b). In conventional global biogeochemistry models, net par-
 694 ticulate export fluxes to the sediment would violate the conservation of global budgets and
 695 induce long-term inventory drift as well as artificial gas exchange with the atmosphere.
 696 Burial losses are therefore typically balanced by instantaneous remineralization and diffu-
 697 sive resupply to the water column (Najjar et al., 2007) or by prescribed uniform weathering
 698 fluxes at the sea surface (Ilyina et al., 2013). In ICON-Coast, weathering fluxes and an-
 699 thropogenic nutrient loadings are provided by spatially explicit river inputs (Fig. 1 index
 700 6). This approach accounts for the influences of matter fluxes from land on the coastal
 701 carbon dynamics and allows to integrate regional, inter-compartmental fluxes as well as im-
 702 balances in global inventories under different environmental conditions and human activities
 703 (Tamburini & Föllmi, 2009; Wallmann, 2010; Beusen et al., 2016).

704 Rivers are responsible for the largest export of tDOM to the ocean with an annual flux
 705 of about 200 Tg C yr^{-1} (Bauer et al., 2013; Kandasamy & Nath, 2016), thus significantly
 706 increasing the pCO_2 of the coastal ocean (Lacroix et al., 2020). In our simulations, about
 707 50% of the global terrestrial carbon input is decomposed in the coastal ocean (water depth
 708 $< 200 \text{ m}$), lying well within the estimated range of 35-55% given in the literature (Fichot &
 709 Benner, 2014; Kaiser et al., 2017; Aarnos et al., 2018). In the broad shelf seas considered
 710 here, decomposition proportions are higher due to longer residence times of near-coastal
 711 waters (Lacroix et al., 2021a), with simulated values of 58% (of 2.1 Tg C yr^{-1}) on the NWES,
 712 67% (of 0.8 Tg C yr^{-1}) on the PS, and 85% (of 6.4 Tg C yr^{-1}) on the ECS. Other riverine
 713 substances directly affecting the surface CO_2 flux are the loadings of alkalinity and dissolved
 714 inorganic carbon. As these rarely deviate from each other by more than 10% (Araujo et al.,
 715 2014; Middelburg et al., 2020), we use a mole ratio of 1:1 following Lacroix et al. (2020),
 716 which leads to a further increase in near-coastal pCO_2 .

3.2.7 Primary production

A characteristic feature of many shelf seas is their exceptionally high biological productivity, which is one of the most essential drivers to lower $p\text{CO}_2$ in coastal surface waters of middle latitudes and foster CO_2 ingassing (Muller-Karger et al., 2005; Gattuso et al., 1998). Key processes mediating enhanced phytoplankton growth are: import of nutrient-rich water masses from the adjacent open ocean, additional continuous nutrient supply via river loads, fast internal nutrient recycling, and often strong tidal mixing, which prevents deposition of biologically bound nutrients in the sediment (Dai et al., 2013; Cao et al., 2020). In addition to river loads from land, we prescribe atmospheric dust (Fe) and nitrogen deposition following Mauritsen et al. (2019), which provides another source of inorganic nutrients for marine primary production.

The simulated annual net primary production on the NWES (Fig. 13a) well captures the high phytoplankton growth rates in the near-coastal zones around the British Islands and along the continental coast of the southern North Sea, as well as the strong gradients to the open shelf areas of the central and northern North Sea (Moll, 1998; Provoost et al., 2010; Holt et al., 2012, 2016; Williams et al., 2013). Similarly, the seasonal cycle averaged over the southern and northern North Sea (Fig. 14), separated by the 50 m isobath, well reflects the spring bloom and summer growth seasons (compare to Moll, 1998; Lemmen, 2018). Simulated annual primary production of the entire North Sea is about $160 \text{ g C m}^{-2} \text{ yr}^{-1}$, falling within the range of $100\text{-}230 \text{ g C m}^{-2} \text{ yr}^{-1}$ given in the cited observational and regional model studies. Satellite-derived primary production is shown in Fig. A2a,b, with an estimated North Sea productivity of about $150\text{-}160 \text{ g C m}^{-2} \text{ yr}^{-1}$. These estimates, however, are sensitively dependent on the utilized satellite data and NPP algorithms (Campbell et al., 2002; Carr et al., 2006), e.g. varying by a factor of 2-4 in coastal primary production among the products provided by the Ocean Productivity service (<http://sites.science.oregonstate.edu/ocean.productivity/index.php>). Maximum simulated annual productivity in the southern North Sea is about $330 \text{ g C m}^{-2} \text{ yr}^{-1}$, compared to $270\text{-}380 \text{ g C m}^{-2} \text{ yr}^{-1}$ measured by Capuzzo et al. (2018), and the simulated spring bloom peaks at $580 \text{ g C m}^{-2} \text{ yr}^{-1}$ in the Southern Bight, which is associated with a considerable observational range of $180\text{-}730 \text{ g C m}^{-2} \text{ yr}^{-1}$ reported in Moll (1998). Locally reduced phytoplankton growth measured close to the continental coast (e.g. Capuzzo et al., 2018), however, is not captured by ICON-Coast, as the impact of suspended particulate matter on light conditions is not yet implemented.

The PS is another highly productive shelf sea with an annual net primary production of about $350 \text{ g C m}^{-2} \text{ yr}^{-1}$ according to measurements by Gonçalves-Araujo et al. (2016); Piola et al. (2018), and $180\text{-}210 \text{ g C m}^{-2} \text{ yr}^{-1}$ derived by satellite products (Fig. A2c,d). A comparably high phytoplankton growth of $240 \text{ g C m}^{-2} \text{ yr}^{-1}$ is simulated by ICON-Coast (Fig. 13b). In observations, a persistent local maximum of Chl-a concentrations is found along the northern part of the PS shelf break, caused by shelf break upwelling of the northward flowing Malvinas Current (Carreto et al., 2016; Franco et al., 2017). In the low-res simulations, elements of enhanced primary production along the shelf break are also indicated, in spite of slope currents and upwelling transports being underestimated due to unresolved mesoscale processes.

On the ECS, the productivity in the near-coastal zone is strongly influenced by riverine nutrient loads (Fig. 13c), similar to the NWES. In observational products as well as in our simulations, local maxima in net primary production of up to $700 \text{ g C m}^{-2} \text{ yr}^{-1}$ are found in the river plumes of the Yangtze and Yellow Rivers, discharging at the Chinese coasts of the Yellow Sea and Bohai Sea, respectively (Tan & Shi, 2006). Also the seasonal cycle with two pronounced phytoplankton blooms in spring and late summer is captured by ICON-Coast (not shown), with a spring bloom though underestimated by about 20% compared to G. Li et al. (2004); Tan & Shi (2012) and Luo (2014). Annual productivity is simulated about $250 \text{ g C m}^{-2} \text{ yr}^{-1}$, compared to $180\text{-}360 \text{ g C m}^{-2} \text{ yr}^{-1}$ by the two satellite products shown in Fig. A2e,f.

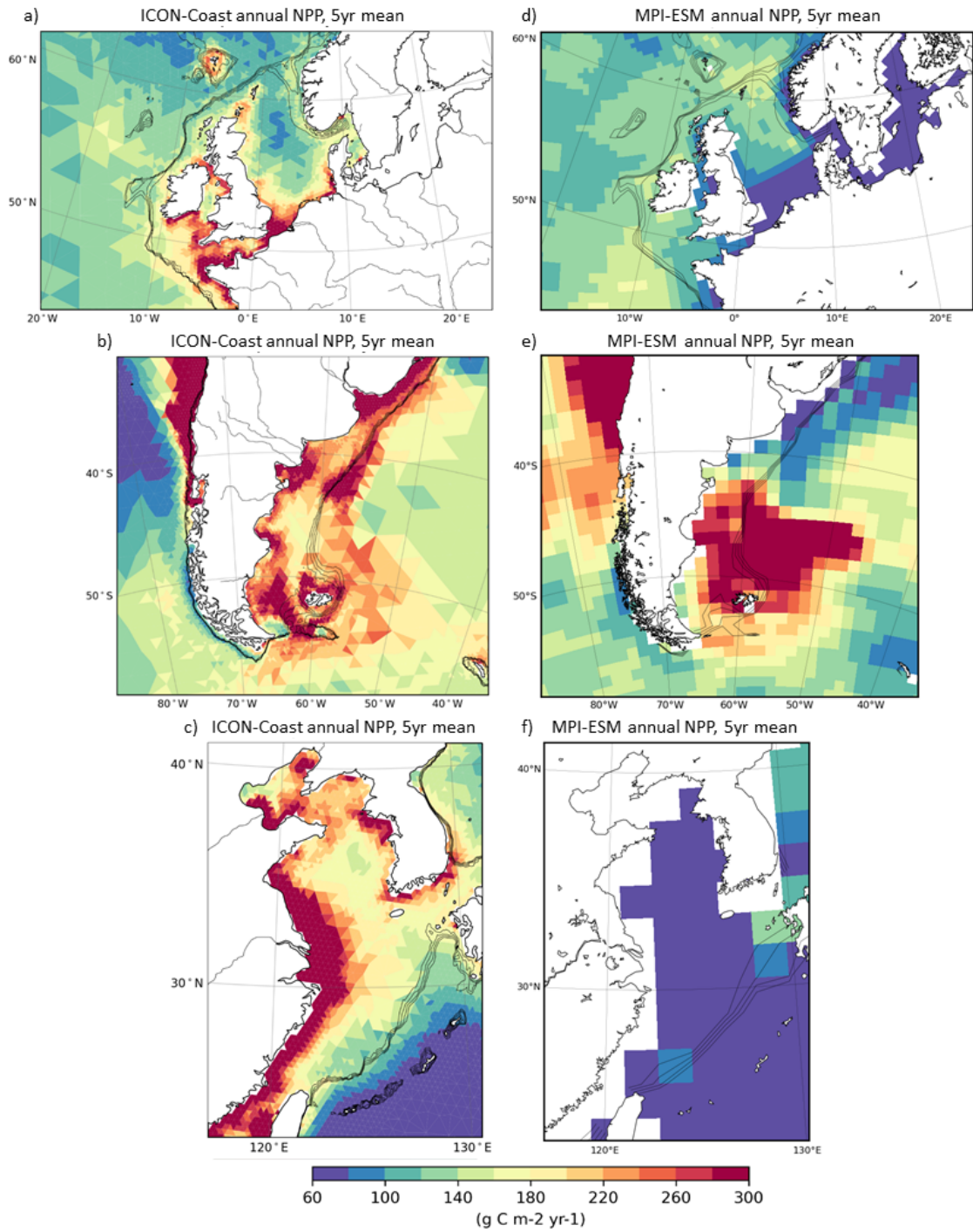


Figure 13: Annual depth-integrated net primary production on the Northwest European Shelf (a,d), Patagonian Shelf (b,e) and East China Shelf (c,f), simulated with ICON-Coast low-res configuration (a-c) and MPI-ESM (d-f). Isobaths illustrate the shelf break at water depths of 200-500 m.

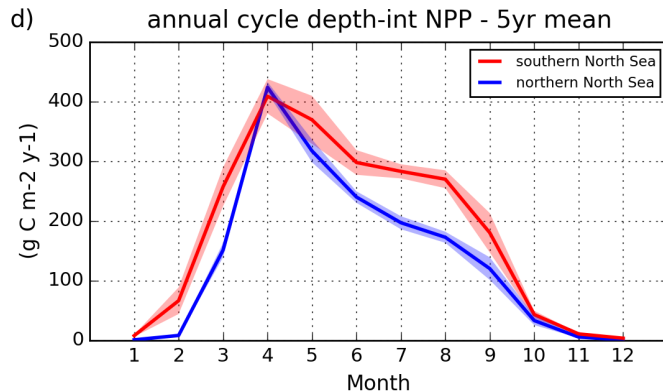


Figure 14: Seasonal cycle in the northern and southern North Sea, simulated with low-res configuration.

770 In conventional global biogeochemistry models, missing factors sustaining enhanced
 771 coastal primary production, such as river inputs, sediment resuspension and often the in-
 772 fluence of temperature on particulate matter decomposition, lead to substantially underes-
 773 timated primary production in shelf and marginal seas (Fig. 13d-f). Regions are less biased
 774 where import of nutrient-rich water masses from the open ocean are the main source of
 775 nutrients, as e.g. on the PS (Fig. 13e).

776 3.2.8 Surface CO₂ flux

777 In temperate shelf seas, the high biological productivity and export of dissolved inor-
 778 ganic carbon is typically associated with a net heterotrophic state and CO₂ uptake from
 779 the atmosphere (Fig. 1 index 7; Kühn et al., 2010; Becker et al., 2021; Tseng et al., 2011).
 780 In the near-coastal zone, river loads play an important role for the air-sea gas exchange at
 781 the global scale, as a substantial amount of the CO₂ uptake is caused by biological con-
 782 sumption of riverine inorganic nutrients and the resulting alkalinity production (Hauck et
 783 al., 2020; Lacroix et al., 2020). Moreover, the mixing of high-pCO₂ river runoff with low-
 784 pCO₂ sea water has been found to induce strong CO₂ uptake in brackish waters of several
 785 large river plumes across latitudes, such as the Yangtze and Mississippi plumes (Tseng et
 786 al., 2011; Huang et al., 2015; Kealoha et al., 2020). In most high- and low-latitude coastal
 787 regions, the temperature effect on the CO₂ solubility of sea water exceeds the biological
 788 CO₂ drawdown, leading to net CO₂ outgassing in low latitudes (G. G. Laruelle et al., 2010;
 789 Mayer et al., 2018) and net uptake in high latitudes (K. Arrigo et al., 2008; Yasunaka et
 790 al., 2016, 2018). This characteristic is generally captured by ICON-Coast (Fig. 15). The
 791 range between CO₂ uptake and outgassing, though, is smaller in the coastal ocean than in
 792 the open ocean. Riverine carbon input weakens the uptake in coastal regions of northern
 793 high latitudes, whereas continuous productivity in low latitudes has a net weakening effect
 794 on the CO₂ flux to the atmosphere. On the southern hemisphere, zonally integrated shelf
 795 areas south of about 20°S are comparatively small. Here, the indicated deviations between
 796 the coastal and open ocean fCO₂ are thus probably overestimated due to the positive bias
 797 on the PS (see below) and the negative bias in the open Southern Ocean (see section 3.1).

798 For the three focus areas, simulated surface CO₂ fluxes (fCO₂) are shown in Fig. 16.
 799 Because of the mixture of driving the model with a modern climate but preindustrial pCO₂
 800 (see section 2.4), the resulting fCO₂ are not fully comparable with present-day observations.
 801 In our experiments though, the spatial structures of fCO₂ in the coastal ocean are relatively
 802 insensitive to variations in atmospheric pCO₂ ranging from preindustrial to present-day
 803 levels. We therefore focus more on the qualitative fCO₂ distributions and gradients here
 804 and reflect on the magnitudes of the fluxes in the discussion section 4.

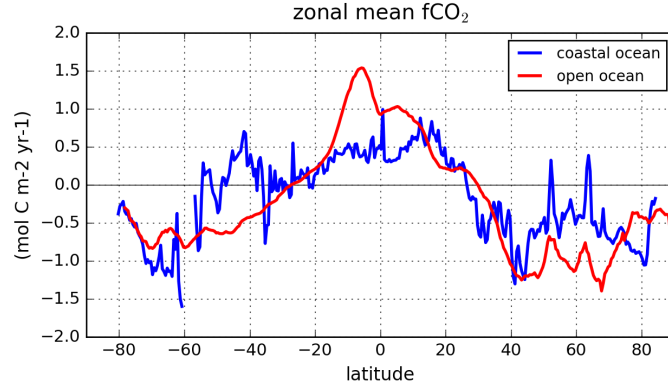


Figure 15: Zonally averaged ocean-atmosphere CO_2 flux for open (red) and coastal (blue; water depth < 500 m) ocean, simulated by the low-res configuration. Positive values refer to oceanic outgassing. The zonal average for the entire ocean is shown in Fig. 4.

805 The northern North Sea and outer shelf areas of the NWES are known to be net sinks for
 806 atmospheric CO_2 under present-day climatic conditions, while the shallow southern North
 807 Sea is close to neutral (Thomas et al., 2004; Marrec et al., 2015; Kitidis et al., 2019; Becker
 808 et al., 2021). This structure is qualitatively reproduced in our ICON-Coast simulations
 809 (Fig. 16a) with an annual mean uptake in the North Sea of about $0.8 \text{ mol C m}^{-2} \text{ yr}^{-1}$.

810 The PS is a significant net carbon sink likewise (Kahl et al., 2017). Tidally mixed
 811 coastal areas, however, are dominated by CO_2 outgassing in austral summer (Bianchi et al.,
 812 2005). This seasonal feature is also captured by ICON-Coast (Fig. 16b). In the northern
 813 part of the PS, though, the outgassing signal is overestimated and extends into the stratified
 814 area of the open shelf.

815 The ECS is simulated as an efficient shelf carbon pump (Fig. 16c). The East China Sea
 816 acts as a strong carbon uptake area and the Yellow Sea and Bohai Sea as rather weak ones,
 817 which is consistent with observations (Tseng et al., 2011; Jiao et al., 2018; Song et al., 2018).
 818 Moreover, the seasonal cycle of fCO_2 in the East China Sea measured by Tseng et al. (2011)
 819 is qualitatively well captured by ICON-Coast, with a simulated maximum uptake of about
 820 $3 \text{ mol C m}^{-2} \text{ yr}^{-1}$ in winter (bias $-1.5 \text{ mol C m}^{-2} \text{ yr}^{-1}$) and a weak outgassing of maximum
 821 $0.5 \text{ mol C m}^{-2} \text{ yr}^{-1}$ (bias $-0.1 \text{ mol C m}^{-2} \text{ yr}^{-1}$) in summer, averaged over the same region
 822 investigated in that study.

823 The CO_2 flux at the sea surface is a sensitive metric of the coastal carbon dynamics,
 824 as it is affected directly or indirectly by all physical and biogeochemical processes discussed
 825 in this section. To provide an outlook of the model skills also in coastal areas other than
 826 the temperate shelves, we briefly elaborate on the simulated fCO_2 for the Sunda Shelf (as
 827 an example of a large low latitude shelf) and the coastal ocean of the Arctic (as an example
 828 of a high latitude region).

829 In our simulations, the whole Sunda Shelf is releasing CO_2 to the atmosphere on annual
 830 means, consistent with observations and regional model studies (Kartadikaria et al., 2015;
 831 Mayer et al., 2018; Y. Zhou et al., 2021). The winter and summer monsoon winds drive
 832 distinct seasonal circulation regimes on the shelf and lead to a reversed fCO_2 in the northern
 833 part in winter (Mayer et al., 2018). ICON-Coast captures this seasonality (Fig. 17) with an
 834 uptake of up to $1 \text{ mol C m}^{-2} \text{ yr}^{-1}$ near the Gulf of Thailand in winter and an outgassing of up
 835 to $0.8 \text{ mol C m}^{-2} \text{ yr}^{-1}$ in summer, while the southern shelf areas show continuous outgassing
 836 of $0.3\text{-}0.7 \text{ mol C m}^{-2} \text{ yr}^{-1}$ throughout the year. The annual net outgassing for the entire

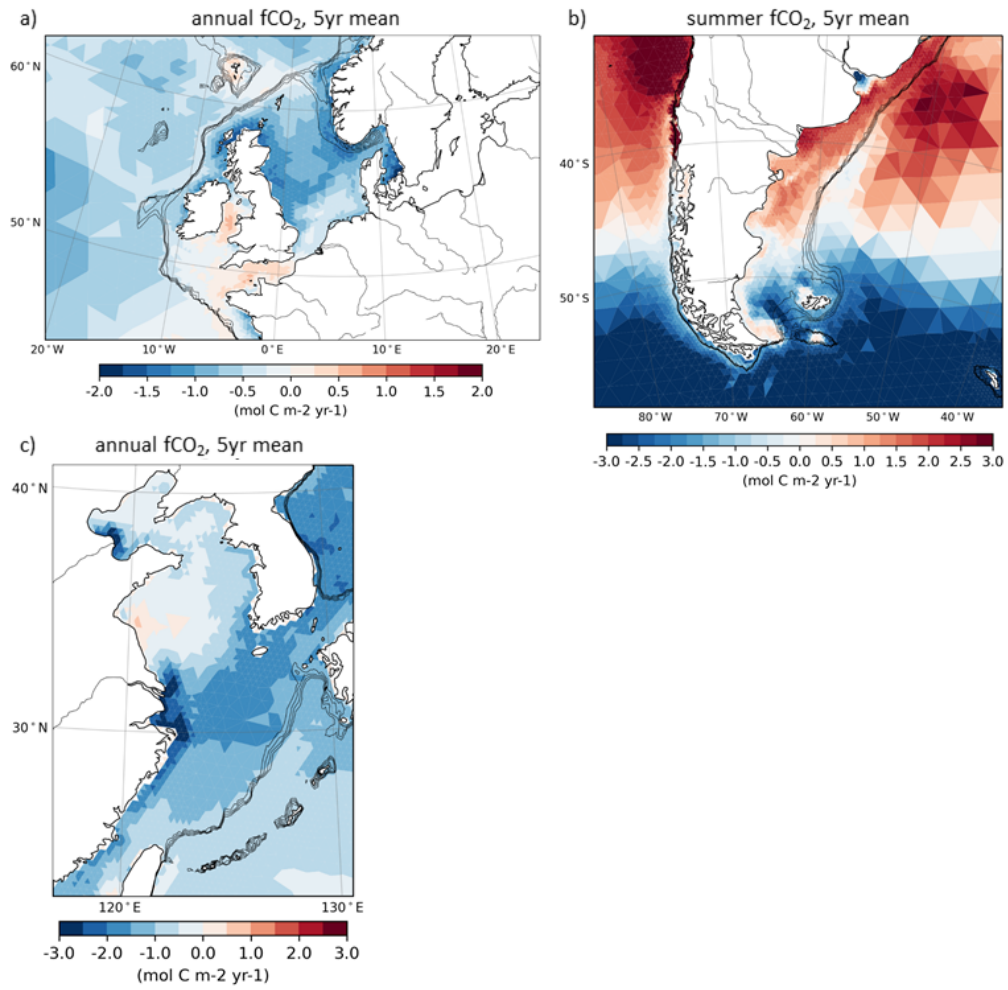


Figure 16: Ocean-atmosphere CO₂ flux for (a) the Northwest European Shelf (annual), (b) Patagonian Shelf (summer), and (c) East China Shelf (annual), simulated by the low-res configuration. Positive values refer to oceanic outgassing. Isobaths illustrate the shelf break at water depths of 200-500 m.

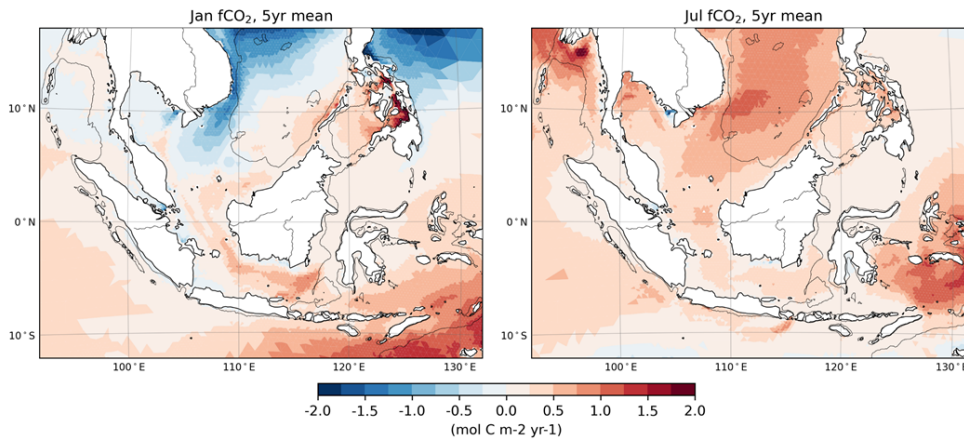


Figure 17: Ocean-atmosphere CO₂ flux on the Sunda Shelf for January (a) and July (b), simulated by the low-res configuration. Positive values refer to oceanic outgassing. The isobath indicates a water depth of 500 m.

837 Sunda Shelf is $0.22 \text{ mol C m}^{-2} \text{ yr}^{-1}$, compared to $0.65 \text{ mol C m}^{-2} \text{ yr}^{-1}$ simulated by Mayer
 838 et al. (2018), who did not account for carbon fixation by phytoplankton.

839 The Arctic ocean accomodates the world's largest continental shelves, extending up to
 840 1500 km from the coast of Siberia into the ocean. Most of these areas draw down atmospheric
 841 CO₂ via biologically mediated pCO₂ reduction during phytoplankton blooms and cooling of
 842 warm water masses intruding from the North Atlantic and Pacific (Bates & Mathis, 2009).
 843 Strong net uptake fluxes exceeding $2 \text{ mol C m}^{-2} \text{ yr}^{-1}$ are simulated by ICON-Coast in the
 844 Barents Sea and the deep water formation sites of the GIN Sea (Fig. 18), in agreement with
 845 multi-year observations by Yasunaka et al. (2016, 2018). Regionally enhanced uptake of more
 846 than $1 \text{ mol C m}^{-2} \text{ yr}^{-1}$ is also indicated in the Chukchi Sea, both in our simulations and field
 847 measurements e.g. by Bates (2006) and Cai et al. (2010). The gradient along the Eurasian
 848 Arctic shelves from high uptake in the western part (Barents Sea) to relatively weak fluxes in
 849 the eastern part was also observed by Pipko et al. (2017), who measured a regional difference
 850 in outer shelf pCO₂ of about 50-100 ppm during fall, compared to about 50 ppm simulated
 851 by ICON-Coast. In the same study, the outgassing along the coasts of the eastern part was
 852 attributed to the influences of river runoff and terrestrial carbon loads. While the spatial
 853 pattern of Arctic fCO₂ is qualitatively well represented, the simulated uptake is generally
 854 weaker than contemporary observations of comparable periods. In the Arctic area used
 855 by Yasunaka et al. (2018), that is north of 65°N, excluding the Greenland and Norwegian
 856 seas and Baffin Bay, the ocean takes up 73 Tg C yr^{-1} in our simulation, compared to the
 857 observational spread of 80-200 Tg C yr^{-1} obtained by Bates & Mathis (2009) and Yasunaka
 858 et al. (2018).

859 Overall, the spatial patterns of seasonal and annual fCO₂ simulated by ICON-Coast for
 860 various regions are consistent with the observational products cited here. In particular the
 861 skill in capturing seasonality is a remarkable improvement, contrasting the large model-data
 862 mismatch on the seasonal time scale of conventional global biogeochemistry models until
 863 now (Hauck et al., 2020). Nevertheless, the net uptake fluxes in middle and high latitudes
 864 are systematically underestimated, which can be attributed to the lower atmospheric pCO₂
 865 of preindustrial levels used in our simulations. Estimates of the change in CO₂ flux due to
 866 the pCO₂ rise during the 20th century, derived from recent global simulations by Lacroix
 867 et al. (2021b), show a clear latitudinal structure, with higher increases in CO₂ fluxes to the
 868 ocean at higher latitudes. We therefore are optimistic that the magnitudes of the net fluxes
 869 simulated by ICON-Coast will get closer to observations of the recent past when we increase
 870 atmospheric CO₂ concentrations to present-day values. We further expect the regional and

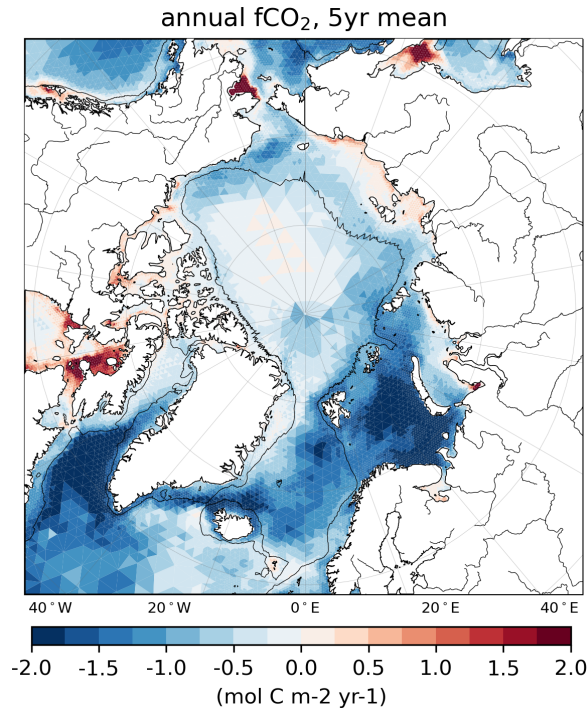


Figure 18: Ocean-atmosphere CO_2 flux for the greater Arctic, simulated by the low-res configuration. Positive values refer to oceanic outgassing. The isobath indicates a water depth of 500 m.

871 seasonal $f\text{CO}_2$ biases e.g. on the PS to get smaller, since they are consistently resulting from
872 too high $p\text{CO}_2$ in the ocean relative to the atmosphere.

873 4 Discussion

874 We have introduced a new global modeling approach aiming to reduce uncertainties in
875 the marine carbon cycle via increased grid resolution in the land-ocean transition zone and
876 enhanced process representation of physical and biogeochemical shelf sea dynamics. Our
877 evaluation therefore focused on the coastal ocean, whereas in the open ocean we expect the
878 global patterns shown in Fig. 3, as well as their spatial integrals, to be still significantly
879 influenced by the initial conditions because of the comparatively short simulation periods of
880 10-20 years. In particular the state of the deep ocean, including the sediment composition,
881 is subject to long-term model drift (Heinze et al., 1999; Palastanga et al., 2011). In many
882 coastal regions, however, the ocean circulation and tracer distribution are rather dominated
883 by short-term regional-scale and even local-scale processes such as tidal mixing, river loads,
884 and the regional atmospheric forcing. In our test simulations, accordingly, most variables
885 on the shelves show a quick response to the external forcing already in the first few years,
886 without a strong discernable drift but a high sensitivity to changes in model-specific pa-
887 rameters (Fig. 19). In particular the spatial patterns and gradients are rapidly developing.
888 Also the nutrient concentrations of open ocean water masses flushing the shelves are rela-
889 tively stable over the simulated period (Fig. 20). These characteristics allow us to gain a
890 basic understanding about the performance of the model in various shelf and marginal seas,
891 although the currently available model runs are relatively short.

892 As known from regional model studies, an increased horizontal resolution in the coastal
893 areas generally improves the spatial manifestation of the implemented physical and bio-
894 geochemical processes (e.g. Mathis et al., 2015; Graham et al., 2018a, 2018b; Guihou et

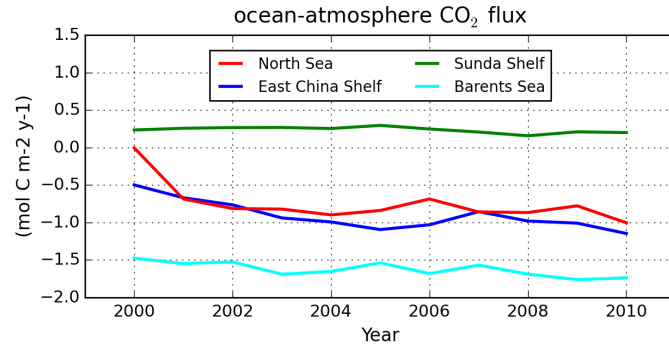


Figure 19: Time series of annual ocean-atmosphere CO₂ flux in various shelf seas, simulated by the low-res configuration. Positive values refer to oceanic outgassing.

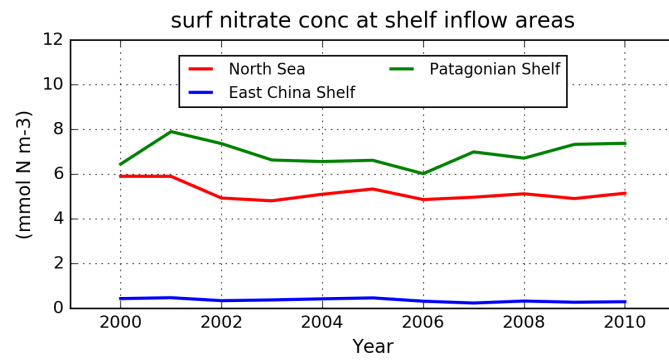


Figure 20: Time series of annual surface nitrate concentrations in main inflow areas of the North Sea (lon 2-4°W, lat 59-61°N), PS (lon 62-64°W, lat 55-57°S) and ECS (lon 123-125°E, lat 25-27°N), simulated by the low-res configuration.

895 al., 2018; de Souza et al., 2020). Moreover, the structure and strength of the general cir-
896 culation, including ocean-shelf exchange, gets more realistic, which affects the distribution
897 of water masses and associated residence times (Pätsch et al., 2017; X. Liu et al., 2019;
898 Lacroix et al., 2021a). The transport rates of boundary and slope currents, for instance, are
899 underestimated in our low-res runs but become more energetic in the high-res simulation,
900 e.g. with increases of the Malvinas Current along the PS by 20% (high-res mean 20.7 Sv
901 at 45°S, literature 20-25 Sv by Frey et al., 2021), the NWES slope current by 35% (high-
902 res mean 2.4 Sv at 58°N, literature 1-4 Sv by Marsh et al., 2017; Clark et al., 2021), and
903 shelf break upwelling velocities by a factor of 4. On the shelves, the general patterns of
904 the circulation and seasonal stratification are comparatively similar in both configurations
905 (Fig. A3), though become more structured and confined in high-res. The representations of
906 the bottom topography and the orography of coastlines are further improved by the unstruc-
907 tured triangular grid due to the smoother horizontal discretization of topographic features
908 compared to the typical staircase approximation by rectilinear grids (e.g. of MPI-ESM). We
909 therefore expect, in particular the influences of cross-shelf transport, coastal upwelling and
910 baroclinic instabilities on net carbon deposition and export rates in the coastal ocean to
911 improve further when we include the biogeochemistry model component also in the high-res
912 setup. In the open ocean, our simulations show that the increase in resolution from 160 km
913 (low-res) to 80 km (high-res) leads to a better representation of the large-scale gyre system
914 (Fig. 21), reduced biases in winter mixed layer depths, and more realistic locations of deep
915 and bottom water formation sites (Fig. 22) in particular in the North Atlantic. The strength
916 of the Atlantic meridional overturning circulation at 26°N is simulated 16.0 Sv with high-res,
917 compared to 11.2 Sv with low-res and 16.8 Sv during 2005-2017 measured by the RAPID
918 time series (Moat et al., 2020), which indicates a generally underestimated large-scale cir-
919 culation in low-res. These differences reflect the typical behavior of global Earth system
920 models to increased resolution (Hewitt et al., 2020). The improved circulation should then
921 also affect the global distribution of biogeochemical tracers such as nutrients (Fig. 3c and
922 Fig. A1), dissolved carbon, and alkalinity.

923 The concept of using unstructured variable-resolution meshes to enhance the quality of
924 a simulation in the region of interest was developed about 1-2 decades ago (e.g. C. Chen et
925 al., 2003; Pain et al., 2005; Piggott et al., 2008; Behrens & Bader, 2009) and has seen sub-
926 stantial progress in recent years concerning optimization, stability, and complexity (Weller
927 et al., 2016; Rémacle & Lambrechts, 2018). Applications of global grid configurations with
928 regional refinement in the coastal ocean, however, were focused on physical ocean modeling
929 so far (D. V. Sein et al., 2017; Hoch et al., 2020; Logemann et al., 2021). Our simulations
930 thus provide a proof-of-concept for an extension of this strategy to include global biogeo-
931 chemistry modeling. For the investigation of single target regions of the coastal ocean, an
932 innovative approach including biogeochemistry was achieved by using stretched global recti-
933 linear grids, utilizing the naturally higher resolution in the vicinity of grid poles (Gröger et
934 al., 2013; D. Sein et al., 2015). The sediment resuspension scheme adapted for ICON-Coast,
935 for example, was first developed for such a system (Mathis et al., 2019). The flexibility of
936 the grid generator used here (Logemann et al., 2021) also allows an assignment of increased
937 resolution to spatially confined areas only, without the limitation of too coarse resolution
938 in pole-distant regions that comes with stretched rectilinear grids. In the vertical, however,
939 we are obliged to use a comparatively thick surface layer (16 m) in our global setup to ac-
940 commodate exceptional negative sea level anomalies in coastal grid cells, resulting from the
941 total of high tidal amplitudes, wind-induced off-shore transport and local sea ice thickness.
942 As a further development, though, we are considering z^* coordinates as an alternative ver-
943 tical grid structure of the model, following the recent work by Singh & Korn (submitted).
944 In a z^* system, the free surface elevation is distributed among all grid layers, thus avoid-
945 ing critical surface layer thicknesses and enabling higher vertical resolution also in shallow,
946 tidally active regions. We expect this to facilitate improvements of simulated stratification
947 dynamics in the near-coastal zone, such as intermittent stratification (van Leeuwen et al.,
948 2015), and related vertical and frontal fluxes of carbon, oxygen and nutrients, which were
949 shown to impact e.g. phytoplankton dilution and phenology (Zhao et al., 2019). Further-

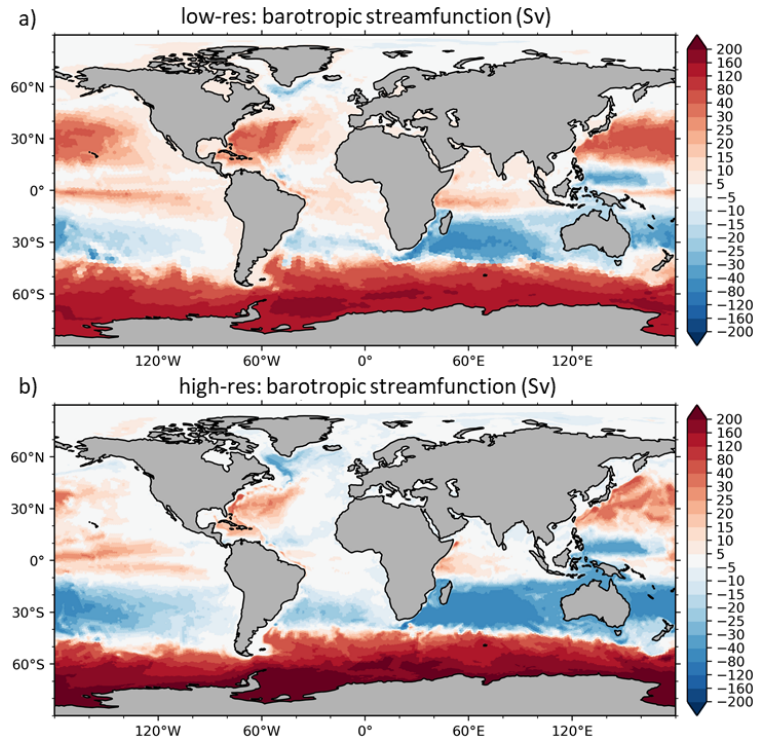


Figure 21: Barotropic streamfunction simulated by the low-res (a) and high-res (b) configurations.

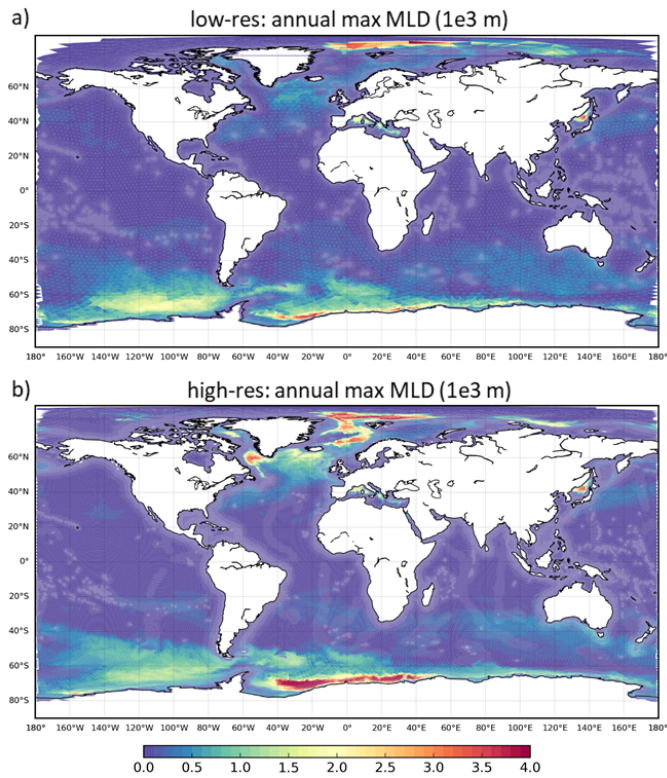


Figure 22: Annual maximum mixed layer depth simulated by the low-res (a) and high-res (b) configurations. Values in the northern and southern hemispheres represent March and September conditions, respectively.

950 more, in combination with a high horizontal resolution, the model might better represent
951 estuarine-like circulations and associated nutrient trapping in coastal regions of fresh water
952 influence (Algeo & Herrmann, 2018). Air-sea gas exchange could also be affected, as surface
953 fluxes are governed by saturation pressures in the surface layer. In the presented setup, the
954 limited vertical resolution may particularly affect the shallowest areas with a bathymetry
955 < 26 m, which are currently represented by only 2 grid layers. The total fraction of such
956 areas corresponds to about 6% of the global coastal ocean (water depth < 500 m) in both
957 configurations, low-res and high-res.

958 The additional processes generalized in ICON-Coast, compared to ICON-O and its
959 standard version of HAMOCC, are all crucially linked to the cycling of carbon and nutri-
960 ents in the coastal ocean (Fig. 1). Tidal waves induce mixing and sediment resuspension, the
961 aggregation of particulate matter affects vertical export fluxes, the temperature dependen-
962 cies of remineralization and dissolution rates modify the internal recycling, and river inputs
963 act as relevant sources of allochthonous organic and inorganic material. We evaluated these
964 add-ons with respect to the ability of the model to simulate key physical and biogeochemical
965 parameters influencing the surface CO_2 flux in the coastal ocean as well as the resulting CO_2
966 flux itself. The necessity to accurately reproduce tidal circulation, stratification, exchange
967 flows, and sediment diagenesis for embedding coastal interface biogeochemistry in global
968 ESMs was pointed out recently by Ward et al. (2020). Irrespective of remaining model
969 biases and a yet immature spinup history, the added value of ICON-Coast stands out in
970 the shown comparison of simulated coastal carbon dynamics with the Earth system model
971 MPI-ESM. Owing to its coarser resolution and the lack of the additional processes integrated
972 here, MPI-ESM is treating coastal areas essentially like a shallow version of an open ocean
973 basin, leading to an inherent misrepresentation of the land-ocean transition zone in the ma-
974 rine carbon cycle. Note that for these structural differences, the ocean-atmosphere coupling
975 included in MPI-ESM is of minor relevance. In fact, surface fluxes are often better balanced
976 in coupled simulations, inducing more realistic gradients and lower biases (e.g. Small et al.,
977 2011; Wang et al., 2015; Xue et al., 2020). The conceptual extension by ICON-Coast thus
978 links to the prospected reduction of uncertainties associated with global modeling exercises.
979 The increased degree of freedom that results from both the higher resolution and extended
980 process representation allows the coastal system to respond to external perturbations, while
981 at the same time feeding back to the adjacent open ocean. Continuous global warming,
982 for instance, would affect local stratification, carbon and nutrient recycling rates as well
983 as the composition and sinking speed of particulate matter. Changes in sea level or wind
984 surge would affect tidal currents and thus net carbon deposition in the coastal sediments.
985 In conventional global models, by contrast, projections for the carbon budget of the coastal
986 ocean are essentially determined by changes in the stratification and large-scale circulation
987 of the open ocean, as without the process extensions made here, import of open ocean water
988 masses represents defacto the only variable nutrient supply mechanism for coastal primary
989 production.

990 One of the main challenges in the model development of ICON-Coast is to bridge
991 the dynamic scales from the deep and open ocean to the shallow shelves and marginal
992 seas by applying globally implemented parameterizations to both eddying and non-eddying
993 regions. ICON-Coast uses a biharmonic horizontal dissipation scheme that is dependent
994 on the mesh spacing and thus, in combination with the regional refinement, accounts for
995 the transition of pertinent scales. The implemented TKE vertical mixing scheme is also
996 scale-dependent but could be further improved to better represent mixing at the bottom
997 boundary layer as suggested e.g. by Holt et al. (2017). In our simulations, we have inten-
998 tionally deactivated the eddy parameterization (Korn, 2018) because first, the combination
999 of eddy closure with the coastal grid refinement considered here is an unsolved problem in
1000 computational fluid dynamics, and second, it allows us to better assess the impact of the
1001 grid refinement. Yet, we are optimistic that a suitably chosen eddy parameterization will
1002 lead to additional improvements of our results, in particular for the general circulation and
1003 tracer distribution in the open ocean. The incorporation of subgridscale eddy activity was

Table 3: Resource demands for simulations with ICON-O and ICON-Coast, when run on the high-res grid with variable resolution of 80-10 km as well as on a globally uniform 10 km grid. The ICON-O run on the high-res grid differs from the ICON-Coast run only with respect to the additional processes implemented to ICON-Coast (see section 2.2). All simulations are performed using 200 nodes of the HPC system 'Mistral'. Each node of the used partition consists of 2x 18-core Intel Xeon E5-2695 v4 (Broadwell) processors with a speed of 2.1 GHz. To quantify the net computing load, we give turnover rates and computational costs also for simulations excluding model output. For runs on the variable-resolution grid, this setup corresponds to an efficiency of about 0.75 and 0.85 with and without output writing, respectively, compared to linear scaling.

Metric	ICON-O uni. 10 km	ICON-O var. 80-10 km	ICON-Coast var. 80-10 km
Wet surface cells	3,730,000	860,000	860,000
Turnover (no outp.)	1.16 yr d ⁻¹	3.70 yr d ⁻¹	2.78 yr d ⁻¹
Turnover (w. outp.)	0.97 yr d ⁻¹	2.50 yr d ⁻¹	2.00 yr d ⁻¹
Cost (no outp.)	413 knh 100yr ⁻¹	128 knh 100yr ⁻¹	172 knh 100yr ⁻¹
Cost (w. outp.)	492 knh 100yr ⁻¹	192 knh 100yr ⁻¹	240 knh 100yr ⁻¹
Storage	45.9 TB 100yr ⁻¹	9.0 TB 100yr ⁻¹	11.1 TB 100yr ⁻¹

1004 shown to impact temperature, salinity and sea ice formation in high latitudes (e.g. Knutti
1005 et al., 1999; Pradal & Gnanadesikan, 2014) as well as nutrient replenishment in the upper
1006 thermocline of oligotrophic subtropical waters (Oschlies, 2008; Doddridge & Marshall, 2018)
1007 and seasonal carbon drawdown in the eddy-rich Southern Ocean (Jersild et al., 2021). The
1008 sediment resuspension scheme of ICON-Coast accounts for the bottom layer thickness in the
1009 calculation of the sediment drag coefficient, thus accounting for the vertical grid resolution
1010 (Mathis et al., 2019). Also here, an improvement would be to include dependence on the
1011 horizontal grid scale as well.

1012 Apart from a better representation of coastal carbon dynamics, higher resource de-
1013 mands of ICON-Coast compared to conventional global models with coarser resolution are
1014 justified by the benefit of having included all coastal areas of the world within a single con-
1015 sistent simulation, thus naturally accounting for two-way coupling of ocean-shelf feedback
1016 mechanisms at the global scale. Computational costs as well as data storage requirements
1017 of high-resolution simulations, though, can be substantially reduced by limiting the grid
1018 refinement to dedicated areas only. In Table 3, we contrast resource demands for simula-
1019 tions with ICON-O and ICON-Coast, run on the high-res grid presented here (80-10 km) as
1020 well as on a globally uniform 10 km-resolution grid. Because of the regionally applied grid
1021 refinement, the variable-resolution grid of ICON-Coast has less surface grid cells than the
1022 uniform-resolution grid by a factor of about 4.3. We conducted reference experiments at
1023 the current HPC system Mistral of the DKRZ, using 200 parallelized cpu nodes (see caption
1024 of Table 3 for specifications). The lower number of grid cells of the variable-resolution grid
1025 leads to a significant saving in computational cost, reducing the required real time for a
1026 simulation of 100 years with ICON-O from about 3 months to less than 1 month. The
1027 computational demands of ICON-Coast, however, increase by 25% due to the additionally
1028 implemented processes (section 2.2). About 30% of cost and time are associated with output
1029 writing, resulting in a total demand of 50 days for a 100-year simulation with ICON-Coast,
1030 including monthly 2d and 3d gridded physical and biogeochemical standard output. Sim-
1031 ilarly, the regional grid refinement reduces the storage space required for the output by a
1032 factor of about 4. These specifications of ICON-Coast allow for reasonable experimental
1033 setups e.g. to study the anthropogenic perturbation of the marine carbon cycle, comprising
1034 a 50-yr spinup run and two 100-yr production runs. Longer spinup simulations spanning
1035 a few hundred years could be performed with the low-res grid configuration at comparable
1036 total cost.

1037 5 Conclusions

1038 In this paper, we have introduced ICON-Coast, the first global ocean-biogeochemistry
 1039 model that uses a telescoping high resolution for an improved representation of coastal car-
 1040 bon dynamics. This approach enables for the first time a seamless incorporation of the
 1041 global coastal ocean in model-based Earth system research. The broad agreement of simu-
 1042 lated shelf-specific physical and biogeochemical processes with both observational products
 1043 and high-resolution regional modeling studies demonstrates the large potential of ICON-
 1044 Coast to be used for cross-cutting scientific applications. Linkages between carbon and
 1045 nutrient transformation pathways in the open ocean, the transition zone to the continental
 1046 shelves, and the near-coastal areas can be investigated that cannot be derived from isolated
 1047 regional modeling studies. Examples are the importance of carbon sequestration, storage,
 1048 and transport processes on the shallow shelves relative to the open ocean under different
 1049 climatic conditions (G. G. Laruelle et al., 2018), or the fate of river inputs and their con-
 1050 nection to interhemispheric carbon transport (Aumont et al., 2001; Resplandy et al., 2018).
 1051 Sensitivity experiments can be used to explore the susceptibility of the coastal ocean en-
 1052 vironment to external perturbations across a range of spatiotemporal scales and interfaces
 1053 (Ward et al., 2020).

1054 The high quality of the model results shown here as well as the efficiency in compu-
 1055 tational cost and storage requirements verifies the strategy of a seamless connection of the
 1056 open and coastal ocean via regional grid refinement and enhanced process representation as
 1057 a pioneering approach for high-resolution modeling at the global scale. In view of the difficul-
 1058 ties in reconciling prognostically shelf-specific processes in the sediment, water column, and
 1059 at the air-sea interface, the model ICON-Coast, built on extended basic parameterizations
 1060 of a global ocean-biogeochemistry model, is encouraging.

1061 Already with the low-res version, spanning a horizontal resolution of 160-20 km, we
 1062 achieve unprecedented accuracy and level of detail in simulating governing processes of the
 1063 coastal carbon dynamics in low, middle and high latitudes, even on the seasonal time scale.
 1064 Some features, such as the general circulation or net primary production, are comparable to
 1065 results from state-of-the-art high-resolution regional model systems, and the incorporation
 1066 of marine aggregates even exceeds the process representation of many established regional
 1067 ecosystem models. We thus conclude that ICON-Coast represents a new tool to deepen our
 1068 mechanistic understanding about the role of the land-ocean transition zone in the global
 1069 carbon cycle, and to narrow related uncertainties in global future projections.

1070 The development of this first version of ICON-Coast was guided by the consideration
 1071 of coastal carbon dynamics. It is clear, however, that the scientific applications of such a
 1072 model system are not restricted to topics related to the carbon cycle. The concept of ICON-
 1073 Coast generally enables high-resolution modeling in the global coastal ocean, including the
 1074 continental margin as the transition to the open ocean. Potential applications thus range
 1075 from investigations of marine extreme events in coastal areas (e.g. storm surges, heat waves,
 1076 hypoxia), and ocean-shelf exchange processes including feedback mechanisms, to scenario-
 1077 based future projections of the coastal ocean physical and biogeochemical state, and sen-
 1078 sitivity studies regarding the efficiency of various coastal management and eutrophication
 1079 policies.

1080 Acknowledgments

1081 This work contributed to the subproject *A5 - The Land-Ocean Transition Zone* of Ger-
 1082 many's Excellence Strategy EXC 2037 *CLICCS - Climate, Climatic Change, and Society*
 1083 with project No 390683824, funded by the Deutsche Forschungsgemeinschaft (DFG, Ger-
 1084 man Research Foundation). Computational resources were made available by the German
 1085 Climate Computing Center (DKRZ) through support from the German Federal Ministry
 1086 of Education and Research (BMBF). TI was supported by the European Union's *Horizon*
 1087 *2020* research and innovation program under grant agreement No 101003536 (*ESM2025 -*

1088 *Earth System Models for the Future*). The source code of ICON-Coast can be accessed via
1089 the gitlab repository hosted at DKRZ: [https://gitlab.dkrz.de/icon/icon-oes/-/tree/icon-oes-](https://gitlab.dkrz.de/icon/icon-oes/-/tree/icon-oes-mm-coast_relaunch)
1090 [mm-coast_relaunch](https://gitlab.dkrz.de/icon/icon-oes/-/tree/icon-oes-mm-coast_relaunch). We thank the associate editor Andreas Oschlies and two anonymous
1091 reviewers whose comments helped improve and clarify this article.

Appendix A Supplementary figures

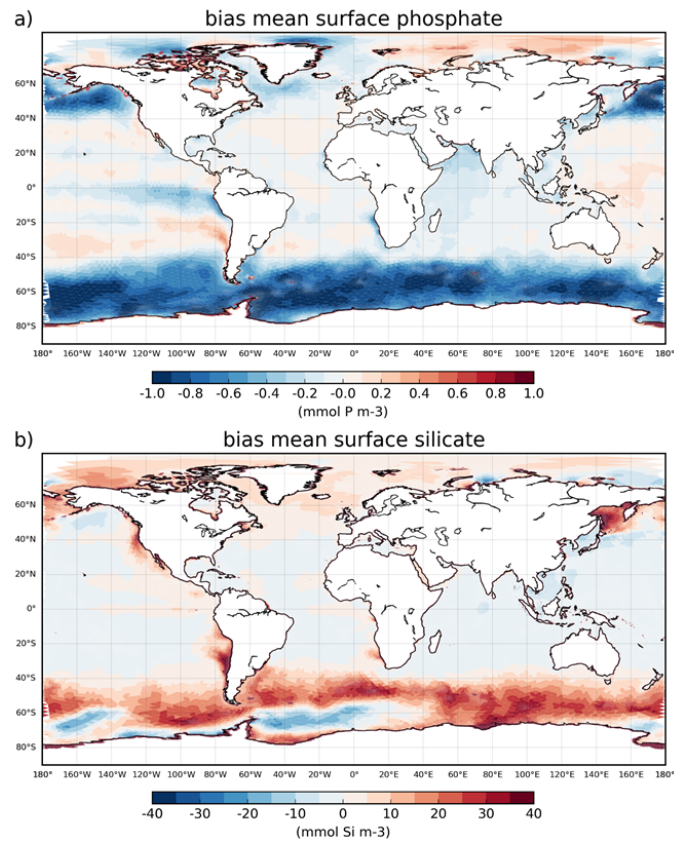


Figure A1: Global distribution of biases in annual surface phosphate (a) and silicate (b) concentrations, simulated with ICON-Coast low-res configuration. Biases are relative to World Ocean Atlas 2018 Boyer et al. (2018).

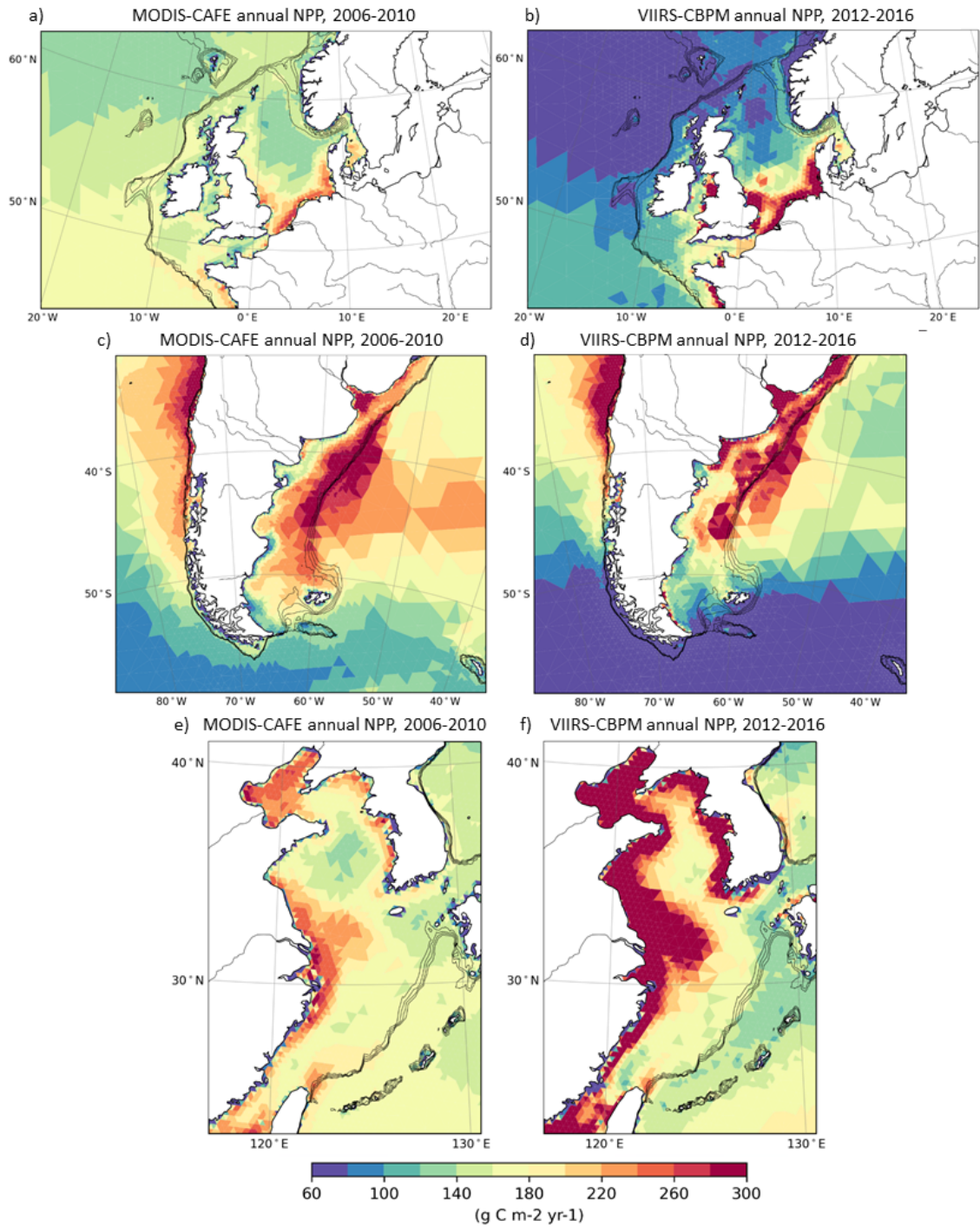


Figure A2: Annual satellite-derived net primary production on the Northwest European Shelf (a,b), Patagonian Shelf (c,d) and East China Shelf (e,f). MODIS-CAFE (Silsbe et al., 2016) product for the period 2006-2010 is shown in (a,c,e), VIIRS-CBPM (Westberry et al., 2008) product for 2012-2016 is shown in (b,d,f), as provided by the Ocean Productivity service (<http://sites.science.oregonstate.edu/ocean.productivity/index.php>). Data have been interpolated onto the low-res grid of ICON-Coast. Isobaths illustrate the shelf break at water depths of 200-500 m.

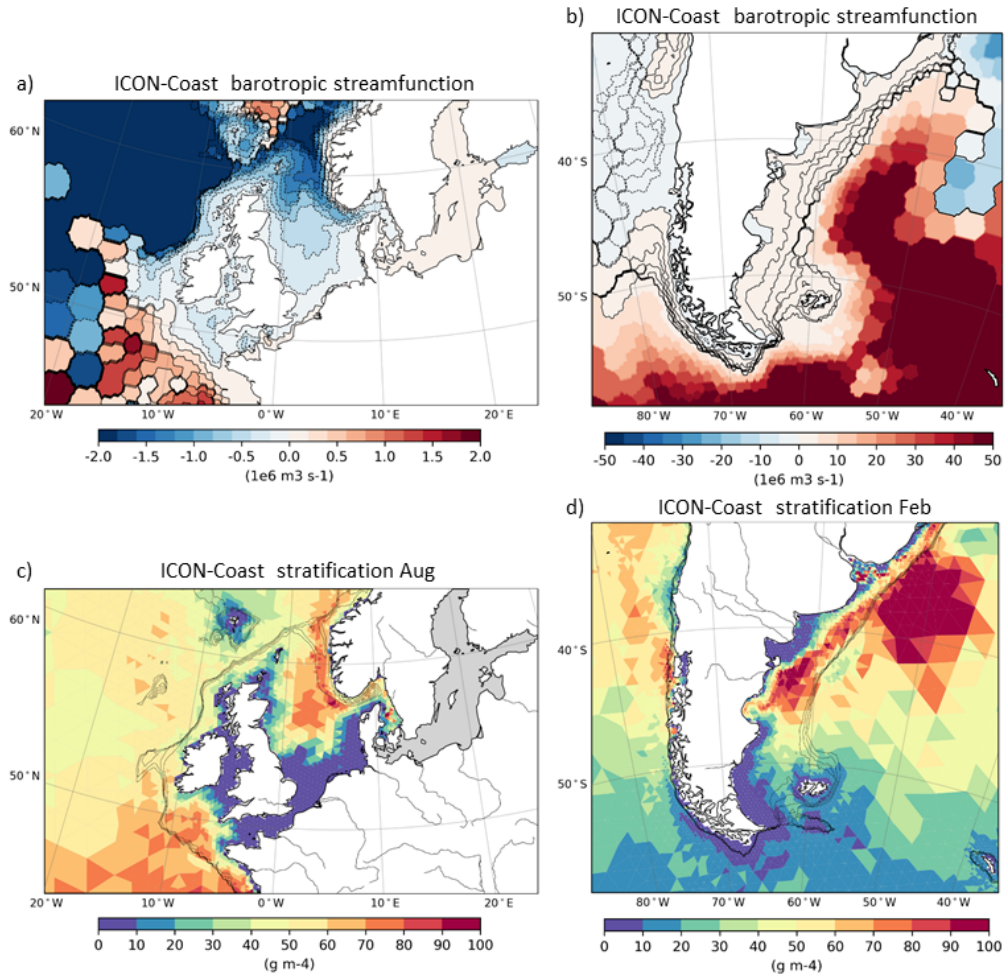


Figure A3: Shelf circulation and seasonal stratification simulated with ICON-Coast low-res configuration: Annual mean barotropic stream function on the Northwest European Shelf (a) and Patagonian Shelf (b). Increments of streamlines are 0.2 Sv for (a) and 0.5 Sv for (b). Hexagonal structures emerge from the calculation and mapping of net volume fluxes through the triangular grid cells. Strength of summer stratification (maximum vertical density gradient) on the Northwest European Shelf (c) and Patagonian Shelf (d). Isobaths illustrate the shelf break at water depths of 200-500 m.

1093

References

- 1094 Aarnos, H., G elinas, Y., Kasurinen, V., Gu, Y., Puupponen, V. M., & V ah atalo, A. V.
1095 (2018). Photochemical Mineralization of Terrigenous DOC to Dissolved Inorganic Carbon
1096 in Ocean. *Global Biogeochemical Cycles*, *32*, 250-266. doi: 10.1002/2017GB005698
- 1097 Acha, E. A., Mianzan, H. W., Guerrero, R. A., Favero, M., & Bava, J. (2004). Marine fronts
1098 at the continental shelves of austral South America: Physical and ecological processes.
1099 *Journal of Marine Systems*, *44*, 83-105. doi: 10.1016/j.jmarsys.2003.09.005
- 1100 Acha, M., Mianzan, H., Guerrero, R., Carreto, J., Giberto, D., Montoya, N., & Carignan, M.
1101 (2008). An overview of physical and ecological processes in the Rio de la Plata Estuary.
1102 *Continental Shelf Research*, *28*, 1579-1588. doi: 10.1016/j.csr.2007.01.031
- 1103 Algeo, T., & Herrmann, A. (2018). An ancient estuarine-circulation nutrient trap: The
1104 Late Pennsylvanian Midcontinent Sea of North America. *Geology*, *46*, 143-146. doi:
1105 10.1130/G39804.1
- 1106 Allen, J. I., Aiken, J., Anderson, T. R., Buitenhuis, E., Cornell, S., Geider, R. J., . . . While,
1107 J. (2010). Marine ecosystem models for earth systems applications: The MarQUEST
1108 experience. *Journal of Marine Systems*, *81*, 19-33. doi: 10.1016/j.jmarsys.2009.12.017
- 1109 Amiotte Suchet, P., & Probst, J. L. (1995). A global model for present-day atmospheric/soil
1110 CO₂ consumption by chemical erosion of continental rocks (GEM-CO₂). *Tellus B: Chem-*
1111 *ical and Physical Meteorology*, *47*, 273-280. doi: 10.3402/tellusb.v47i1-2.16047
- 1112 Araujo, M., Noriega, C., & Lef evre, N. (2014). Nutrients and carbon fluxes in the estuaries
1113 of major rivers flowing into the tropical Atlantic. *Front. Mar. Sci.*, *1*, 1-16. doi: 10.3389/
1114 fmars.2014.00010
- 1115 Arndt, S., J orgensen, B. B., Rowe, D. E. L., Middelburg, J. J., Pancost, R. D., & Regnier,
1116 P. (2013). Quantifying the degradation of organic matter in marine sediments: A review
1117 and synthesis. *Earth-Science Reviews*, *123*, 53-86. doi: 10.1016/j.earscirev.2013.02.008
- 1118 Arrigo, K., van Dijken, G., & Long, M. (2008). Coastal Southern Ocean: A strong anthro-
1119 pogenic CO₂ sink. *Geophys. Res. Lett.*, *35*, 6 pp. doi: 10.1029/2008GL035624
- 1120 Arrigo, K. R., & van Dijken, G. L. (2015). Continued increases in Arctic Ocean primary
1121 production. *Progr. Oceanogr.*, *136*, 60-70. doi: 10.1016/j.pocean.2015.05.002
- 1122 Aumont, O., Orr, J. C., Monfray, P., Ludwig, W., Suchet, P. A., & Probst, J. L. (2001).
1123 Riverine-driven interhemispheric transport of carbon. *Global Biogeochem. Cy.*, *15*, 393-
1124 405. doi: 10.1029/1999GB001238
- 1125 Babin, M., & Stramski, D. (2004). Variations in the mass-specific absorption coefficient of
1126 mineral particles suspended in water. *Limnology and Oceanography*, *49*, 756-767. doi:
1127 10.4319/lo.2004.49.3.0756
- 1128 Bai, Y., He, X., Pan, D., Chen, C. T. A., Kang, Y., Chen, X., & Cai, W. J. (2014). Sum-
1129 mertime Changjiang River plume variation during 1998-2010. *Journal of Geophysical*
1130 *Research: Oceans*, *119*, 6238-6257. doi: 10.1002/2014JC009866
- 1131 Bates, N. R. (2006). Air-sea CO₂ fluxes and the continental shelf pump of carbon in
1132 the Chukchi Sea adjacent to the Arctic Ocean. *J. Geophys. Res.*, *111*, 21 pp. doi:
1133 10.1029/2005JC003083
- 1134 Bates, N. R., & Mathis, J. T. (2009). The Arctic Ocean marine carbon cycle: evaluation
1135 of air-sea CO₂ exchanges, ocean acidification impacts and potential feedbacks. *Biogeo-*
1136 *sciences*, *6*, 2433-2459. doi: 10.5194/bg-6-2433-2009
- 1137 Bauer, J. E., Cai, W. J., Raymond, P. A., Bianchi, T. S., Hopkinson, C. S., & Regnier,
1138 P. A. G. (2013). The changing carbon cycle of the coastal ocean. *Nature*, *504*, 61-70.
1139 doi: 10.1038/nature12857
- 1140 Becker, M., Olsen, A., Landsch utzer, P., Omar, A., Rehder, G., R odenbeck, C., & Skjelvan,
1141 I. (2021). The northern European shelf as an increasing net sink for CO₂. *Biogeo-*
1142 *sciences*, *18*, 1127-1147. doi: 10.5194/bg-18-1127-2021
- 1143 Behrens, J., & Bader, M. (2009). Efficiency considerations in triangular adaptive mesh
1144 refinement. *Phil. Trans. R. Soc. A.*, *367*, 4577-4589. doi: 10.1098/rsta.2009.0175
- 1145 Berner, R. A., Lasaga, A. C., & Garrels, R. M. (1983). The carbonate-silicate geochem-

- 1146 ical cycle and its effect on atmospheric carbon dioxide over the past 100 million years.
 1147 *American Journal of Science*, *283*, 641-683. doi: 10.2475/ajs.283.7.641
- 1148 Beusen, A. H. W., Bouwman, A. F., Dürr, H., Dekkers, A. L. M., & Hartmann, J. (2009).
 1149 Global patterns of dissolved silica export to the coastal zone: Results from a spatially
 1150 explicit global model. *Global Biogeochem. Cy.*, *23*, GB0A02. doi: 10.1029/2008GB003281
- 1151 Beusen, A. H. W., Bouwman, A. F., Van Beek, L. P. H., Mogollón, J. M., & Middelburg,
 1152 J. J. (2016). Global riverine N and P transport to ocean increased during the 20th century
 1153 despite increased retention along the aquatic continuum. *Biogeosciences*, *13*, 2441-2451.
 1154 doi: 10.5194/bg-13-2441-2016
- 1155 Bianchi, A. A., Bianucci, L., Piola, A. R., Pino, D. R., Schloss, I., Poisson, A., & Balestrini,
 1156 C. F. (2005). Vertical stratification and air-sea CO₂ fluxes in the Patagonian shelf.
 1157 *Journal of Geophysical Research: Oceans*, *110*, 11 pp. doi: 10.1029/2004JC002488
- 1158 Birol, F., Fuller, N., Lyard, F., Cancet, M., Niño, F., Delebecque, C., ... Léger, F. (2017).
 1159 Coastal applications from nadir altimetry: Example of the X-TRACK regional products.
 1160 *Advances in Space Research*, *59*, 936-953. doi: 10.1016/j.asr.2016.11.005
- 1161 Borges, D. B., A. V., & Frankignoulle, M. (2005). Budgeting sinks and sources of CO₂ in
 1162 the coastal ocean: Diversity of ecosystems counts. *Geophys. Res. Lett.*, *32*, L14601. doi:
 1163 10.1029/2005GL023053
- 1164 Bourgeois, T., Orr, J. C., Resplandy, L., Terhaar, J., Ethé, C., Gehlen, M., & Bopp, L.
 1165 (2016). Coastal-ocean uptake of anthropogenic carbon. *Biogeosciences*, *13*, 4167-4185.
 1166 doi: 10.5194/bg-13-4167-2016
- 1167 Boyd, P. W., Sundby, S., & Pörtner, H. O. (2014). Cross-chapter box on net primary produc-
 1168 tion in the ocean. In C. B. Field et al. (Eds.), *Climate change 2014: Impacts, adaptation,*
 1169 *and vulnerability. part a: Global and sectoral aspects. contribution of working group ii to*
 1170 *the fifth assessment report of the intergovernmental panel on climate change* (p. 133-136).
 1171 Cambridge, United Kingdom and New York, NY, USA: Cambridge University Press.
- 1172 Boyer, T. P., García, H. E., Locarnini, R. A., Zweng, M. M., Mishonov, A. V., Reagan, J. R.,
 1173 ... Smolyar, I. V. (2018). World Ocean Atlas 2018 (2005-2017). *NOAA National Centers*
 1174 *for Environmental Information*, [https://www.ncei.noaa.gov/archive/accession/NCEI-](https://www.ncei.noaa.gov/archive/accession/NCEI-WOA18)
 1175 [WOA18](https://www.ncei.noaa.gov/archive/accession/NCEI-WOA18).
- 1176 Brink, K. H. (2016). Cross-Shelf Exchange. *Annual Review of Marine Science*, *8*, 59-78.
 1177 doi: 10.1146/annurev-marine-010814-015717
- 1178 Buitenhuis, E. T., Hashioka, T., & Quéré, C. L. (2013). Combined constraints on global
 1179 ocean primary production using observations and models. *Global Biogeochemical Cycles*,
 1180 *27*, 847-858. doi: 10.1002/gbc.20074
- 1181 Burdige, D. J. (2007). Preservation of Organic Matter in Marine Sediments: Controls,
 1182 Mechanisms, and an Imbalance in Sediment Organic Carbon Budgets? *Chem. Rev.*, *107*,
 1183 467-485. doi: 10.1021/cr050347q
- 1184 Bushinsky, S. M., Landschützer, P., Rödenbeck, C., Gray, A. R., Baker, D., Mazloff, M. R.,
 1185 ... Sarmiento, J. L. (2019). Reassessing Southern Ocean Air-Sea CO₂ Flux Estimates
 1186 With the Addition of Biogeochemical Float Observations. *Global Biogeochemical Cycles*,
 1187 *33*, 1370-1388. doi: 10.1029/2019GB006176
- 1188 Cadier, M., Gorgues, T., L'Helguen, S., Sourisseau, M., & Memery, L. (2017). Tidal cycle
 1189 control of biogeochemical and ecological properties of a macrotidal ecosystem. *Geophys.*
 1190 *Res. Lett.*, *44*, 8453-8462. doi: 10.1002/2017GL074173
- 1191 Cai, W. J. (2011). Estuarine and coastal ocean carbon paradox: CO₂ sinks or sites of
 1192 terrestrial carbon incineration? *Ann. Rev. Mar. Sci.*, *3*, 123-145. doi: 10.1146/annurev-
 1193 -marine-120709-142723
- 1194 Cai, W. J., Chen, L., Chen, B., Gao, Z., Lee, S. H., Chen, J., ... Zhang, H. (2010). Decrease
 1195 in the CO₂ Uptake Capacity in an Ice-Free Arctic Ocean Basin. *Science*, *329*, 556-559.
 1196 doi: 10.1126/science.1189338
- 1197 Campbell, J., Antoine, D., Armstrong, R., Arrigo, K., Balch, W., Barber, R., ... Yoder, J.
 1198 (2002). Comparison of algorithms for estimating ocean primary production from surface
 1199 chlorophyll, temperature, and irradiance. *Global Biogeochemical Cycles*, *16*, 15 pp. doi:

- 1200 10.1029/2001GB001444
- 1201 Canadell, J. G., Ciiais, P., Dhakal, S., Dolman, H., Friedlingstein, P., Gurney, K. R., ...
- 1202 Raupach, M. R. (2010). Interactions of the carbon cycle, human activity, and the climate
- 1203 system: a research portfolio. *Current Opinion in Environmental Sustainability*, *2*, 301-
- 1204 311. doi: 10.1016/j.cosust.2010.08.003
- 1205 Cao, Z., Yang, W., Zhao, Y., Guo, X., Yin, Z., Du, C., ... Dai, M. (2020). Diagnosis of
- 1206 CO₂ dynamics and fluxes in global coastal oceans. *National Science Review*, *7*, 786-797.
- 1207 doi: 10.1093/nsr/nwz105
- 1208 Capuzzo, E., Lynam, C. P., Barry, J., Stephens, D., Forster, R. M., Greenwood, N., ...
- 1209 Engelhard, G. H. (2018). A decline in primary production in the North Sea over 25 years,
- 1210 associated with reductions in zooplankton abundance and fish stock recruitment. *Global*
- 1211 *Change Biology*, *24*, 352-364.
- 1212 Carless, S. J., Green, J. A. M., Pelling, H. E., & Wilmes, S. B. (2016). Effects of future
- 1213 sea-level rise on tidal processes on the Patagonian Shelf. *Journal of Marine Systems*, *163*,
- 1214 113-124. doi: 10.1016/j.jmarsys.2016.07.007
- 1215 Carr, M. E., Friedrichs, M. A. M., Schmeltz, M., Noguchi-Aita, M., Antoine, D., Arrigo,
- 1216 K. R., ... Yamanaka, Y. (2006). A comparison of global estimates of marine primary
- 1217 production from ocean color. *Deep Sea Research Part II: Topical Studies in Oceanography*,
- 1218 *53*, 741-770. doi: 10.1016/j.dsr2.2006.01.028
- 1219 Carreto, J. I., Montoya, N. G., Carignan, M. O., Akselman, R., Acha, E. M., & Derisio,
- 1220 C. (2016). Environmental and biological factors controlling the spring phytoplankton
- 1221 bloom at the Patagonian shelf-break front - Degraded fucoxanthin pigments and the
- 1222 importance of microzooplankton grazing. *Progress in Oceanography*, *146*, 1-21. doi:
- 1223 10.1016/j.pocean.2016.05.002
- 1224 Chen, C., Liu, H., & Beardsley, R. C. (2003). An unstructured grid, finite-volume, three-
- 1225 dimensional, primitive equations ocean model: Application to coastal ocean and estu-
- 1226 aries. *Journal of Atmospheric and Oceanic Technology*, *20*, 159-186. doi: 10.1175/
1227 1520-0426(2003)020<0159:AUGFVT>2.0.CO;2
- 1228 Chen, H. W., Liu, C. T., Matsuno, T., Ichikawa, K., Fukudome, K., Yang, Y., ... Tsai, W. L.
- 1229 (2016). Temporal variations of volume transport through the Taiwan Strait, as identified
- 1230 by three-year measurements. *Cont. Shelf Res.*, *114*, 41-53. doi: 10.1016/j.csr.2015.12.010
- 1231 Cheng, Y., Putrasahan, D., Beal, L., & Kirtman, B. (2016). Quantifying Agulhas Leakage
- 1232 in a High-Resolution Climate Model. *Journal of Climate*, *29*, 6881-6892. doi: 10.1175/
1233 JCLI-D-15-0568.1
- 1234 Clark, M., Marsh, R., & Harle, J. (2021). Weakening and warming of the European Slope
- 1235 Current since the late 1990s attributed to basin-scale density changes. *Ocean Science*
- 1236 *Discussions*, 32 pp. doi: 10.5194/os-2021-60
- 1237 Combes, V., & Matano, R. P. (2018). The Patagonian shelf circulation: Drivers and
- 1238 variability. *Progress in Oceanography*, *167*, 24-43.
- 1239 Combes, V., Matano, R. P., & Palma, E. D. (2021). Circulation and cross-shelf exchanges in
- 1240 the northern shelf region of the southwestern Atlantic: Kinematics. *Journal of Geophysical*
- 1241 *Research: Oceans*, *126*, 16 pp. doi: 10.1029/2020JC016959
- 1242 Compton, J., Mallinson, D., Glenn, C. R., Filippelli, G., Follmi, K., Shields, G., & Zanin, Y.
- 1243 (2000). Variations in the Global Phosphorus cycle. In *Marine authigenesis: From global*
- 1244 *to microbial*. SEPM Society for Sedimentary Geology. doi: 10.2110/pec.00.66.0021
- 1245 Dai, M., Cao, Z., Guo, X., Zhai, W., Liu, Z., Yin, Z., ... Du, C. (2013). Why are some
- 1246 marginal seas sources of atmospheric CO₂? *Geophysical Research Letters*, *40*, 2154-2158.
- 1247 doi: doi.org/10.1002/grl.50390
- 1248 Dale, A. C., & Inall, M. E. (2015). Tidal mixing processes amid small-scale, deep-ocean
- 1249 topography. *Geophysical Research Letters*, *42*, 484-491. doi: 10.1002/2014GL062755
- 1250 Danilov, S. (2010). On utility of triangular C-grid type discretization for numerical modeling
- 1251 of large-scale ocean flows. *Ocean Dynamics*, *60*, 1361-1369. doi: 10.1007/s10236-010-0339
- 1252 -6
- 1253 Danilov, S., Wang, Q., Timmermann, R., Iakovlev, N., Sidorenko, D., Kimmritz, M., ...

- 1254 Schröter, J. (2015). Finite-element sea ice model (FESIM), version 2. *Geosci. Model.*
 1255 *Dev.*, *8*, 1747-1761. doi: 10.5194/gmd-8-1747-2015
- 1256 Dee, D. P., Uppala, S. M., Simmons, A. J., Berrisford, P., Poli, P., Kobayashi, S., ...
 1257 Vitart, F. (2011). The ERA-Interim reanalysis: configuration and performance of the
 1258 data assimilation system. *Quarterly Journal of the Royal Meteorological Society*, *137*,
 1259 553-597. doi: 10.1002/qj.828
- 1260 de Souza, M. M., Mathis, M., Mayer, B., Noernberg, M. A., & Pohlmann, T. (2020).
 1261 Possible impacts of anthropogenic climate change to the upwelling in the South Brazil
 1262 Bight. *Climate Dynamics*, *55*, 651-664. doi: 10.1007/s00382-020-05289-0
- 1263 DeVries, T., & Weber, T. (2017). The export and fate of organic matter in the ocean:
 1264 New constraints from combining satellite and oceanographic tracer observations. *Global*
 1265 *Biogeochemical Cycles*, *31*, 535-555. doi: 10.1002/2016GB005551
- 1266 Diesing, M., Kröger, S., Parker, R., Jenkins, C., Mason, C., & Weston, K. (2017). Predicting
 1267 the standing stock of organic carbon in surface sediments of the North-West European
 1268 continental shelf. *Biogeochemistry*, *135*, 183-200. doi: 10.1007/s10533-017-0310-4
- 1269 Diesing, M., Thorsnes, T., & Bjarnadóttir, L. R. (2021). Organic carbon densities and
 1270 accumulation rates in surface sediments of the North Sea and Skagerrak. *Biogeosciences*,
 1271 *18*, 2139-2160. doi: 10.5194/bg-18-2139-2021
- 1272 Dixit, S., van Cappellen, P., & van Bennekom, A. J. (2001). Processes controlling solubility
 1273 of biogenic silica and pore water build-up of silicic acid in marine sediments. *Marine*
 1274 *Chemistry*, *73*, 333-352. doi: 10.1016/S0304-4203(00)00118-3
- 1275 Doddridge, E. W., & Marshall, D. P. (2018). Implications of Eddy Cancellation for Nutrient
 1276 Distribution Within Subtropical Gyres. *Journal of Geophysical Research: Oceans*, *123*,
 1277 6720-6735. doi: 10.1029/2018JC013842
- 1278 Duarte, C. M., Middelburg, J. J., & Caraco, N. (2005). Major role of marine vegetation on
 1279 the oceanic carbon cycle. *Biogeosciences*, *2*, 1-8. doi: 10.5194/bg-2-1-2005
- 1280 Dürr, H. H., Meybeck, M., Hartmann, J., Laruelle, G. G., & Roubeix, V. (2011). Global
 1281 spatial distribution of natural riverine silica inputs to the coastal zone. *Biogeosciences*,
 1282 *8*, 597-620. doi: 10.5194/bg-8-597-2011
- 1283 Egbert, G. D., & Erofeeva, S. Y. (2002). Efficient inverse modeling of barotropic ocean
 1284 tides. *J. Atmos. Ocean. Technol.*, *19*, 183-204. doi: 10.1175/1520-0426(2002)019<0183:
 1285 EIMOBO>2.0.CO;2
- 1286 Ekici, A., Beer, C., Hagemann, S., Boike, J., Langer, M., & Hauck, C. (2014). Simulating
 1287 high-latitude permafrost regions by the JSBACH terrestrial ecosystem model. *Geoscientific*
 1288 *Model Development*, *7*, 631-647. doi: 10.5194/gmd-7-631-2014
- 1289 Eyring, V., Bony, S., Meehl, G. A., Senior, C. A., Stevens, B., Stouffer, R. J., & Taylor,
 1290 K. E. (2016). Overview of the coupled model intercomparison project phase 6 (CMIP6)
 1291 experimental design and organization. *Geoscient. Model. Dev.*, *9*, 1937-1958. doi: 10
 1292 .5194/gmd-9-1937-2016
- 1293 Fennel, K., Alin, S., Barbero, L., Evans, W., Bourgeois, T., Cooley, S., ... Wang, Z. A.
 1294 (2019). Carbon cycling in the North American coastal ocean: a synthesis. *Biogeosciences*,
 1295 *16*, 1281-1304. doi: 10.5194/bg-16-1281-2019
- 1296 Fettweis, M., Baeye, M., Van der Zande, D., Van den Eynde, D., & Lee, B. J. (2014).
 1297 Seasonality of flocculation strength in the southern North Sea. *Journal of Geophysical Research:*
 1298 *Oceans*, *119*, 1911-1926. doi: 10.1002/2013JC009750
- 1299 Fichot, C. G., & Benner, R. (2014). The fate of terrigenous dissolved organic carbon in a
 1300 riverinfluenced ocean margin. *Global Biogeochemical Cycles*, *28*, 300-318. doi: 10.1002/
 1301 2013GB004670
- 1302 Franco, B. C., Palma, E. D., Combes, V., & Lasta, M. L. (2017). Physical processes
 1303 controlling passive larval transport at the Patagonian Shelf Break Front. *Journal of Sea*
 1304 *Research*, *124*, 17-25. doi: 10.1016/j.seares.2017.04.012
- 1305 Francois, R., Honjo, S., Krishfield, R., & Manganini, S. (2002). Factors controlling the flux
 1306 of organic carbon to the bathypelagic zone of the ocean. *Global Biogeochemical Cycles*,
 1307 *16*, 20 pp. doi: 10.1029/2001GB001722

- 1308 Franzo, A., Celussi, M., Bazzaro, M., Relitti, F., & Negro, P. D. (2019). Microbial processing
1309 of sedimentary organic matter at a shallow LTER site in the northern Adriatic Sea: an
1310 8-year case study. *Nature Conservation*, *34*, 397-415. doi: 10.3897/natureconservation
1311 .34.30099
- 1312 Frey, D., Piola, A., Krechik, V., Fofanov, D. V., Morozov, E. G., Silvestrova, K., ... Gladyshev,
1313 S. V. (2021). Direct Measurements of the Malvinas Current Velocity Structure.
1314 *Journal of Geophysical Research: Oceans*, *126*. doi: 10.1029/2020JC016727
- 1315 Friedlingstein, P., O'Sullivan, M., Jones, M. W., Andrew, R. M., Hauck, J., Olsen, A.,
1316 ... Zaehle, S. (2020). Global Carbon Budget 2020. *Earth System Science Data*, *12*,
1317 3269-3340. doi: 10.5194/essd-12-3269-2020
- 1318 Galy, V., Peucker-Ehrenbrink, B., & Eglinton, T. (2015). Global carbon export from
1319 the terrestrial biosphere controlled by erosion. *Nature*, *521*, 204-207. doi: 10.1038/
1320 nature14400
- 1321 Gaspar, P., Grégoris, Y., & Lefevre, J. M. (1990). A simple eddy kinetic energy model for
1322 simulations of the oceanic vertical mixing: Tests at station Papa and long-term upper
1323 ocean study site. *Journal of Geophysical Research: Oceans*, *95*, 16179-16193. doi: 10
1324 .1029/JC095iC09p16179
- 1325 Gattuso, J. P., Frankignoulle, M., & Wollast, R. (1998). Carbon and carbonate metabolism
1326 in coastal aquatic ecosystems. *Annual Review of Ecology and Systematics*, *29*, 405-434.
1327 doi: 10.1146/annurev.ecolsys.29.1.405
- 1328 Gille, S. T., Metzger, E. J., & Tokmakian, R. (2004). Seafloor topography and ocean
1329 circulation. *Oceanography*, *17*, 47-54. doi: 10.5670/oceanog.2004.66
- 1330 Gloege, L., McKinley, G. A., Mouw, C. B., & Ciochetto, A. B. (2017). Global evaluation of
1331 particulate organic carbon flux parameterizations and implications for atmospheric pCO₂.
1332 *Global Biogeochem. Cycles*, *31*, 1192-1215. doi: 10.1002/2016GB005535
- 1333 Gonçalves-Araujo, R., de Souza, M. S., Mendes, C. R. B., Tavano, V. M., & Garcia, C. A. E.
1334 (2016). Seasonal change of phytoplankton (spring vs. summer) in the southern Patagonian
1335 shelf. *Continental Shelf Research*, *124*, 142-152. doi: 10.1016/j.csr.2016.03.023
- 1336 Graham, J. A., O'Dea, E., Holt, J., Polton, J., Hewitt, H. T., Furner, R., ... May-
1337 orga Adame, C. G. (2018a). AMM15: a new high resolution NEMO configuration for
1338 operational simulation of the European north-west shelf. *Geoscientific Model Develop-*
1339 *ment*, *11*, 681-696. doi: 10.5194/gmd-11-681-2018
- 1340 Graham, J. A., Rosser, J. P., O'Dea, E., & Hewitt, H. T. (2018b). Resolving Shelf Break Ex-
1341 change Around the European Northwest Shelf. *Geophysical Research Letters*, *45*, 12386-
1342 12395.
- 1343 Gregor, L., Lebehot, A. D., Kok, S., & Scheel Monteiro, P. M. (2019). A comparative
1344 assessment of the uncertainties of global surface ocean CO₂ estimates using a machine-
1345 learning ensemble (CSIR-ML6 version 2019a) – have we hit the wall? *Geoscientific Model*
1346 *Development*, *12*, 5113-5136. doi: 10.5194/gmd-12-5113-2019
- 1347 Gröger, M., Maier-Reimer, E., Mikolajewicz, U., Moll, A., & Sein, D. (2013). NW Euro-
1348 pean shelf under climate warming: implications for open ocean - shelf exchange, primary
1349 production, and carbon absorption. *Biogeosciences*, *10*, 3767-3792.
- 1350 Gruber, N. (2015). Ocean biogeochemistry: Carbon at the coastal interface. *Nature*,
1351 *517*(7533), 148-149. doi: 10.1038/nature14082
- 1352 Guidi, L., Legendre, L., Reygondeau, G., Uitz, J., Stemmann, L., & Henson, S. A. (2015). A
1353 new look at ocean carbon remineralization for estimating deepwater sequestration. *Global*
1354 *Biogeochem. Cycles*, *29*, 1044-1059. doi: 10.1002/2014GB005063
- 1355 Guihou, K., Piola, A. R., Palma, E. D., & Chidichimo, M. P. (2020). Dynamical con-
1356 nections between large marine ecosystems of austral South America based on numerical
1357 simulations. *Ocean Science*, *16*, 271-290. doi: 10.5194/os-16-271-2020
- 1358 Guihou, K., Polton, J., Harle, J., Wakelin, S., O'Dea, E., & Holt, J. (2018). Kilometric Scale
1359 Modeling of the North West European Shelf Seas: Exploring the Spatial and Temporal
1360 Variability of Internal Tides. *Journal of Geophysical Research: Oceans*, *123*, 688-707.
1361 doi: 10.1002/2017JC012960

- 1362 Gutjahr, O., Brüggemann, N., Haak, H., Jungclaus, J., Putrasahan, D., Lohmann, K., &
1363 von Storch, J. (2021). Comparison of ocean vertical mixing schemes in the Max Planck
1364 Institute Earth System Model (MPI-ESM1.2). *Geophysical Model Development*, *14*, 2317-
1365 2349. doi: 10.5194/gmd-14-2317-2021
- 1366 Hagemann, S., & Dümenil-Gates, L. (2001). Validation of the hydrological cycle of ECMWF
1367 and NCEP reanalyses using the MPI hydrological discharge model. *Journal of Geophysical
1368 Research - Atmospheres*, *106*, 1503-1510.
- 1369 Hagemann, S., Stacke, T., & Ho-Hagemann, H. T. M. (2020). High Resolution Discharge
1370 Simulations Over Europe and the Baltic Sea Catchment. *Frontiers in Earth Science*, *8*,
1371 12 pp. doi: 10.3389/feart.2020.00012
- 1372 Hallberg, R. (2013). Using a resolution function to regulate parameterizations of oceanic
1373 mesoscale eddy effects. *Ocean Modelling*, *72*, 92-103. doi: 10.1016/j.ocemod.2013.08.007
- 1374 Hartmann, J., Jansen, N., Dürr, H. H., Kempe, S., & Köhler, P. (2009). Global CO₂-
1375 consumption by chemical weathering: What is the contribution of highly active weathering
1376 regions? *Global and Planetary Change*, *69*, 185-194. doi: 10.1016/j.gloplacha.2009.07
1377 .007
- 1378 Hátún, H., Azetsu-Scott, K., Somavilla, R., Rey, F., Johnson, C., Mathis, M., ... Ólafsson,
1379 J. (2017). The subpolar gyre regulates silicate concentrations in the North Atlantic.
1380 *Scientific Reports*, *7*(14576), 9 pp.
- 1381 Hauck, J., Zeising, M., Quéré, C. L., Gruber, N., Bakker, D. C. E., Bopp, L., ... Séférian,
1382 R. (2020). Consistency and Challenges in the Ocean Carbon Sink Estimate for the Global
1383 Carbon Budget. *Frontiers in Marine Science*, *7*, 22 pp. doi: 10.3389/fmars.2020.571720
- 1384 Heinze, C., Maier-Reimer, E., Winguth, A. M. E., & Archer, D. (1999). A global oceanic
1385 sediment model for long-term climate studies. *Global Biogeochem. Cycles*, *13*, 221-250.
- 1386 Hewitt, H. T., Bell, M. J., Chassignet, E. P., Czaja, A., Ferreira, D., Griffies, S. M., ...
1387 Roberts, M. J. (2017). Will high-resolution global ocean models benefit coupled pre-
1388 dictions on short-range to climate timescales? *Ocean Modelling*, *120*, 120-136. doi:
1389 10.1016/j.ocemod.2017.11.002
- 1390 Hewitt, H. T., Roberts, M., Mathiot, P., Biastoch, A., Blockley, E., Chassignet, E. P., ...
1391 Zhang, Q. (2020). Resolving and Parameterising the Ocean Mesoscale in Earth System
1392 Models. *Curr. Clim. Change Rep.*, *6*, 137-152. doi: 10.1007/s40641-020-00164-w
- 1393 Hoch, K. E., Petersen, M. R., Brus, S. R., Engwirda, D., Roberts, A. F., Rosa, K. L., &
1394 Wolfram, P. J. (2020). MPAS-Ocean Simulation Quality for Variable-Resolution North
1395 American Coastal Meshes. *Journal of Advances in Modeling Earth Systems*, *12*, 23 pp.
1396 doi: 10.1029/2019MS001848
- 1397 Holt, J., Butenschön, M., Wakelin, S. L., Artioli, Y., & Allen, J. I. (2012). Oceanic
1398 controls on the primary production of the northwest European continental shelf: model
1399 experiments under recent past conditions and a potential future scenario. *Biogeosciences*,
1400 *9*(1), 97-117.
- 1401 Holt, J., Harle, J., Proctor, R., Michel, S., Ashworth, M., Batstone, C., ... Smith, G.
1402 (2009). Modelling the global coastal ocean. *Philosophical Transactions of the Royal
1403 Society A: Mathematical, Physical and Engineering Sciences*, *367*, 939-951. doi: 10.1098/
1404 rsta.2008.0210
- 1405 Holt, J., Hyder, P., Ashworth, M., Harle, J., Hewitt, H. T., Liu, H., ... Wood, R. (2017).
1406 Prospects for improving the representation of coastal and shelf seas in global ocean models.
1407 *Geoscientific Model Development*, *10*, 499-523. doi: 10.5194/gmd-10-499-2017
- 1408 Holt, J., & Proctor, R. (2008). The seasonal circulation and volume transport on the
1409 northwest European continental shelf: A fine-resolution model study. *J. Geophys. Res.*,
1410 *113*, 20 pp. doi: 10.1029/2006JC004034
- 1411 Holt, J., Schrum, C., Cannaby, H., Daewel, U., Allen, I., Artioli, Y., ... Wakelin, S. (2016).
1412 Potential impacts of climate change on the primary production of regional seas: A com-
1413 parative analysis of five European seas. *Progress in Oceanography*, *140*, 91-115.
- 1414 Hu, J., Kawamura, H., Li, C., Hong, H., & Jiang, Y. (2010). Review on current and seawater
1415 volume transport through the Taiwan Strait. *Journal of Oceanography*, *66*, 591-610. doi:

- 1416 10.1007/s10872-010-0049-1
- 1417 Hu, L. M., Lin, T., Shi, X. F., Yang, Z. S., Wang, H. J., Zhang, G., & Guo, Z. G. (2011). The
1418 role of shelf mud depositional process and large river inputs on the fate of organochlorine
1419 pesticides in sediments of the Yellow and East China seas. *Geophysical Research Letters*,
1420 *38*, 6 pp. doi: 10.1029/2010GL045723
- 1421 Huang, W. J., Cai, W. J., Wang, Y., Lohrenz, S. E., & Murrell, M. C. (2015). The carbon
1422 dioxide system on the Mississippi River-dominated continental shelf in the northern Gulf
1423 of Mexico: 1. Distribution and air-sea CO₂ flux. *Journal of Geophysical Research: Oceans*,
1424 *120*, 1429-1445. doi: 10.1002/2014JC010498
- 1425 Hurd, D. C. (1972). Factors affecting solution rate of biogenic opal in seawater. *Earth and*
1426 *Planetary Science Letters*, *15*, 411-417. doi: 10.1016/0012-821X(72)90040-4
- 1427 Ilyina, T., Six, K. D., Segschneider, J., Maier-Reimer, E., Li, H., & Núñez-Riboni, I. (2013).
1428 The global ocean biogeochemistry model HAMOCC: Model architecture and performance
1429 as component of the MPI-Earth System Model in different CMIP5 experimental realiza-
1430 tions. *Journal of Advances in Modeling Earth Systems*, *5*, 287-315.
- 1431 Jersild, A., Delawalla, S., & Ito, T. (2021). Mesoscale eddies regulate seasonal iron sup-
1432 ply and carbon drawdown in the Drake Passage. *Geophysical Research Letters*, *48*,
1433 e2021GL096020. doi: 10.1029/2021GL096020
- 1434 Jiao, N., Liang, Y., Zhang, Y., Liu, J., Zhang, Y., Zhang, R., . . . Zhang, S. (2018). Carbon
1435 pools and fluxes in the China Seas and adjacent oceans. *Science China Earth Sciences*,
1436 *61*, 1535-1563. doi: 10.1007/s11430-018-9190-x
- 1437 Kahl, L. C., Bianchi, A. A., Osiroff, A. P., Pino, D. R., & Piola, A. R. (2017). Distribution
1438 of sea-air CO₂ fluxes in the Patagonian Sea: Seasonal, biological and thermal effects.
1439 *Continental Shelf Research*, *143*, 18-28. doi: 10.1016/j.csr.2017.05.011
- 1440 Kaiser, K., Benner, R., & W., A. R. M. (2017). The fate of terrigenous dissolved organic
1441 carbon on the Eurasian shelves and export to the North Atlantic. *Scientific Reports*, *7*,
1442 11 pp. doi: 10.1038/s41598-017-12729-1
- 1443 Kamatani, A. (1982). Dissolution rates of silica from diatoms decomposing at various
1444 temperatures. *Marine Biology*, *68*, 91-96. doi: 10.1007/BF00393146
- 1445 Kämpf, J. (2021). On the upslope sediment transport at continental margins. *Journal of*
1446 *Marine Systems*, *219*, 103546. doi: 10.1016/j.jmarsys.2021.103546
- 1447 Kandasamy, S., & Nath, B. N. (2016). Perspectives on the Terrestrial Organic Matter
1448 Transport and Burial along the Land-Deep Sea Continuum: Caveats in Our Understand-
1449 ing of Biogeochemical Processes and Future Needs. *Front. Mar. Sci.*, *3*, 18 pp. doi:
1450 10.3389/fmars.2016.00259
- 1451 Karakaş, G., Nowald, N., Blaas, M., Marchesiello, P., Frickenhaus, S., & Schlitzer, R. (2006).
1452 High-resolution modeling of sediment erosion and particle transport across the northwest
1453 African shelf. *J. Geophys. Res.*, *111*, 13 pp. doi: 10.1029/2005JC003296
- 1454 Kartadikaria, A. R., Watanabe, A., Nadaoka, K., Adi, N. S., Prayitno, H. B., Soemo-
1455 rumekso, S., . . . Khasanah, E. N. (2015). CO₂ sink/source characteristics in the trop-
1456 ical Indonesian seas. *Journal of Geophysical Research: Oceans*, *120*, 7842-7856. doi:
1457 10.1002/2015JC010925
- 1458 Kastner, S. E., Horner-Devine, A. R., & Thomson, J. (2018). The influence of wind
1459 and waves on spreading and mixing in the Fraser River plume. *Journal of Geophysical*
1460 *Research: Oceans*, *123*, 6818-6840. doi: 10.1029/2018JC013765
- 1461 Ke, Z., & Yankovsky, A. (2010). The Hybrid Kelvin-Edge Wave and Its Role in Tidal
1462 Dynamic. *Journal of Physical Oceanography*, *40*, 2757-2767. doi: 10.1175/2010JPO4430
1463 .1
- 1464 Kealoha, A. K., Shamberger, K. E. F., DiMarco, S. F., Thyng, K. M., Hetland, R. D.,
1465 Manzello, D. P., . . . Enochs, I. C. (2020). Surface Water CO₂ variability in the Gulf of
1466 Mexico (1996-2017). *Scientific Reports*, *10*, 13 pp. doi: 10.1038/s41598-020-68924-0
- 1467 Kerimoglu, O., Voynova, Y. G., Chegini, F., Brix, H., Callies, U., Hofmeister, R., . . . van
1468 Beusekom, J. E. E. (2020). Interactive impacts of meteorological and hydrological condi-
1469 tions on the physical and biogeochemical structure of a coastal system. *Biogeosciences*,

- 1470 17, 5097-5127. doi: 10.5194/bg-17-5097-2020
- 1471 Kitidis, V., Shutler, J. D., Ashton, I., Warren, M., Brown, I., Findlay, H., ... Nightingale,
1472 P. D. (2019). Winter weather controls net influx of atmospheric CO₂ on the north-west
1473 European shelf. *Scientific Reports*, 9, 11 pp. doi: 10.1038/s41598-019-56363-5
- 1474 Kloster, S., Feichter, J., Maier-Reimer, E., Six, K. D., Stier, P., & Wetzzel, P. (2006). DMS
1475 cycle in the marine ocean-atmosphere system - A global model study. *Biogeosciences*, 3,
1476 29-51.
- 1477 Knutti, R., Stocker, T. F., & Wright, D. G. (1999). The Effects of Subgrid-Scale Parame-
1478 terizations in a Zonally Averaged Ocean Model. *Journal of Physical Oceanography*, 30,
1479 2738-2752.
- 1480 Korn, P. (2017). Formulation of an unstructured grid model for global ocean dynamics. *J.*
1481 *Comput. Phys.*, 339, 525-552. doi: 10.1016/j.jcp.2017.03.009
- 1482 Korn, P. (2018). A structure-preserving discretization of ocean parametrizations on un-
1483 structured grids. *Ocean Modelling*, 132, 73-90. doi: 10.1016/j.ocemod.2018.10.002
- 1484 Korn, P., & Linardakis, L. (2018). A conservative discretization of the shallow-water
1485 equations on triangular grids. *J. Comput. Phys.*, 375, 871â€“900. doi: 10.1016/j.jcp
1486 .2018.09.002
- 1487 Koul, V., Schrum, C., Dusterhus, A., & Baehr, J. (2019). Atlantic Inflow to the North Sea
1488 Modulated by the Subpolar Gyre in a Historical Simulation With MPI-ESM. *Journal of*
1489 *Geophysical Research: Oceans*, 124, 1807-1826. doi: 10.1029/2018JC014738
- 1490 Krumins, V., Gehlen, M., Arndt, S., Cappellen, P. V., & Regnier, P. (2013). Dissolved
1491 inorganic carbon and alkalinity fluxes from coastal marine sediments: model estimates
1492 for different shelf environments and sensitivity to global change. *Biogeosciences*, 10,
1493 371-398. doi: 10.5194/bg-10-371-2013
- 1494 Khn, W., Ptsch, J., Thomas, H., Borges, A. V., Schiettecatte, L.-S., Bozec, Y., & Prowe,
1495 A. E. F. (2010). Nitrogen and carbon cycling in the North Sea and exchange with the
1496 North Atlantic - A model study, Part II: Carbon budget and fluxes. *Continental Shelf*
1497 *Research*, 30, 1701-1716.
- 1498 Kulk, G., Platt, T., Dingle, J., Jackson, T., Jnsson, B. F., Bouman, H. A., ... Sathyen-
1499 dranath, S. (2020). Primary Production, an Index of Climate Change in the Ocean:
1500 Satellite-Based Estimates over Two Decades. *Remote Sensing*, 12, 26 pp. doi: 10.3390/
1501 rs12050826
- 1502 Kwon, E. Y., Primeau, F., & Sarmiento, J. L. (2009). The impact of remineralization depth
1503 on the air-sea carbon balance. *Nature Geoscience*, 2, 630-635. doi: 10.1038/ngeo612
- 1504 Lacroix, F., Ilyina, T., & Hartmann, J. (2020). Oceanic CO₂ outgassing and biological
1505 production hotspots induced by pre-industrial river loads of nutrients and carbon in a
1506 global modeling approach. *Biogeosciences*, 17, 55-88. doi: 10.5194/bg-17-55-2020
- 1507 Lacroix, F., Ilyina, T., Laruelle, G. G., & Regnier, P. (2021a). Reconstructing the Preindus-
1508 trial Coastal Carbon Cycle Through a Global Ocean Circulation Model: Was the Global
1509 Continental Shelf Already Both Autotrophic and a CO₂ Sink? *Global Biogeochemical*
1510 *Cycles*, 35, e2020GB006603. doi: 10.1029/2020GB006603
- 1511 Lacroix, F., Ilyina, T., Mathis, M., Laruelle, G. G., & Regnier, P. (2021b). Historical
1512 Increases in Land-Derived Nutrient Inputs May Alleviate Effects of a Changing Physical
1513 Climate on the Oceanic Carbon Cycle. *Global Change Biology*, in press. doi: 10.1111/
1514 gcb.15822
- 1515 Landschtzer, P., Gruber, N., & Bakker, D. C. E. (2016). Decadal variations and trends
1516 of the global ocean carbon sink. *Global Biogeochemical Cycles*, 30, 1396-1417. doi:
1517 10.1002/2015GB005359
- 1518 Laruelle, G., Lauerwald, R., Pfeil, B., & Regnier, P. (2014). Regionalized global budget of
1519 the CO₂ exchange at the air-water interface in continental shelf seas. *Global Biogeochem-
1520 ical Cycles*, 28(11), 1199-1214. doi: 10.1002/2014GB004832
- 1521 Laruelle, G. G., Cai, W. J., Hu, X., Gruber, N., Mackenzie, F. T., & Regnier, P. (2018).
1522 Continental shelves as a variable but increasing global sink for atmospheric carbon dioxide.
1523 *Nature Communications*, 9, 11 pp. doi: 10.1038/s41467-017-02738-z

- 1524 Laruelle, G. G., Dürr, H. H., Slomp, C. P., & Borges, A. V. (2010). Evaluation of sinks
1525 and sources of CO₂ in the global coastal ocean using a spatially-explicit typology of
1526 estuaries and continental shelves. *Geophysical Research Letters*, *37*, L15607. doi: 10.1029/
1527 2010GL043691
- 1528 Laufkötter, C., John, J. G., Stock, C. A., & Dunne, J. P. (2017). Temperature and oxygen
1529 dependence of the remineralization of organic matter. *Global Biogeochem. Cycles*, *31*,
1530 1038-1050. doi: 10.1002/2017GB005643
- 1531 Laufkötter, C., Vogt, M., Gruber, N., Aita-Noguchi, M., Aumont, O., Bopp, L., ... Völker,
1532 C. (2015). Drivers and uncertainties of future global marine primary production in marine
1533 ecosystem models. *Biogeosciences*, *12*, 6955-6984. doi: 10.5194/bg-12-6955-2015
- 1534 Lavelle, J. W., Thurnherr, A. M., Mullineaux, L. S., McGillicuddy, D. J., & Ledwell, J. R.
1535 (2012). The Prediction, Verification, and Significance of Flank Jets at Mid-Ocean Ridges.
1536 *Oceanography*, *25*, 277-283.
- 1537 Lee, T. R., Wood, W. T., & Phrampus, B. J. (2019). A Machine Learning (kNN) Approach
1538 to Predicting Global Seafloor Total Organic Carbon. *Global Biogeochemical Cycles*, *33*,
1539 37-46. doi: 10.1029/2018GB005992
- 1540 Legge, O., Johnson, M., Hicks, N., Jickells, T., Diesing, M., Aldridge, J., ... Williamson,
1541 P. (2020). Carbon on the Northwest European Shelf: Contemporary Budget and Future
1542 Influences. *Frontiers in Marine Science*, *7*, 23 pp. doi: 10.3389/fmars.2020.00143
- 1543 Lemmen, C. (2018). North Sea Ecosystem-Scale Model-Based Quantification of Net Primary
1544 Productivity Changes by the Benthic Filter Feeder *Mytilus edulis*. *Water*, *10*, 18 pp. doi:
1545 10.3390/w10111527
- 1546 Li, G., Gao, P., Wang, F., & Liang, Q. (2004). Estimation of ocean primary productivity
1547 and its spatio-temporal variation mechanism for East China Sea based on VGPM model.
1548 *Journal of Geographical Sciences*, *14*, 32-40. doi: 10.1007/BF02873088
- 1549 Li, M., Peng, C., Wang, M., Xue, W., Zhang, K., Wang, K., ... Zhu, Q. (2017). The
1550 carbon flux of global rivers: A re-evaluation of amount and spatial patterns. *Ecological*
1551 *Indicators*, *80*, 40-51. doi: 10.1016/j.ecolind.2017.04.049
- 1552 Li, M., Peng, C., Zhou, X., Yang, Y., Guo, Y., Shi, G., & Zhu, Q. (2019). Modeling Global
1553 Riverine DOC Flux Dynamics From 1951 to 2015. *Journal of Advances in Modeling Earth*
1554 *Systems*, *11*, 514-530. doi: 10.1029/2018MS001363
- 1555 Li, Z., von Storch, J. S., & Müller, M. (2017). The K1 internal tide simulated by a 1/10°
1556 OGCM. *Ocean Modelling*, *113*, 145-156. doi: 10.1016/j.ocemod.2017.04.002
- 1557 Lie, H. J., & Cho, C. H. (2016). Seasonal circulation patterns of the Yellow and East
1558 China Seas derived from satellite-tracked drifter trajectories and hydrographic observa-
1559 tions. *Progress in Oceanography*, *146*, 121-141. doi: 10.1016/j.pocean.2016.06.004
- 1560 Liu, F., Su, J., Moll, A., Krasemann, H., X. Chen, T. P., & Wirtz, K. (2014). Assessment
1561 of the summer-autumn bloom in the Bohai Sea using satellite images to identify the roles
1562 of wind mixing and light conditions. *Journal of Marine Systems*, *129*, 303-317. doi:
1563 10.1016/j.jmarsys.2013.07.007
- 1564 Liu, X., Dunne, J. P., Stock, C. A., Harrison, M. J., Adcroft, A., & Resplandy, L. (2019).
1565 Simulating Water Residence Time in the Coastal Ocean: A Global Perspective. *Geophys-*
1566 *ical Research Letters*, *46*, 13910-13919. doi: 10.1029/2019GL085097
- 1567 Liu, Z., & Gan, J. (2016). Open boundary conditions for tidally and subtidally forced
1568 circulation in a limited-area coastal model using the Regional Ocean Modeling System
1569 (ROMS). *Journal of Geophysical Research: Oceans*, *121*, 6184-6203. doi: 10.1002/
1570 2016JC011975
- 1571 Liu, Z., Gan, J., Hu, J., Wu, H., Cai, Z., & Deng, Y. (2021). Progress on circulation
1572 dynamics in the East China Sea and southern Yellow Sea: Origination, pathways, and
1573 destinations of shelf currents. *Progress in Oceanography*, *193*, 102553. doi: 10.1016/
1574 j.pocean.2021.102553
- 1575 Liu, Z., Zhang, W., Xiong, X., & Zhu, S. (2021). Observational characteristics and dynamic
1576 mechanism of low-salinity water lens for the offshore detachment of the Changjiang River
1577 diluted water in August 2006. *Acta Oceanologica Sinica*, *40*, 34-45. doi: 10.1007/s13131

1578 -021-1710-9

- 1579 Locarnini, R. A., Mishonov, A. V., Antonov, J. I., Boyer, T. P., Garcia, H. E., Baranova,
1580 O. K., ... Seidov, D. (2013). World Ocean Atlas 2013, Volume 1: Temperature. *Levitus,*
1581 *S., Mishonov, A. (Eds.), NOAA Atlas NESDIS, 73*, 40 pp.
- 1582 Loebel, M., Colijn, F., van Beusekom, J. E. E., Baretta-Bekker, J. G., Lancelot, C., Philip-
1583 part, C. J. M., ... Wiltshire, K. H. (2009). Recent patterns in potential phytoplankton
1584 limitation along the Northwest European continental coast. *Journal of Sea Research, 61*,
1585 34-43. doi: 10.1016/j.seares.2008.10.002
- 1586 Logemann, K., Linardakis, L., Korn, P., & Schrum, C. (2021). Global tide simulations with
1587 ICON-O: testing the model performance on highly irregular meshes. *Ocean Dynamics,*
1588 *71*, 43-57. doi: 10.1007/s10236-020-01428-7
- 1589 Lønborg, C., Álvarez Salgado, X. A., Letscher, R. T., & Hansell, D. A. (2018). Large
1590 Stimulation of Recalcitrant Dissolved Organic Carbon Degradation by Increasing Ocean
1591 Temperatures. *Front. Mar. Sci., 4*, 11 pp. doi: 10.3389/fmars.2017.00436
- 1592 Luisetti, T., Ferrini, S., Grilli, G., Jickells, T. D., Kennedy, H., Kröger, S., ... Tyllianakis,
1593 E. (2020). Climate action requires new accounting guidance and governance frameworks
1594 to manage carbon in shelf seas. *Nature Communications, 11*, 4599. doi: 10.1038/s41467-
1595 -020-18242-w
- 1596 Luo, X. (2014). Phytoplankton community and primary productivity in the Yellow Sea and
1597 East China Sea. In *Marine biodiversity and ecosystem dynamics of the northwest pacific*
1598 *ocean* (p. 13 pp). Science Press Beijing.
- 1599 Maerz, J., Hofmeister, R., van der Lee, E. M., Gräwe, U., Riethmüller, R., & Wirtz, K. W.
1600 (2016). Maximum sinking velocities of suspended particulate matter in a coastal transition
1601 zone. *Biogeosciences, 13*, 4863-4876. doi: 10.5194/bg-13-4863-2016
- 1602 Maerz, J., Six, K. D., Stemmler, I., Ahmerkamp, S., & Ilyina, T. (2020). Microstructure
1603 and composition of marine aggregates as co-determinants for vertical particulate organic
1604 carbon transfer in the global ocean. *Biogeosciences, 17*, 1765-1803. doi: 10.5194/bg-17-
1605 -1765-2020
- 1606 Maier-Reimer, E., Kriest, I., Segschneider, J., & Wetzel, P. (2005). The Hamburg Ocean
1607 Carbon Cycle Model HAMOCC5.1 - Technical Description Release 1.1. *Berichte zur*
1608 *Erdsystemforschung, 14*, 50 pp. (Max Planck Institute for Meteorology, Hamburg, Ger-
1609 many)
- 1610 Marrec, P., Cariou, T., Macé, E., Morin, P., Salt, L. A., Vernet, M., ... Bozec, Y. (2015).
1611 Dynamics of air-sea CO₂ fluxes in the northwestern European shelf based on voluntary
1612 observing ship and satellite observations. *Biogeosciences, 12*, 5371-5391. doi: 10.5194/
1613 bg-12-5371-2015
- 1614 Marsaleix, P., Auclair, F., & Estournel, C. (2006). Considerations on Open Boundary
1615 Conditions for Regional and Coastal Ocean Models. *Journal of Atmospheric and Oceanic*
1616 *Technology, 23*, 1604-1613. doi: 10.1175/JTECH1930.1
- 1617 Marsh, R., Haigh, I. D., Cunningham, S. A., Inall, M. E., Porter, M., & Moat, B. I. (2017).
1618 Large-scale forcing of the European Slope Current and associated inflows to the North
1619 Sea. *Ocean Science, 13*, 315-335.
- 1620 Mathis, M., Elizalde, A., & Mikolajewicz, U. (2018). Which complexity of regional climate
1621 system models is essential for downscaling anthropogenic climate change in the Northwest
1622 European Shelf? *Climate Dynamics, 50*, 2637-2659.
- 1623 Mathis, M., Elizalde, A., & Mikolajewicz, U. (2019). The future regime of Atlantic nutrient
1624 supply to the Northwest European Shelf. *J. Mar. Syst., 189*, 98-115. doi: 10.1016/
1625 j.jmarsys.2018.10.002
- 1626 Mathis, M., Elizalde, A., Mikolajewicz, U., & Pohlmann, T. (2015). Variability patterns of
1627 the general circulation and sea water temperature in the North Sea. *Prog. Oceanog., 135*,
1628 91-112.
- 1629 Mathis, M., Mayer, B., & Pohlmann, T. (2013). An uncoupled dynamical downscaling for
1630 the North Sea: Method and evaluation. *Ocean Modelling, 72*, 153-166.
- 1631 Mauritsen, T., Bader, J., Becker, T., Behrens, J., Bittner, M., Brokopf, R., ... Roeckner,

- 1632 E. (2019). Developments in the MPI-M Earth System Model version 1.2 (MPI-ESM1.2)
 1633 and its response to increasing CO₂. *Journal of Advances in Modeling Earth Systems*, *11*,
 1634 998-1038. doi: 10.1029/2018MS001400
- 1635 Mayer, B., Rixen, T., & Pohlmann, T. (2018). The Spatial and Temporal Variability of
 1636 Air-Sea CO₂ Fluxes and the Effect of Net Coral Reef Calcification in the Indonesian Seas:
 1637 A Numerical Sensitivity Study. *Frontiers in Marine Science*, *5*, 19 pp. doi: 10.3389/
 1638 fmars.2018.00116
- 1639 Meybeck, M. (1982). Carbon, Nitrogen, and Phosphorus Transport by World Rivers. *Am.*
 1640 *J. Sci.*, *282*, 401-450. doi: 10.2475/ajs.282.4.401
- 1641 Meybeck, M., & Vörösmarty, C. (1999). Global Transfer of Carbon by Rivers. *Global*
 1642 *Change Newsletters, IGBP Newsletter No. 37*, 18-19.
- 1643 Middelburg, J. J., Soetaert, K., & Hagens, M. (2020). Ocean Alkalinity, Buffering and
 1644 Biogeochemical Processes. *Reviews of Geophysics*, *58*, e2019RG000681. doi: 10.1029/
 1645 2019RG000681
- 1646 Moat, B. I., Frajka-Williams, E., Smeed, D., Rayner, D., Sanchez-Franks, A., Johns,
 1647 W. E., ... Collins, J. (2020). Atlantic meridional overturning circulation observed by
 1648 the RAPID-MOCHA-WBTS (RAPID-Meridional Overturning Circulation and Heatflux
 1649 Array-Western Boundary Time Series) array at 26N from 2004 to 2018 (v2018.2). *British*
 1650 *Oceanographic Data Centre, National Oceanography Centre, NERC, UK*. doi: 10/d3z4
- 1651 Moll, A. (1998). Regional distribution of primary production in the North Sea simulated
 1652 by a three-dimensional model. *Journal of Marine Systems*, *16*, 151-170.
- 1653 Muller-Karger, F. E., Varela, R., Thunell, R. C., Luerssen, R., Hu, C., & Walsh, J. J. (2005).
 1654 The importance of continental margins in the global carbon cycle. *Geophys. Res. Letters*,
 1655 *32*, L01602. doi: 10.1029/2004GL021346
- 1656 Najjar, R. G., Jin, X., Louanchi, F., Aumont, O., Caldeira, K., Doney, S. C., ... Yool,
 1657 A. (2007). Impact of circulation on export production, dissolved organic matter, and
 1658 dissolved oxygen in the ocean: Results from Phase II of the Ocean Carbon-cycle Model
 1659 Intercomparison Project (OCMIP-2). *Global Biogeochemical Cycles*, *21*, 22 p. doi: 10
 1660 .1029/2006GB002857
- 1661 Nellemann, C., Corcoran, E., Duarte, C., Valdes, L., Young, C., Fonseca, L., & Grimsditch,
 1662 G. (2009). Blue Carbon - The Role of Healthy Oceans in Binding Carbon. *A Rapid*
 1663 *Response Assessment. United Nations Environment Programme*.
- 1664 Oguz, T., Macias, D., , & Tintore, J. (2015). Ageostrophic frontal processes controlling
 1665 phytoplankton production in the Catalano-Balearic Sea (Western Mediterranean). *PLoS*
 1666 *One*, *10*, 22 pp. doi: 10.1371/journal.pone.0129045
- 1667 O'Meara, T., Gibbs, E., & Thrush, S. F. (2018). Rapid organic matter assay of organic
 1668 matter degradation across depth gradients within marine sediments. *Methods Ecol. Evol.*,
 1669 *9*, 245-253. doi: 10.1111/2041-210X.12894
- 1670 Oschlies, A. (2008). Eddies and Upper-Ocean Nutrient Supply. *Geophysical Monograph*
 1671 *Series*, *177*, 115-130. doi: 10.1029/177GM09
- 1672 Pain, C. C., Piggott, M. D., Goddard, A. J. H., Fang, F., Gorman, G. J., Marshall, D. P.,
 1673 ... de Oliveira, C. R. E. (2005). Three-dimensional unstructured mesh ocean modelling.
 1674 *Ocean Modelling*, *10*, 5-33. doi: 10.1016/j.ocemod.2004.07.005
- 1675 Painter, S. C., Hartman, S. E., Kivimäe, C., Salt, L. A., Clargo, N. M., Bozec, Y., ...
 1676 Allen, S. R. (2016). Carbon exchange between a shelf sea and the ocean: The Hebrides
 1677 Shelf, west of Scotland. *Journal of Geophysical Research: Oceans*, *121*, 4522-4544. doi:
 1678 10.1002/2015JC011599
- 1679 Painting, S. J., Collingridge, K. A., Durand, D., Grémare, A., Créach, V., Arvanitidis, C., &
 1680 Bernard, G. (2020). Marine monitoring in Europe: is it adequate to address environmental
 1681 threats and pressures? *Ocean Sci.*, *16*, 235-252. doi: 10.5194/os-16-235-2020
- 1682 Palastanga, V., Slomp, C. P., & Heinze, C. (2011). Long-term controls on ocean phosphorus
 1683 and oxygen in a global biogeochemical model. *Global Biogeochemical Cycles*, *25*, 19 pp.
 1684 doi: 10.1029/2010GB003827
- 1685 Park, G. H., Wanninkhof, R., Doney, S. C., Takahashi, T., Lee, K., Feely, R. A., ... Lima,

- 1686 I. (2010). Variability of global air-sea CO₂ fluxes over the last three decades. *Tellus*,
1687 *62B*, 352-368. doi: 10.1111/j.1600-0889.2010.00498.x
- 1688 Pätzsch, J., Burchard, H., Dieterich, C., Gräwe, U., Gröger, M., Mathis, M., ... Eden, C.
1689 (2017). An evaluation of the North Sea circulation in global and regional models relevant
1690 for ecosystem simulations. *Ocean Modelling*, *116*, 70-95. doi: 10.1016/j.ocemod.2017.06
1691 .005
- 1692 Paulsen, H., Ilyina, T., Six, K. D., & Stemmler, I. (2017). Incorporating a prognostic repre-
1693 sentation of marine nitrogen fixers into the global ocean biogeochemical model HAMOCC.
1694 *Journal of Advances in Modeling Earth Systems*, *9*, 438-464. doi: 10.1002/2016MS000737
- 1695 Piggott, M. D., Pain, C. C., Gorman, G. J., Marshall, D. P., & Killworth, P. D. (2008).
1696 Unstructured Adaptive Meshes for Ocean Modeling. In M. W. Hecht & H. Hasumi (Eds.),
1697 *Ocean modeling in an eddying regime* (p. 383-408). American Geophysical Union (AGU).
1698 doi: 10.1029/177GM22
- 1699 Pimenta, F. M., Campos, E. J. D., Miller, J. L., & Piola, A. R. (2005). A numerical study
1700 of the Plata River plume along the southeastern South American continental shelf. *Braz.*
1701 *J. Oceanogr.*, *53*, 129-146.
- 1702 Piola, A. R., Palma, E. D., Bianchi, A. A., Castro, B. M., Dottori, M., Guerrero, R. A., ...
1703 Saraceno, M. (2018). Physical Oceanography of the SW Atlantic Shelf: A Review. In
1704 M. Hoffmeyer, M. Sabatini, F. Brandini, D. Calliari, & S. N. (Eds.), *Plankton Ecology of*
1705 *the Southwestern Atlantic* (p. 37-56). Springer, Cham. doi: 10.1007/978-3-319-77869-3_2
- 1706 Pipko, I. I., Pugach, S. P., Semiletov, I. P., Anderson, L. G., Shakhova, N. E., Gustafsson,
1707 O., ... Dudarev, O. V. (2017). The spatial and interannual dynamics of the surface water
1708 carbonate system and air-sea CO₂ fluxes in the outer shelf and slope of the Eurasian Arctic
1709 Ocean. *Ocean Science*, *13*, 997-1016. doi: 10.5194/os-13-997-2017
- 1710 Poulain, P. M., & Centurioni, L. (2015). Direct measurements of World Ocean tidal cur-
1711 rents with surface drifters. *J. Geophys. Res. Oceans*, *120*, 6986-7003. doi: 10.1002/
1712 2015JC010818
- 1713 Pradal, M. A., & Gnanadesikan, A. (2014). How does the Redi parameter for mesoscale
1714 mixing impact global climate in an Earth System Model? *Journal of Advances in Modeling*
1715 *Earth Systems*, *6*, 586-601. doi: 10.1002/2013MS000273
- 1716 Provoost, P., Braeckman, U., van Gansbeke, D., Moodley, L., Soetaert, K., Middelburg,
1717 J. J., & Vanaverbeke, J. (2013). Modelling benthic oxygen consumption and benthic-
1718 pelagic coupling at a shallow station in the southern North Sea. *Estuarine, Coastal and*
1719 *Shelf Science*, *120*, 1-11. doi: 10.1016/j.ecss.2013.01.008
- 1720 Provoost, P., van Heuven, S., Soetaert, K., Laane, R. W. P. M., & Middelburg, J. J. (2010).
1721 Seasonal and long-term changes in pH in the Dutch coastal zone. *Biogeosciences*, *7*,
1722 3869-3878. doi: 10.5194/bg-7-3869-2010
- 1723 Quante, M., Colijn, F., Bakker, J. P., Härdtle, W., Heinrich, H., Lefebvre, C., ... Tölle,
1724 M. H. (2016). Introduction to the Assessment - Characteristics of the Region. In
1725 M. Quante & F. Colijn (Eds.), *North Sea Region Climate Change Assessment* (p. 175-
1726 217). Springer Berlin - Heidelberg.
- 1727 Regnier, P., Friedlingstein, P., Ciais, P., Mackenzie, F. T., Gruber, N., Janssens, I. A., ...
1728 Thullner, M. (2013). Anthropogenic perturbation of the carbon fluxes from land to ocean.
1729 *Nature Geoscience*, *6*, 597-607. doi: 10.1038/ngeo1830
- 1730 Remacle, J. F., & Lambrechts, J. (2018). Fast and robust mesh generation on the sphere -
1731 Application to coastal domains. *Computer-Aided Design*, *103*, 14-23. (25th International
1732 Meshing Roundtable Special Issue: Advances in Mesh Generation) doi: 10.1016/j.cad
1733 .2018.03.002
- 1734 Resplandy, L., Keeling, R. F., Rödenbeck, C., Stephens, B. B., Khatiwala, S., Rodgers,
1735 K. B., ... Tans, P. P. (2018). Revision of global carbon fluxes based on a reassessment
1736 of oceanic and riverine carbon transport. *Nat. Geosci.*, *11*, 504-509. doi: 10.1038/
1737 s41561-018-0151-3
- 1738 Reynaud, J. Y., & Dalrymple, R. (2012). Shallow-Marine Tidal Deposits. In R. A. J. Davis &
1739 R. W. Dalrymple (Eds.), *Principles of tidal sedimentology* (p. 335-369). Springer Science

- 1740 and Business Media B. V. doi: 10.1007/978-94-007-0123-6_13
- 1741 Richardson, K., & Bendtsen, J. (2019). Vertical distribution of phytoplankton and primary
1742 production in relation to nutricline depth in the open ocean. *Mar. Ecol. Progr. Ser.*, *620*,
1743 33-46. doi: 10.3354/meps12960
- 1744 Ridgwell, A. J., Watson, A. J., & Archer, D. E. (2002). Modeling the response of the
1745 oceanic Si inventory to perturbation, and consequences for atmospheric CO₂. *Global
1746 Biogeochemical Cycles*, *16*, 26 pp. doi: 10.1029/2002GB001877
- 1747 Rippeth, T. P., Lincoln, B. J., Kennedy, H. A., Palmer, M. R., Sharples, J., & Williams,
1748 C. A. J. (2014). Impact of vertical mixing on sea surface pCO₂ in temperate sea-
1749 sonally stratified shelf seas. *J. Geophys. Res. Oceans*, *119*, 3868-3882. doi: 10.1002/
1750 2014JC010089
- 1751 Roobaert, A., Laruelle, G. G., Landschützer, P., Gruber, N., Chou, L., & Regnier, P. (2019).
1752 The spatiotemporal dynamics of the sources and sinks of CO₂ in the global coastal ocean.
1753 *Global Biogeochemical Cycles*, *33*, 1693-1714. doi: 10.1029/2019GB006239
- 1754 Schartau, M., Riethmüller, R., Flöser, G., van Beusekom, J. E. E., Krasemann, H., Hofmeis-
1755 ter, R., & Wirtz, K. (2019). On the separation between inorganic and organic fractions
1756 of suspended matter in a marine coastal environment. *Progress in Oceanography*, *171*,
1757 231-250. doi: 10.1016/j.pocean.2018.12.011
- 1758 Schmidt, S., Neumann, B., Waweru, Y., Durussel, C., Unger, S., & Visbeck, M. (2017).
1759 SDG14 Conserve and Sustainably Use the Oceans, Seas and Marine Resources for Sus-
1760 tainable Development. In D. J. Griggs, M. Nilsson, A. Stevance, & D. McCollum (Eds.),
1761 *A guide to sdg interactions: from science to implementation* (p. 174-218). International
1762 Council for Science (ICSU), Paris. doi: 10.24948/2017.01
- 1763 Séférian, R., Berthet, S., Yool, A., Palmiéri, J., Bopp, L., Tagliabue, A., ... Yamamoto,
1764 A. (2020). Tracking Improvement in Simulated Marine Biogeochemistry Between CMIP5
1765 and CMIP6. *Curr. Clim. Change Rep.*, *6*, 95-119. doi: 10.1007/s40641-020-00160-0
- 1766 Sein, D., Mikolajewicz, U., Gröger, M., Fast, I., Cabos, I., Pinto, J., ... Jacob, D. (2015).
1767 Regionally coupled atmosphere-ocean-sea ice-marine biogeochemistry model ROM. Part
1768 I: Description and validation. *J. Adv. Model. Earth Syst.*, *7*, 268-304.
- 1769 Sein, D. V., Koldunov, N. V., Danilov, S., Wang, Q., Sidorenko, D., Fast, I., ... Jung, T.
1770 (2017). Ocean modeling on a mesh with resolution following the local Rossby radius. *Jour-
1771 nal of Advances in Modeling Earth Systems*, *9*, 2601-2614. doi: 10.1002/2017MS001099
- 1772 Seitzinger, S. P., Mayorga, E., Bouwman, A. F., Kroeze, C., Beusen, A. H. W., Billen, G.,
1773 ... Harrison, J. A. (2010). Global river nutrient export: A scenario analysis of past and
1774 future trends. *Global Biogeochemical Cycles*, *24*, 16 pp. doi: 10.1029/2009GB003587
- 1775 Silsbe, G. M., Behrenfeld, M. J., Halsey, K. H., Milligan, A. J., & Westberry, T. K. (2016).
1776 The CAFE model: A net production model for global ocean phytoplankton. *Global
1777 Biogeochemical Cycles*, *30*, 1756-1777. doi: GlobalBiogeochemicalCycles
- 1778 Simmons, H. L., Jayne, S. R., St. Laurent, L. C., & Weaver, A. J. (2004). Tidally driven
1779 mixing in a numerical model of the ocean general circulation. *Ocean Modelling*, *6*, 245-
1780 263. doi: 10.1016/S1463-5003(03)00011-8
- 1781 Six, K. D., & Maier-Reimer, E. (1996). Effects of plankton dynamics on seasonal carbon
1782 fluxes in an ocean general circulation model. *Global Biogeochem. Cycles*, *10*, 559-583.
- 1783 Small, R., Campbell, T., Teixeira, J., Carniel, S., Smith, T., Dykes, J., ... Allard, R. (2011).
1784 Air-Sea Interaction in the Ligurian Sea: Assessment of a Coupled Ocean-Atmosphere
1785 Model Using In Situ Data from LASIE07. *Monthly Weather Review*, *139*, 1785-1808. doi:
1786 10.1175/2010MWR3431.1
- 1787 Song, J., Qu, B., Li, X., Yuan, H., Li, N., & Duan, L. (2018). Carbon sinks/sources in
1788 the Yellow and East China Seas - Air-sea interface exchange, dissolution in seawater,
1789 and burial in sediments. *Science China Earth Sciences*, *61*, 1583-1593. doi: 10.1007/
1790 s11430-017-9213-6
- 1791 Stolpovsky, K., Dale, A. W., & Wallmann, K. (2015). Toward a parameterization of
1792 global-scale organic carbon mineralization kinetics in surface marine sediments. *Global
1793 Biogeochemical Cycles*, *29*, 812-829. doi: 10.1002/2015GB005087

- 1794 Stuhne, G. R., & Peltier, W. R. (2009). An unstructured C-grid based method for 3-D
1795 global ocean dynamics: Free-surface formulations and tidal test cases. *Ocean Modelling*,
1796 *28*, 97-105. doi: 10.1016/j.ocemod.2008.11.005
- 1797 Su, J., Tian, T., Krasemann, H., Schartau, M., & Wirtz, K. (2015). Response patterns
1798 of phytoplankton growth to variations in resuspension in the German Bight revealed by
1799 daily MERIS data in 2003 and 2004. *Oceanologia*, *57*, 328-341. doi: 10.1016/j.oceano
1800 .2015.06.001
- 1801 Sündermann, J., & Pohlmann, T. (2011). A brief analysis of North Sea physics. *Oceanologia*,
1802 *53*(3), 663-689.
- 1803 Takahashi, T., Sutherland, S. C., Wanninkhof, R., Sweeney, C., Feely, R. A., Chipman,
1804 D. W., ... de Baar, H. J. (2009). Climatological mean and decadal change in surface
1805 ocean pCO₂, and net sea-air CO₂ flux over the global oceans. *Deep Sea Research Part*
1806 *II: Topical Studies in Oceanography*, *56*, 554-577. doi: 10.1016/j.dsr2.2008.12.009
- 1807 Tamburini, F., & Föllmi, K. B. (2009). Phosphorus burial in the ocean over glacial-
1808 interglacial time scales. *Biogeosciences*, *6*, 501-513. doi: 10.5194/bg-6-501-2009
- 1809 Tan, S., & Shi, G. (2006). Satellite-derived primary productivity and its spatial and temporal
1810 variability in the China seas. *Journal of Geographical Sciences*, *16*, 447-457. doi: 10.1007/
1811 s11442-006-0408-4
- 1812 Tan, S., & Shi, G. (2012). The relationship between satellite-derived primary production and
1813 vertical mixing and atmospheric inputs in the Yellow Sea cold water mass. *Continental*
1814 *Shelf Research*, *48*, 138-145. doi: 10.1016/j.csr.2012.07.015
- 1815 Taylor, K., Stouffer, R. J., & Meehl, G. A. (2012). An overview of CMIP5 and the experiment
1816 design. *Bull. Am. Meteorol. Soc.*, *93*, 485-498. doi: 10.1175/BAMS-D-11-00094.1
- 1817 Terhaar, J., Lauerwald, R., Regnier, P., Gruber, N., & Bopp, L. (2021). Around one third of
1818 current Arctic Ocean primary production sustained by rivers and coastal erosion. *Nature*
1819 *Communications*, *12*, 10 pp. doi: 10.1038/s41467-020-20470-z
- 1820 Thévenin, M. R., Pereira, J., & Lessa, G. C. (2019). Shelf-break upwelling on a very
1821 narrow continental shelf adjacent to a western boundary current formation zone. *Journal*
1822 *of Marine Systems*, *194*, 52-65. doi: 10.1016/j.jmarsys.2019.02.008
- 1823 Thomas, H., Bozec, Y., Elkalay, K., & de Baar, H. J. W. (2004). Enhanced Open Ocean
1824 Storage of CO₂ from Shelf Sea Pumping. *Science*, *304*(5673), 1005-1008.
- 1825 Toffoli, A., & Bitner-Gregersen, E. M. (2017). Types of Ocean Surface Waves, Wave
1826 Classification. In J. Carlton, P. Jukes, & Y. Choo (Eds.), *Encyclopedia of maritime and*
1827 *offshore engineering* (p. 1-8). John Wiley & Sons, Ltd. doi: 10.1002/9781118476406
1828 .emoe077
- 1829 Tréguer, P. J., & De La Rocha, C. L. (2013). The World Ocean Silica Cycle. *Annual Review*
1830 *of Marine Science*, *5*, 477-501. doi: 10.1146/annurev-marine-121211-172346
- 1831 Tréguer, P. J., Sutton, J. N., Brzezinski, M., Charette, M. A., Devries, T., Dutkiewicz, S.,
1832 ... Rouxel, O. (2021). Reviews and syntheses: The biogeochemical cycle of silicon in the
1833 modern ocean. *Biogeosciences*, *18*, 1269-1289. doi: 10.5194/bg-18-1269-2021
- 1834 Tseng, C. M., Liu, K. K., Gong, G. C., Shen, P. Y., & Cai, W. J. (2011). CO₂ uptake in the
1835 East China Sea relying on Changjiang runoff is prone to change. *Geophysical Research*
1836 *Letters*, *38*, 6 pp. doi: 10.1029/2011GL049774
- 1837 van Cappellen, P., Dixit, S., & van Beusekom, J. (2002). Biogenic silica dissolution in the
1838 oceans: Reconciling experimental and field-based dissolution rates. *Global Biogeochemical*
1839 *Cycles*, *16*, 10 pp. doi: 10.1029/2001GB001431
- 1840 van Leeuwen, S., Tett, P., Mills, D., & van der Molen, J. (2015). Stratified and nonstratified
1841 areas in the North Sea: Long-term variability and biological and policy implications. *J.*
1842 *Geophys. Res. Oceans*, *120*, 4670-4686. doi: 10.1002/2014JC010485
- 1843 Vantrepotte, V., Loisel, H., Dessailly, D., & Mériaux, X. (2012). Optical classification of
1844 contrasted coastal waters. *Remote Sensing of Environment*, *123*, 306-323. doi: 10.1016/
1845 j.rse.2012.03.004
- 1846 Violante, R. A., Paterlini, C. M., Marcolini, S. I., Costa, I. P., Cavallotto, J. L., Laprida, C.,
1847 ... Osterrieth, M. L. (2014). The Argentine continental shelf: Morphology, sediments,

- 1848 processes and evolution since the last glacial maximum. *Geological Society Memoir*, *41*,
1849 55-68. doi: 10.1144/M41.6
- 1850 Volk, T., & Hoffert, M. I. (1985). Ocean Carbon Pumps: Analysis of Relative Strengths and
1851 Efficiencies in Ocean-Driven Atmospheric CO₂ Changes. In E. Sundquist & W. Broecker
1852 (Eds.), *The carbon cycle and atmospheric CO₂: Natural variations archean to present*
1853 (p. 99-110). American Geophysical Union (AGU). doi: 10.1029/GM032p0099
- 1854 Wallmann, K. (2010). Phosphorus imbalance in the global ocean? *Global Biogeochem.*
1855 *Cycles*, *24*, 12 pp. doi: 10.1029/2009GB003643
- 1856 Wang, S., Dieterich, C., Döscher, R., Höglund, A., Hordoir, R., Meier, H. E. M., ... Schi-
1857 manke, S. (2015). Development and evaluation of a new regional coupled atmosphere-
1858 ocean model in the North Sea and Baltic Sea. *Tellus A*, *67*, 20 pp. doi: 10.3402/
1859 tellusa.v67.24284
- 1860 Ward, N. D., Bianchi, T. S., Medeiros, P. M., Seidel, M., Richey, J. E., Keil, R. G., &
1861 Sawakuchi, H. O. (2017). Where Carbon Goes When Water Flows: Carbon Cycling
1862 across the Aquatic Continuum. *Frontiers in Marine Science*, *4*, 27 pp. doi: 10.3389/
1863 fmars.2017.00007
- 1864 Ward, N. D., Megonigal, J. P., Bond-Lamberty, B., Bailey, V. L., Butman, D., Canuel,
1865 E. A., ... Windham-Myers, L. (2020). Representing the function and sensitivity of
1866 coastal interfaces in Earth system models. *Nature Communications*, *11*, 14 pp. doi:
1867 10.1038/s41467-020-16236-2
- 1868 Weber, T., Cram, J. A., Leung, S. W., DeVries, T., & Deutsch, C. (2016). Deep ocean
1869 nutrients imply large latitudinal variation. *PNAS*, *113*, 8606-8611. doi: 10.1073/pnas
1870 .1604414113
- 1871 Weller, H., Browne, P., Budd, C., & Cullen, M. (2016). Mesh adaptation on the sphere
1872 using optimal transport and the numerical solution of a Monge-Ampère type equation.
1873 *Journal of Computational Physics*, *308*, 102-123. doi: 10.1016/j.jcp.2015.12.018
- 1874 Westberry, T., Behrenfeld, M., Siegel, D., & Boss, E. (2008). Carbon-based primary pro-
1875 ductivity modeling with vertically resolved photoacclimation. *Glob.Biogeochem. Cycles*,
1876 *22*, GB2024. doi: 10.1029/2007GB003078
- 1877 Williams, C., Sharples, J., Mahaffey, C., & Rippeth, T. (2013). Wind-driven nutrient pulses
1878 to the subsurface chlorophyll maximum in seasonally stratified shelf seas. *Geophysical*
1879 *Research Letters*, *40*, 1-6. doi: 10.1002/2013GL058171
- 1880 Wilson, R. J., & Heath, M. R. (2019). Increasing turbidity in the North Sea during
1881 the 20th century due to changing wave climate. *Ocean Science*, *15*, 1615-1625. doi:
1882 10.5194/os-15-1615-2019
- 1883 Wu, H., Wu, T., Shen, J., & Zhu, J. (2018). Dynamics of the Changjiang River Plume. In
1884 X. S. Liang & Y. Zhang (Eds.), *Coastal Environment, Disaster, and Infrastructure - A*
1885 *Case Study of China's Coastline*. London, UK.
- 1886 Wu, R., Lin, J., & Li, B. (2016). Spatial and Temporal Variability of Sea Surface Tem-
1887 perature in Eastern Marginal Seas of China. *Advances in Meteorology*, *2016*, 1-9. doi:
1888 10.1155/2016/3820720
- 1889 Xie, F., Tao, Z., Zhou, X., Lv, T., & Wang, J. (2019). Spatial and Temporal Variations
1890 of Particulate Organic Carbon Sinking Flux in Global Ocean from 2003 to 2018. *Remote*
1891 *Sens.*, *11*, 20 pp. doi: 10.3390/rs11242941
- 1892 Xue, P., Malanotte-Rizzoli, P., Wei, J., & Eltahir, E. (2020). Coupled Ocean-Atmosphere
1893 Modeling Over the Maritime Continent: A Review. *Journal of Geophysical Research:*
1894 *Oceans*, *125*. doi: 10.1029/2019JC014978
- 1895 Yang, S., Song, B., Ye, S., Laws, E., He, L., Li, J., ... Behling, H. (2019). Large-scale
1896 pollen distribution in marine surface sediments from the Bohai Sea, China: Insights into
1897 pollen provenance, transport, deposition, and coastal-shelf paleoenvironment. *Progress in*
1898 *Oceanography*, *178*, 17 pp. doi: 10.1016/j.pocean.2019.102183
- 1899 Yang, S., Wang, Z., Dou, Y., & Shi, X. (2014). A review of sedimentation since the Last
1900 Glacial Maximum on the continental shelf of eastern China. *Geological Society, London,*
1901 *Memoirs*, *41*, 293-303. doi: 10.1144/M41.21

- 1902 Yao, Z., He, R., Bao, X., Wu, D., & Song, J. (2012). M2 tidal dynamics in Bohai and
 1903 Yellow Seas: a hybrid data assimilative modeling study. *Ocean Dynamics*, *62*, 753-769.
 1904 doi: 10.1007/s10236-011-0517-1
- 1905 Yasunaka, S., Murata, A., Watanabe, E., Chierici, M., Fransson, A., van Heuven, S., ...
 1906 Wanninkhof, R. (2016). Mapping of the air-sea CO₂ flux in the Arctic Ocean and its
 1907 adjacent seas: Basin-wide distribution and seasonal to interannual variability. *Polar*
 1908 *Science*, *10*, 323-334. doi: 10.1016/j.polar.2016.03.006
- 1909 Yasunaka, S., Siswanto, E., Olsen, A., Hoppema, M., Watanabe, E., Fransson, A., ...
 1910 Mathis, J. T. (2018). Arctic Ocean CO₂ uptake: an improved multiyear estimate of the
 1911 air-sea CO₂ flux incorporating chlorophyll *a* concentrations. *Biogeosciences*, *15*, 1643-
 1912 1661. doi: 10.5194/bg-15-1643-2018
- 1913 Yuan, D., Zhu, J., Li, C., & Hu, D. (2008). Cross-shelf circulation in the Yellow and East
 1914 China Seas indicated by MODIS satellite observations. *Journal of Marine Systems*, *70*,
 1915 134-149. doi: 10.1016/j.jmarsys.2007.04.002
- 1916 Yvon-Durocher, G., Caffrey, J. M., Cescatti, A., Dossena, M., del Giorgio, P., Gasol, J. M.,
 1917 ... Allen, A. P. (2012). Reconciling the temperature dependence of respiration across
 1918 timescales and ecosystem types. *Nature*, *487*, 472-476. doi: 10.1038/nature11205
- 1919 Zhang, W., & Wirtz, K. (2017). Mutual dependence between sedimentary organic carbon
 1920 and infaunal macrobenthos resolved by mechanistic modeling. *Journal of Geophysical*
 1921 *Research: Biogeosciences*, *122*, 2509-2526. doi: 10.1002/2017JG003909
- 1922 Zhao, C., Daewel, U., & Schrum, C. (2019). Tidal impacts on primary production in the
 1923 North Sea. *Earth Syst. Dynam.*, *10*, 287-317. doi: 10.5194/esd-10-287-2019
- 1924 Zhou, Y., Evans, C., Chen, Y., Chang, K., & Martin, P. (2021). Extensive remineralization
 1925 of peatland-derived dissolved organic carbon and acidification in the Sunda Shelf Sea,
 1926 Southeast Asia. *Earth and Space Science Open Archive*, 67 pp. doi: 10.1002/essoar
 1927 .10506636.1
- 1928 Zhou, Z. X., Yu, R. C., Sun, C., Feng, M., & Zhou, M. J. (2019). Impacts of Changjiang
 1929 River Discharge and Kuroshio Intrusion on the Diatom and Dinoflagellate Blooms in
 1930 the East China Sea. *Journal of Geophysical Research: Oceans*, *124*, 5244-5257. doi:
 1931 10.1029/2019JC015158
- 1932 Zhu, J., Wu, H., & Li, L. (2015). Hydrodynamics of the Changjiang Estuary and Adja-
 1933 cent Seas. In J. Zhang (Ed.), *Ecological continuum from the changjiang (yangtze river)*
 1934 *watersheds to the east china sea continental margin* (p. 19-45). Springer International
 1935 Publishing Switzerland. doi: 10.1007/978-3-319-16339-0_2
- 1936 Zweng, M. M., Reagan, J. R., Antonov, J. I., Locarnini, R. A., Mishonov, A. V., Boyer,
 1937 T. P., ... Biddle, M. M. (2013). World Ocean Atlas 2013, Volume 2: Salinity. *Levitus,*
 1938 *S., Mishonov, A. (Eds.), NOAA Atlas NESDIS, 74*, 39 pp.